Advanced passive micro-optical elements

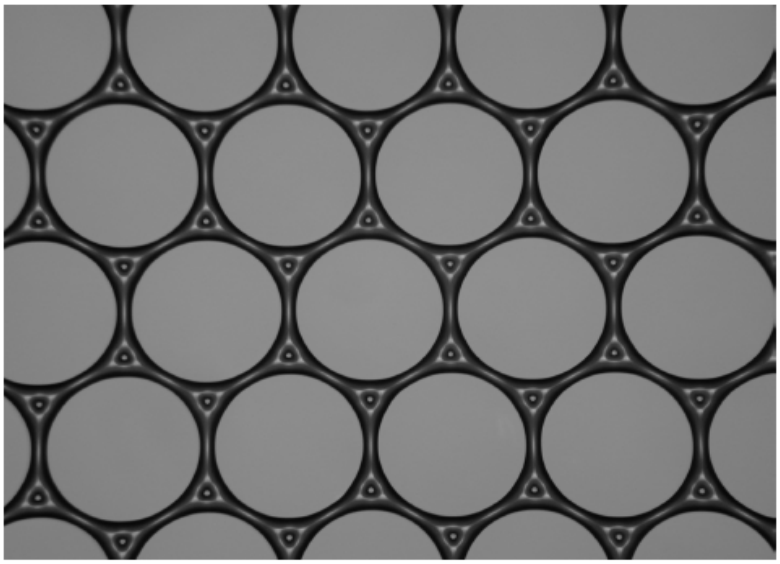

Patrick Ruffieux

Institut de microtechnique

Advanced passive micro-optical elements

Thèse

Présentée à la Faculté des Sciences pour obtenir le grade
de docteur ès sciences par

Patrick Ruffieux

Neuchâtel, Avril 2008

Thèse de l'université de Neuchâtel

Date de soutenance : le 9 Janvier 2008

Rapporteurs :

Prof. Dr. H.-P Herzig (Directeur de thèse)
Dr. T. Scharf
Dr. R. Völkel
Prof. Dr. H.P. Zappe

Mots clés: micro-optique, birefringence, cristaux liquides, polariseurs, microlentilles achromatiques, réseaux de microlentilles, homogénéiseur de faisceau, effet de moiré, agrandissement par effet de moiré, afficheurs, diffuseurs, microlentilles concaves.

Keywords : micro-optics, birefringence, liquid cristals, polarizer, achromatic microlenses, microlens arrays, beam homogenizers, moiré, moiré magnifier, displays, diffusers, concave microlenses.

Université de Neuchâtel unine

FACULTE DES SCIENCES
Secrétariat-Décanat de la faculté
- Rue Emile-Argand 11
- CP 158
- CH-2009 Neuchâtel

IMPRIMATUR POUR LA THESE

Advanced passive micro-optical elements

Patrick RUFFIEUX

UNIVERSITE DE NEUCHATEL

FACULTE DES SCIENCES

La Faculté des sciences de l'Université de Neuchâtel,
sur le rapport des membres du jury

H.P. Herzig (directeur de thèse),
T. Scharf,
R. Völkel (SUSS MicroOptics, Neuchâtel)
et H.P. Zappe (Freiburg, D)

autorise l'impression de la présente thèse.

Neuchâtel, le 21 février 2007

Le doyen :
F. Kessler

UNIVERSITE DE NEUCHATEL
FACULTE DES SCIENCES
Secrétariat - décanat de la faculté
Rue Emile-Argand 11 - CP 158
CH-2009 Neuchâtel

■ Téléphone : +41 32 718 21 00 ■ E-mail : secretariat.sciences@unine.ch ■ www.unine.ch/sciences

Abstract

Micro-optical elements are optical elements having size or details in the range of the micrometer scale. The emergency of such elements is strongly linked to the development made in the fabrication techniques during the nineties to follow the still actual trend of miniaturization. From this time it has been convenient to separate micro-optical element having refractive or reflective optical design from those ones having strictly diffractive design. In the present thesis we are in between this two fields and from conventional refractive optical elements, different features of physical optics like diffraction, polarization or interference effects are added. We start by adding the birefringent property of liquid crystal polymers (LCP) to microlenses. The interest to employ LCP is linked to the fact that bulky birefringent structures of various shapes can easily be obtained by embossing. Moreover the choice of the optical axis of this material can be chosen by boundary conditions imposed by the different surfaces embedding the liquid crystal. Using this material a micro-optical device allowing the increase of the efficiency of conventional polarizer has been designed, simulated and realized. We continue by studying the influence of the aperture size on the position of the peak irradiance of microlenses. This diffractive effect of the aperture limitation is known as the focal shift which tends to decrease the real focal length obtained from paraxial geometric optics. In the frame of this thesis, we pursue the investigation and show that this effect could be advantageously used to obtain achromatic microlenses. In the frame of beam shaping applications we realized diffusers with very narrow angular distribution. These diffusers allow high energy throughputs and homogeneity distribution for highly coherent sources employed in conventional Fly's eye condensers. The consequences of coherent sources used in such beam shaper are discused in detail and rules are given to employ our diffusers in such systems. To finish, we developed and characterized a new method to fabricate concave microlenses with diffraction limited property and applied them in the realization of optical diffusers.

Contents

1 Introduction **1**

2 Fabrication methods and simulation tools **3**
2.1 Fabrication processes . . . 3
2.1.1 Photolithography . . . 3
2.1.1.1 Microlens array fabrication . . . 6
2.1.2 Replication techniques . . . 7
2.1.3 Dry etching . . . 9
2.2 Simulation tools. . . . 11
2.2.1 Ray-Tracing . . . 11
2.2.2 Polarization ray tracing . . . 11
2.2.3 Simulation of optical fields . . . 14

3 Birefringent polarizer **17**
3.1 Introduction . . . 17
3.2 Operation principle . . . 17
3.3 Simulations . . . 19
3.4 Experimental results . . . 23
3.5 Un-collimated sources . . . 27
3.6 Head to head configuration . . . 30
3.7 Conclusion . . . 33

4 Moiré magnifier **35**
4.1 Introduction . . . 35
4.2 Moiré phenomenon . . . 35
4.3 Moiré magnifier . . . 35
4.4 Design considerations . . . 37
4.5 Image quality . . . 39
4.5.1 Image formation . . . 39
4.5.2 Parallax and orientation . . . 44
4.6 Encoding . . . 49

4.7 Conclusion 50

5 Achromatic microlenses **51**
5.1 Introduction 51
5.2 Basic considerations 52
5.3 Plano-convex refractive microlens 52
5.4 Refractive and diffractive regime 54
5.5 Achromaticity 56
5.6 Conclusion 58

6 Diffusers for optimized illuminations **61**
6.1 Introduction 61
6.2 Microlens beam homogenizers 62
6.3 Design considerations 63
6.4 Beam requirements 65
6.5 Diffraction effects 66
6.6 Coherent illumination 67
6.7 Diffusers 72
6.8 Beam Homogenizer with diffuser 75
6.9 Advanced considerations on homogeneity 78
6.10 Conclusions 79

7 Concave microlenses **81**
7.1 Introduction 81
7.2 Basic principle 81
7.3 Methodology 82
7.4 Quality measurements 84
7.5 Experimental results 85
7.6 Concave microlens diffusers 90
7.7 Conclusion 92

8 Conclusion **93**

Chapter 1

Introduction

In the nineties following the trend of miniaturization several technologies have been developed to shrink the size of refractive and reflective optical elements [1]. In parallel diffractive optics has emerged from holography. Several studies of optical elements combining the advantages of refractive (low dispersion) and diffractive properties (arbitrary beam shape) have been done. They consist in hybrid elements having both refractive and diffractive features. As an example a grating structure can be associated to the surface of a microlens to reduce its chromatic aberration [2]. Basically all these optical elements have a relatively large size and are made in isotropic media. This consideration introduces to the field of "advanced micro-optics" where different features of physical optics like diffraction, polarization or interference effects are added to basic micro-optical elements. It includes birefringent microlens arrays, diffusers obtained from designed microstructures for coherent beam shaping applications, achromatic microlenses with limited apertures and designed radius of curvature (ROC) [3] or microlenses with annular phase or amplitude steps [4]. All these elements have refractive designs compared to strictly diffractive objects such as diffractive optical elements DOE [5, 6] but their behaviors also imply diffraction, polarization and interference effects. The arrival of liquid crystal polymers [7] (LCP) on the market gave the possibility to obtain birefingent micro-optical elements of various shapes. Associated to different fabrication techniques, birefringent micro-optical elements having different orientations of their optical axis are nowadays feasible [8]. This property can be added to conventional refractive, diffractive or hybrid elements. Another trend is to combine micro-optical elements in systems in the purpose of achieving specific functions. We realized such a system by combining birefringent microlens arrays with index matching layers and patterned twisted nematic liquid crystal cell. While the actual trend in optics research is more focused on nanooptics [9] i.e. optical devices with

nano-scale structures, a still strong interest exist for refractive and diffractive optical microstructures. Most parts of the various research topics presented here have been done during projects with different industrial partners that witness the still high value of applied micro-optics. The fabrication techniques used in the frame of this work are presented in chapter two. The third chapter concerns the development and realization of a micro-optical polarizer based on birefringent optical elements. The forth chapter explores image quality of moiré magnifiers. The fifth chapter talks about the design of microlenses where diffractive effects can advantageously reduce or eliminate chromatic aberrations. Chapter six summarizes the development followed by the realization of narrow dispersion angle diffusers for beam shaping applications. Chapter seven describes a new fabrication method allowing the realization of diffraction limited concave microlenses and the generation of high quality diffusers.

Chapter 2

Fabrication methods and simulation tools

2.1 Fabrication processes

An important part of the present work has been done in the cleanroom of the optics group at the Institute of Microtechnology of Neuchatel with the help of several fabrication techniques. This chapter summarizes the different employed methods.

2.1.1 Photolithography

Firstly developed for manufacturing of microelectronics at a very large scale integration (VLSI), photolithography is nowadays commonly used to fabricate, at a wafer level, micro-optical elements from binary gratings to multi-level diffractive optical elements (DOE) or microlenses. The principle is to pattern a photosensitive material (photoresist) that can be transferred by dry etching techniques into optical substrates such as silicon or quartz. Two types of photoresist (PR) are commonly distinguished, positive or negative PR. Positive photoresists are resins synthesized from phenol and formaldehyde with addition of a photo initiator which increases their alkaline solubility by three orders of magnitude when exposed to UV light. The patterning of the photoresist is made by mean of a mask. The structures are printed in chromium or steal oxide and reflect or absorb the photon flux. This variation of solubility when exposed or not to UV light, allows transferring a pattern into the thickness of the photoresist layer. The exposed parts are removed using appropriate solvents called developers. A 2D pattern with binary profile is obtained. The different steps involved in the photolithography process are illustrated through the first four points of the microlens array fabrication described in Fig. 2.1. Firstly the PR is deposited

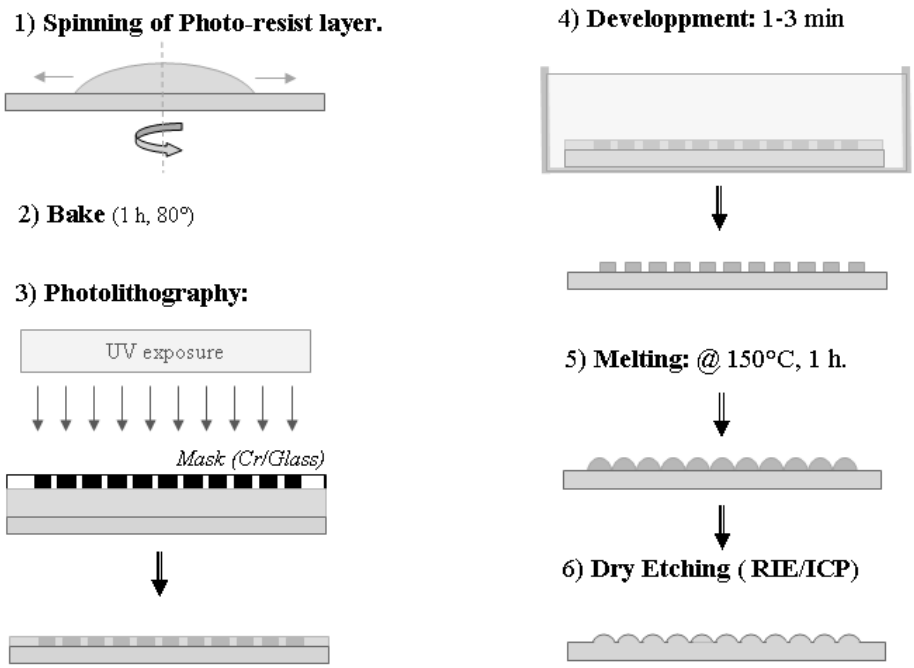

Figure 2.1: Process Flow of microlens arrays fabrication steps. (1) Pouring and spinning of photoresist PR on the wafer; (2) Bake at 80˚C to remove solvents; (3) UV exposure steps through a pattern mask in chromium; (4) Development step of the PR. All the illuminated parts are removed (positive PR); (5) Melting of the cylinders at 150˚C for 1hour to obtain microlenses; (6) Additional dry etching step to transfer the PR into the wafer.

over the whole wafer by spin coating. The spinning process consists to rotate a substrate at various speed rates over a certain period of time while deposing PR on its surface. By reaching equilibrium between centrifugal force and solvent evaporation a homogeneous layer of accurate thickness is obtained. Figure 2.2 illustrates the obtained thickness for AZ9260 photoresist versus speed rotation of the substrate. Because PR are very sensitive to ambient conditions and especially to the humidity rate, which should be set around 50%, all spinning curves must be calibrated for each machine type and cleanroom. In this operation, the viscosity partially due to the presence of solvent (55 to 85 % Vol.) is an important parameter [10]. Addition of solvent is often used to decrease the viscosity of the PR to allow deposition of thinner layer when using spinning machines. Then a typical cure at 80° for 1h is necessary to remove the remaining solvent still present inside the material. The cure parameters such as the number of temperature steps and time, depend on the thickness of the deposited PR layer as described later in the microlens array fabrication. This solvent has to be removed to avoid bubble formation and dark erosion (development rate of unexposed PR) in the development step. Then the photoresist is exposed using

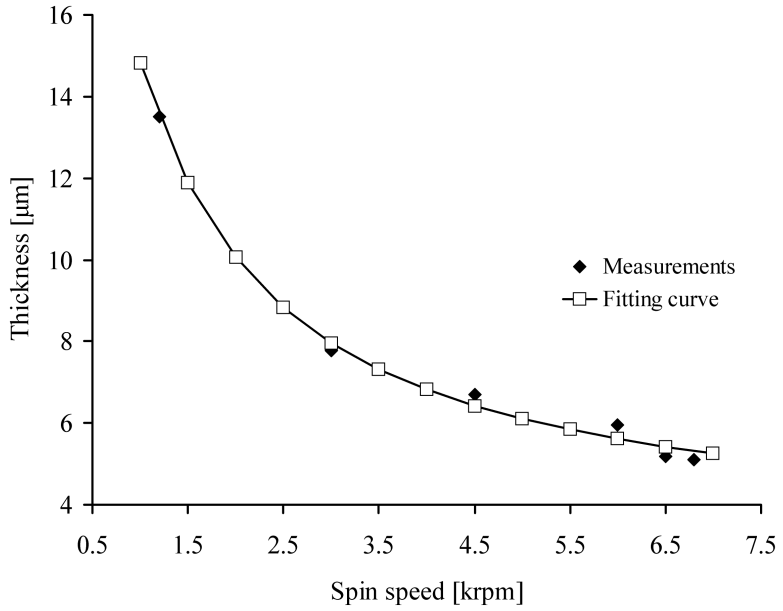

Figure 2.2: Typical example of thickness layer versus spinning speed for pure AZ9260 photoresist (CMI-EPFL). The fitted curve is described by $0.31 \cdot x^2 - 3.89 \cdot x + 17.45$ *where* x *is the spin speed.*

Table 2.1: Example of typical exposure times for different thickness of the photoresist (AZ9260, h and i lines) layer using a mask aligner MA150 (CMI-EPFL)

Resist type and treshold dosis [mJ/cm2]		Hg Power [mW/cm2]	Exposure time [s]	
			Min.	+33% safety
AZ9260 5 μm	190	10	19	23
AZ9260 8 μm	240		24	32
AZ9260 14μm	360		36	48

a mask aligner which allows an accurate positioning of the mask to the wafer. To reduce diffraction effects at the edge of the fine structured patterns contact mode can be used in which the mask and the wafer are pressed together. The typical achievable resolution is around 1 μm. The PR is exposed to UV light. The sensitivity of PR is commonly defined for three spectral lines found in the typical Hg light sources of mask aligner, i-line at 365 nm, h-line at 405 nm and g-line at 436 nm. To ensure perfect results, a calibration has to be done depending on the type of photoresist and the thickness of the layer. As an example, typical exposure times for different thicknesses of PR layers are given in Table 2.1 . To finally obtain the structures, the PR is developed in a bath of dedicated developer during 1 to 3 min. The wafer is then cleaned in de-ionized water and dried with N2 jet.

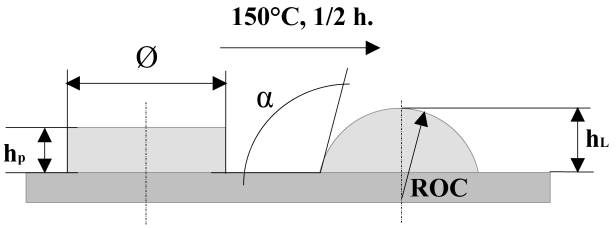

Figure 2.3: Schematic illustration of the pillar and microlens parameters. The height of the pillars h_p before melting at 150°C is correlated to the height of the microlens h_L. The diameter Ø stays the same for the pillars and for the microlens of radius of curvature ROC. The maximum achievable microlens diameter is fixed by the contact angle α.

2.1.1.1 Microlens array fabrication

In the fabrication process of microlens arrays, a 1 to 4 volume dilution of PR is used to spin a 500 nm base layer in order to set the adhesion conditions. Because of the presence of solvent, the base layer is left 1 hour at ambient temperature to remove the main part. A second layer of the desired thickness is deposited using the same method. Because of the more important thickness several cures are performed to remove the solvent. Typically for 20 microns thickness: the curing time is 1h at 50°, 1h at 60°, 1h at 70° and 1h at 80°C. Using a mask containing round holes in the chromium layer, the PR is exposed as discussed before under UV light and developed. At this stage only cylinders are fabricated. To obtain microlenses a next cure at 150°C is performed for half an hour. By melting of the resist and because of cohesive forces, a lens like shape is obtained [11, 12]. The different parameters such as the cylinders height h_c and the lens height h_L are shown in Fig. 2.3. This shape strongly depends on the adhesion boundaries conditions of the second PR layer on the base layer and the cohesive forces of the PR. Because of solvent evaporation and thermal cross linking of the material during the cure, the volume of the corresponding lens is lower than the volume of the initial cylinder. The lens height h_L is correlated to the height of the cylinders h_c by [13]

$$h_c \leq \frac{h_L}{2} + \frac{h_L^3}{6r^2}, \tag{2.1}$$

where r is the radius of the lens aperture. Equation 2.1 can be rewritten in the form $h_c = \gamma \cdot h_p$ with γ in the range between 1.3 to 1.7, meaning that the height of the microlenses is higher than the height of the initial pillars. The contact angle α seen on Fig. 2.3 depends on the surface energy, the resist volume and the diameter of the lens base during the melting step. While diffraction effects limit the minimum diameter of the microlenses Ø, the upper limit is fixed by the

height of the pillars and the contact angle α. A minimum contact angle in the order of 10° is achieved for melting PR on a resist base layer corresponding to a ratio $\frac{h_L}{\emptyset} \approx \frac{1}{23}$. Below this ratio the lens profile is deformed. For higher values of the ratio similar shape problems appear, but reflow microlenses of $\frac{h_L}{\emptyset} > \frac{1}{2}$ have already been fabricated. The best microlenses are realized with a ratio in the range between $\frac{h_L}{\emptyset} \approx \frac{1}{12}$ and $\frac{h_L}{\emptyset} \approx \frac{1}{15}$.

2.1.2 Replication techniques

Although photolithography is the dominant technology, even for large micron scale features, it is not always the best or the only option for all applications. It

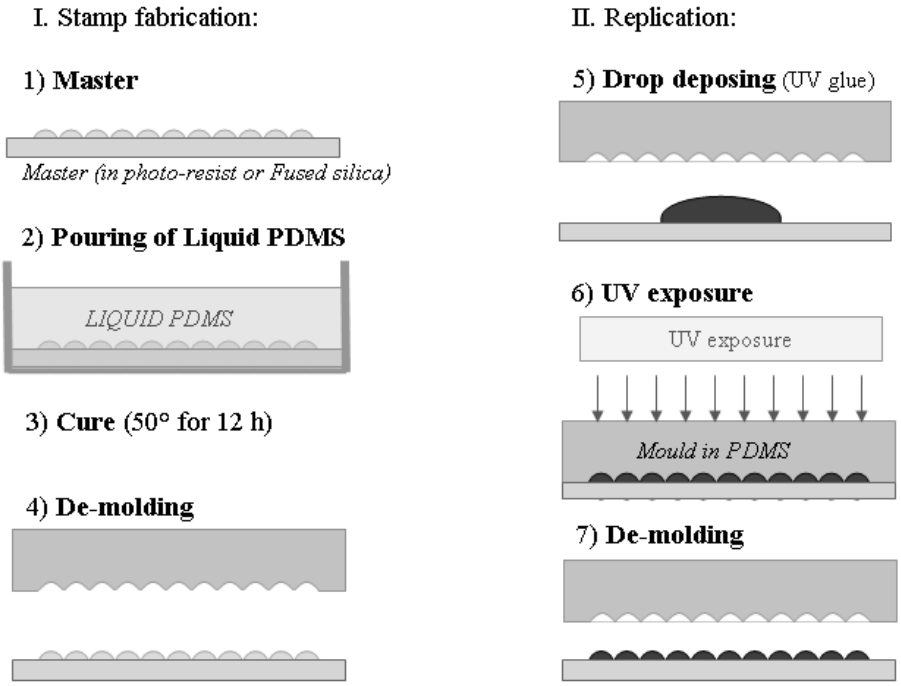

Figure 2.4: Process flow of the replication technique used; (1) Fabrication of a master; (2) Pouring of the liquid PDMS over the master; (3) Cure at 50°C for 12 hours to polymerize the PDMS. (4) De-molding operation and release of the master; (5) Deposition of UV glue on a substrate; (6) UV exposure ∼ 9 min at 350 nm to polymerize the UV adhesive; (7) De-molding operation and realization of a micro-optical element in solid UV glue.

is not an inexpensive technology and difficulties arise for patterning non planar surfaces although it becomes possible with spraycoater. In addition it provides almost no control over the chemistry of the surface and hence is not very flexible in generating patterns of specific chemical functionalities on surfaces (e.g., for anchorage-dependant tissue culture or combinatorial chemistry). Moreover it

can only generate 2D microstructures and is directly applicable only to a limited set of photosensitive materials (photoresists) [14]. As an alternative, several micro fabrication techniques on polymers have been created especially in mass production of micro-optical elements with extended functionalities. Methods such as micro injection molding [15] or embossing techniques have been developed. In the field of embossing methods, two approaches can be distinguished [14]. Soft lithography techniques, using elastomer molds, such as replica molding (REM) solvent assisted micro-molding (SAMIM), micro-molding in capillaries (MIMIC), microcontact printing and microtransfert molding (μTM) and rigid imprint techniques such as nanocontact imprint (NCM), step and flash imprint lithography (S-FIL) and nanoimprint lithography (NIL) [16, 17]. In the frame of this work a general UV embossing technique (i. e. embossing of UV curable polymer) with an elastomer mold was used. Fig. 2.4 shows the different steps involved in this process. As described in the previous section the fabrication

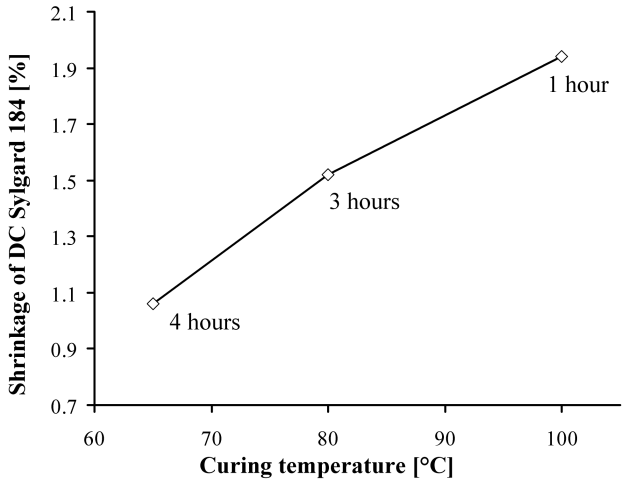

Figure 2.5: Corresponding shrinkage of Sylgard 184 PDMS versus curing conditions. The measurements were performed on a 4 inches round mold with a thickness of 1.2 mm [18].

of microlens arrays by photolithography and reflow process is a three step process. To simplify the manufacture of prototypes, a mold of the PR master is fabricated using standard Sylgard 184 PolyDiMethylSiloxane (PDMS) material from DowCorning. The material is composed out of two elements, a base and a hardener. The two components are blend together with a weight ratio of 1 part of hardener to 10 part of base [19]. After mixing, the air and solvents are removed with an additional step in a vacuum chamber at 5 mbar. The liquid is then applied directly on the master preliminary placed in an adapted container. 50 ml are enough to produce a 4 inches square mold with about 5 mm thickness. The PDMS is then polymerized in an oven 12 hours at 50°C. Faster

cure, 1 hour at 100°C, is also possible but with a corresponding shrinkage of the mold of about 2 % (Fig. 2.5). Replicas are simply made by applying the PDMS mold over a drop of optical UV glue [Norland Optical Adhesive (NOA)] and polymerized 9 minutes in a standard UV box with approximately $2\frac{mW}{cm^2}$ in the wavelength range between 350 to 400 nm. Replicated nanostructures smaller than 300 nm can be achieved but an aspect ratio of the structures in the range between 0,2-2 must be observed to avoid their collapsing [14].

2.1.3 Dry etching

To obtain microlens arrays in silicon or fused silica substrates an additional step from the reflow process described previously in the photolithography section has to be done. This step is performed using a Reactive Ion etching with Inducted Coupled Plasma (RIE-ICP) machine from STS (Surface Technology Systems). In a reactor, plasma conditions are generated for different mixtures of gases by means of electrodes supplied by a RF generator at 13.56 MHz with an adaptative power between 200-1000 W. The substrate being etched is biased to induce directional ion bombardment and produce anisotropic etch characteristics. The ions generated in the plasma are confined on the wafer and generated at low pressure (2-5 mtorr) by an additional coil driven separately by an identical RF power supply. The presence of the coil allows to increase etching rates and directional etching by increasing the ion to neutral particles ratio and reducing ions to neutral particles collisions [20]. All the different mentioned parts of the machine are illustrated in Fig. 2.6. . More recent improvements have been realized

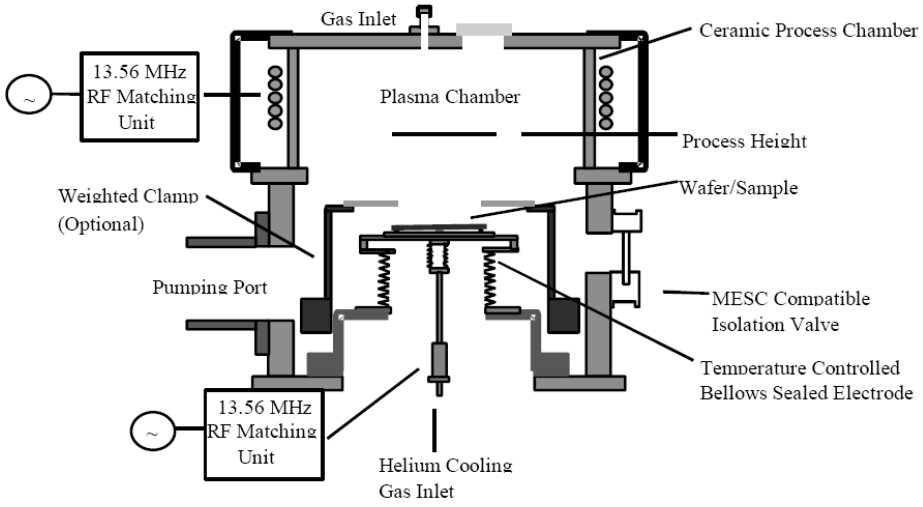

Figure 2.6: Illustration of the Multiplex-ICP system. Image source from [25].

in the etching of silicon using Deep Reactive Ion Etching (DRIE) technology.

This allows very high selectivity by repeating etching steps and formation of sidewalls passivation layers used as protective layers during the sputtering etching steps (Bosch process) [21]. Similar improvements have been realized on silicon oxide using continuous polymer layer deposition to increase the etching capability of the oxide with anisotropic etch [22]. Mainly based on fluorine chemistry, several types of gazes can be used CF_4,, C_2F_6, CHF_3, C_3F_8, C_4F_8 [23] and etching of a wide range of materials are possible (Silicon SI, quartz QZ, Aluminum AL...)[24]. In the present work C_3F_8 and SF_6 were used to etch respectively fused silica and silicon substrates, while heavy Ar molecules were added as a general surface cleaner for both materials (sputtering effect, low selectivity). In the purpose of changing the selectivity of etching between PR and the material of the substrate O_2 and CH_4 are added as an accelerator and an inhibitor of PR etching. The depth of the transferred structures can be adjusted by modifying the ratio between the different gases. Several others parameters such as plasma pressure, flux of the gases and powers of the coil and platen can be changed. During the etching process two main effects occur .

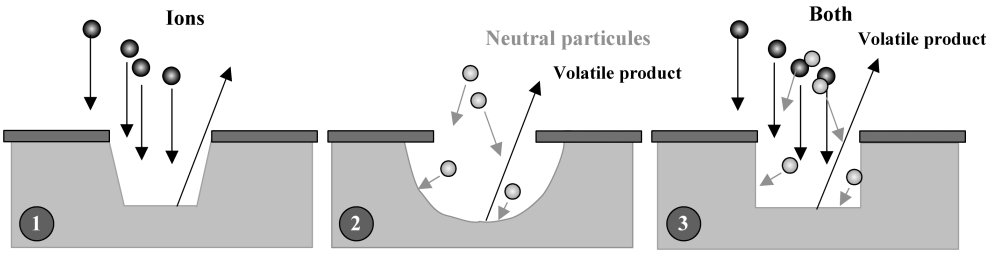

Figure 2.7: Scheme of the basic mechanisms occurring during dry etching process. (1) Physical etching i.e. sputtering etching, highly anisotropic and low selectivity. (2) Chemical etching, isotropic and high selectivity. (3) Both, anisotropic profile, good selectivity.

As described in Fig. 2.7 an isotropic chemical etching of the material happens as well as an anisotropic physical sputtering occur. By adjusting separately the pressure inside the chamber the weight of one effect to the other can be emphasized. While low pressures tend to strengthen the effect of sputtering, higher pressures increase the effect of chemical etching mechanisms as seen in Fig. 2.7 [24]. In the applied processes, the pressures were typically set between 2-5 mtorr. Because optical elements were fabricated we focused our attention to good surface roughness and obtain etching rates of 400 nm/min in PR with selectivity $S = \frac{PR_{etching\,rate}}{QZ_{etching\,rate}}$ of 0.65 for quartz (QZ) wafers coated with AZ9260 PR while 600nm/min in PR with selectivity between 0.56 to 1.14 were obtained for SI wafers. More information can be found on general etching mechanisms of Si and SiO_2 in fluorocarbon ICP plasmas in [20, 23].

2.2 Simulation tools.

2.2.1 Ray-Tracing

With the arrival of computers in the sixties and with the Fourier series expansion of the different sine and cosine functions, efficient simulations of optical system by looking at the propagation of rays, according to the laws of geometrical optics, became possible. Two principle of ray-tracing approaches can be distinguished, sequential and non-sequential ray-tracing. The sequential ray-tracing has been developed to analyze optical aberrations in imaging system. The propagation of the optical rays through the different optical interfaces of the system is calculated using the law of refraction and reflection. It performs a sequential propagation from the source through the different optical interfaces up to the image plane. The non-sequential ray-tracing has been developed to optimize design light sources or imaging instruments where internal reflections, stray-light and diffusion by the roughness of surfaces are important. It takes into account transmitted as well as reflected rays and includes geometrical optics for scattering. The main goal is the calculation of spatial or directional distribution of the power, such as the flux ϕ, the irradiance E and the radiance L [26].

2.2.2 Polarization ray tracing

Because micro-optics combines small to very small optical structures but spread over a large surfaces of several square millimeters, accurate simulations can be difficult especially in time consumption. It is therefore convenient to separate the different optical phenomena that physically appear and retain only the most significant ones. The main optical effects we had to deal with in simulations were diffraction, polarization management and coherence. In the case of birefringent refractive microstructures presented in the next chapter, we used Trace Pro software from Lambda research which is able to deal with polarization and ray splitting. No diffraction and coherence effects have been retained. As an example we simulate the case of a finite bundle of normal rays incident on a birefringent prism illustrated in Fig. 2.8. The output rays are collected on a detector screen at two different positions ((1) and (2)). The results on the intensity distribution and the degree of polarization are shown in Fig. 2.9 for position (1) and in Fig. 2.10 for position (2). Because simulations are performed using incoming natural light, the two orthogonal components (transverse electric (TE) and transverse magnetic (TM)) generated by the system cannot be recombined in an interferometric way [27]. Consequently two rays R_e and R_o having different Optical Path Difference (OPD) do not interfere and their superposition

gives, as it was the case for the input light, unpolarized light.

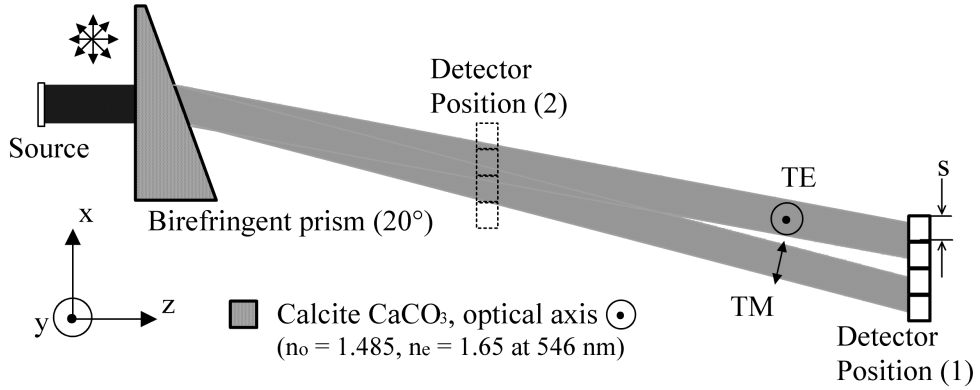

Figure 2.8: Illustration of a typical polarization management experiment performed with Trace Pro software from Lambda Reaserch. A birefringent prism is illuminated with collimated unpolarized light. At the output face of the prism double refraction occurs. TE and TM components travel with different directions of propagation.

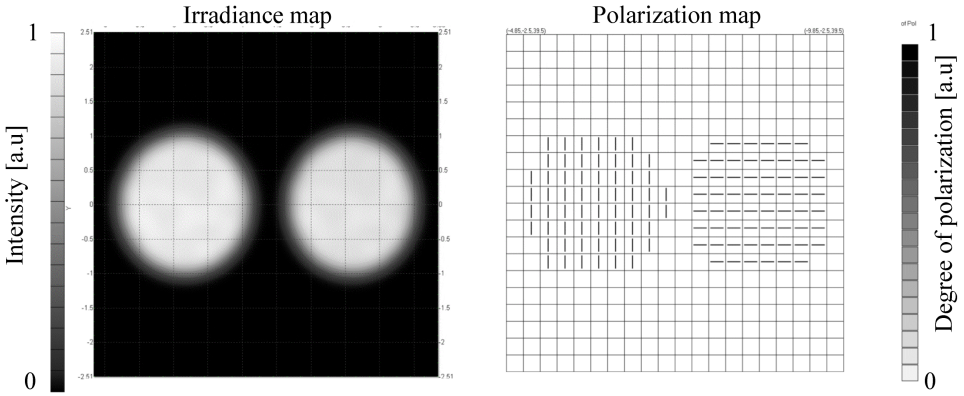

Figure 2.9: Intensity and polarization distribution at the detector plane placed in position (1) in the experiment described in Fig. 2.8. The right image shows the intensity distribution of the two beams while the left image shows the polarization distribution (state and degree) in the same plane.

The simulation of the polarization state is then simply defined by the addition of the stokes vector parameters

$$\mathbf{S}_{\mathrm{S}} = \sum_{\mathrm{S}} \mathbf{S}_{\mathrm{i}} = \sum_{\mathrm{S}} \begin{bmatrix} S_0 \\ S_1 \\ S_2 \\ S_3 \end{bmatrix}_{\mathrm{i}}, \tag{2.2}$$

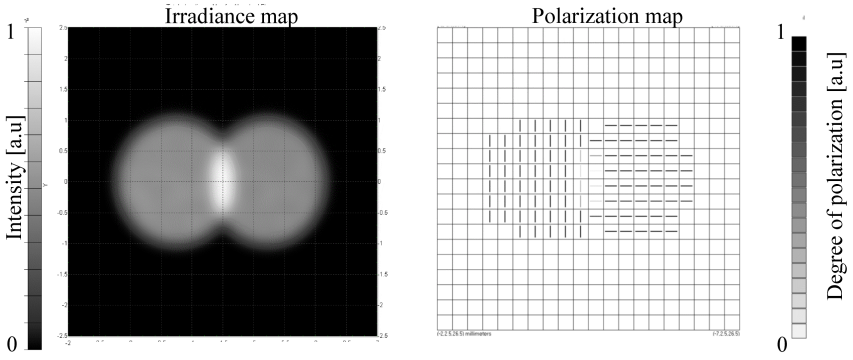

Figure 2.10: Intensity and polarization distribution at the detector plane placed in position (2) in the experiment described in Fig. 2.8. The right image shows the intensity distribution of the superposition of the two beams while the left image shows the polarization distribution in the same plane. The intensity distribution increases at the superposition of the two beams while the degree of polarization decreases in the same area.

where the index S corresponds to the sampling area in the target plan and i to the rays. In the case of a plane wave, S_0, S_1, S_2, S_3 are Stokes vector parameters linked to the amplitude polarization components A_x and A_y and their relative phase difference δ and is given by,

$$\begin{bmatrix} S_0 \\ S_1 \\ S_2 \\ S_3 \end{bmatrix} = \begin{bmatrix} \langle A_x^2 + A_y^2 \rangle \\ \langle A_x^2 - A_y^2 \rangle \\ \langle 2A_x A_y \cos(\delta) \rangle \\ \langle 2A_x A_y \sin(\delta) \rangle \end{bmatrix}. \tag{2.3}$$

The degree of polarization is then defined by

$$p = \frac{\sqrt{S_1^2 + S_2^2 + S_3^2}}{S_0}. \tag{2.4}$$

In the case of rays the intensity is replaced by the amount of power or flux. For instance, the addition of a ray TE polarized with an associated flux P_1 represented by a Stokes vector, [P_1 P_1 0 0] and a second ray TM polarized, [P_2 -P_2 0 0] will give [$(P_1 + P_2)$ $(P_1 - P_2)$ 0 0] corresponding to a partially polarized ray $p = \left|\frac{P_1 - P_2}{P_1 + P_2}\right|$ with flux $P_1 + P_2$. The local intensity will be defined by the ratio between the flux and the sampling area S. This can be seen in Fig. 2.10 where the degree of polarization drops down to nearly zero at the intersection of the two beams because of the superposition of the two orthogonal components. The sign of the parameter S_1 gives the orientation of the linear polarization. To ensure different cases of the resulting degree of polarization at the intersection of the two beams, the light source was set to have randomly distributed rays

at its surface. The degree of polarization is now dependent on the number of rays striking the local sampling area S. More complete interpretations and explanations on Stokes vectors and associated Mueller matrix can be found in [28].

2.2.3 Simulation of optical fields

In the case of micro-optical elements, the diffraction of the light becomes important and has to be taken into account in the simulations. This is specially the case in the understanding of the light propagation through microlenses with finite apertures which are studied in details in the chapter 5. Several rig-

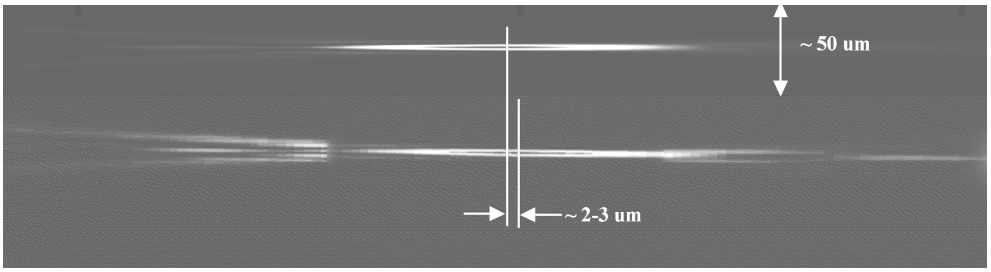

Figure 2.11: Comparison between simulated (upper image) and measured (bottom pictures) intensity distribution of the focal region of a microlens of Ø = 250 μm, ROC= 864 μm and Strehl ratio of 96.

orous methods like FDTD (Finite Differential Time Domain), FMM (Fourier Modal Method) have been developed nowadays to understand the propagation of electromagnetic waves through optical objects. Nevertheless these accurate methods are not appropriate for wide optical geometries such as microlenses of several hundred of microns, mainly because of their somehow too high precision (not necessary) and their time consuming. To overcome these difficulties we choose the FRED simulation software from Photons Engineering combining scalar diffraction theory and easy implementations of complex geometries of several millimeters with coherent illuminations. The aim of this paragraph is to validate this approach through comparison with 2D measurements of the intensity distribution of a microlens of $Ø = 250\,\mu m$ with a Radius of curvature (ROC) equal to $864\,\mu m$ performed using a Mach-Zehnder interferometer. This is illustrated in Fig. 2.11 where the position of the peak irradiance is the same in both cases with a slight difference of only 2-3 microns. The shape of the intensity distribution is well comparable with the presence of the different side lobes. The measured image is the combination of three scans over $100\,\mu m$ with different intensity of the laser source to avoid saturation of the CCD camera. This explains the general higher contrast measured in the side lobes. A

comparison of the position of the peak irradiance position through a circular aperture has been done with the resolution of the Rayleigh Sommerfeld integral and FRED software in chapter 5.

Chapter 3

Birefringent polarizer

3.1 Introduction

The appearance of polymerizable liquid crystal mesogens (LCP) has opened new opportunities for manufacturing of birefringent components and devices, often composed of expensive and bulky materials such as calcite or quartz [29]. Replication of micro-optical components is standard but not known for birefringent organic materials until now [30]. Combining different methods such as soft (or UV) embossing with alignment of liquid crystals on nanostructures and index matching, elements of various shapes and devices with increased functionalities can be produced [31]. The purpose of the proposed device is to convert incoming natural light into nearly linearly polarized light with efficiency over 50 %. Compared to conventional polarization management devices developed for LCD projector [32, 33] we avoid expensive components such as polarizing beamsplitters. Moreover the wafer based fabrication process strongly reduces the obstruction to a thickness of only few millimeters.

3.2 Operation principle

The principle of the present device is based on splitting natural light into its polarization components and modifying one component with a polarization rotator to get one polarization state at the output. Neither absorption nor reflection is used. With the help of birefringent lenses, incoming natural light can be split into its two linear polarization components with two different focal points [34]. Embedding the lens in an index matching environment allows focalizing one polarization only, leaving the other unaffected. If we consider only the polarization component which is not focalized by the system and we rotate it by 90° all this light will be transformed into a polarization state perpendicular to its origin.

This light has now the same polarization state as the focalized second polarization component. Only one polarization state will therefore be transmitted. The system becomes a polarizer with very high efficiency and without loss due to absorption. This operation principle is shown in details in Fig. 3.1. Because one

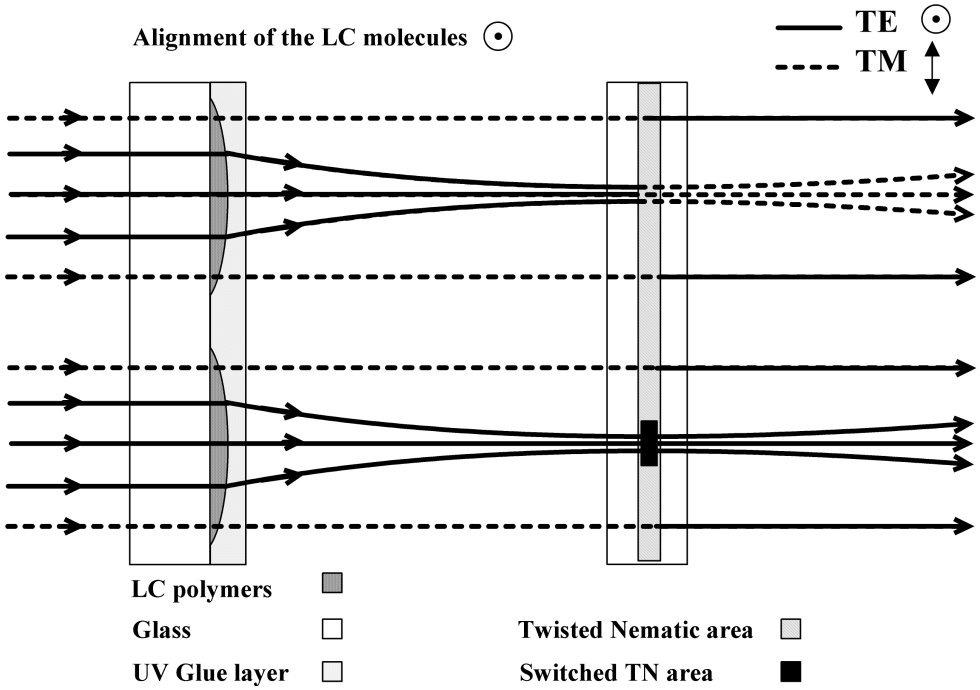

Figure 3.1: Operation principle, on the top lens of the picture, the incoming light is split by the microlens, TE polarization is focused on the twisted nematic (TN) cell and converted into TM polarization while TM component is not focused and converted into TE polarization. The bottom lens shows the same system but with a switched zone in the TN cell located at the focal point, resulting in a whole TE polarization at the output of the TN cell. Note that if the TN cell is switched the polarization is maintained.

of the polarization components is focalized and the other is not, the beam characteristics will be changed. To achromatically rotate in the visible wavelength range the polarization a twisted nematic (TN) cell is well suited. The choice of rotating the unfocalized component comes from the angular sensitivity of the TN cell [29] which could be important for angles higher than 20° or a numerical aperture of the microlens $NA > 0.34$. Because the micro-optical polarizer (MP) converts incoming natural light into polarized light it is not possible to use it as conventional dichroic (absorption of one polarization component) polarizers. The behavior of the MP is described in Fig. 3.2 for different case of polarization of the input light and compared to a conventional polarizer. In the first case (A), the input light I_{IN} is unpolarized and only half the intensity is converted into a linearly polarization state I_{OUT} by the polarizer. In the case of the MP

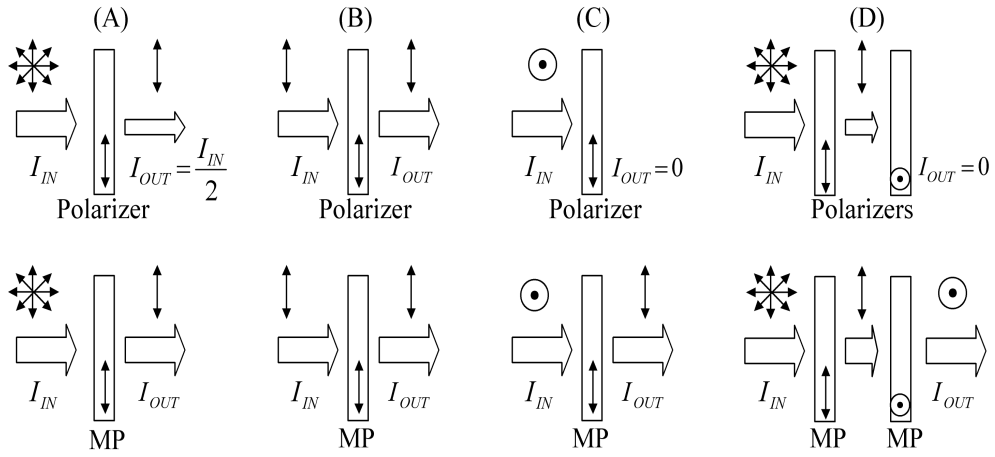

Figure 3.2: Illustration of the behaviors of a perfect dichroic polarizer (top part) compared to the case of a perfect micro-optical polarizer MP (bottom part) under different illumination conditions. The arrow in the polarizer and the MP gives their optical axis orientation.

all the intensity is converted. In the second case (B) the input light is linearly polarized and parallel to the devices. Both let pass the light. In the third case (C), the polarization of the input light is orthogonal to the optical axis of the devices. No light passes trough the polarizer while all the light is converted by the MP. (D) Crossed polarizer and MP configurations. The unpolarized input light is totally absorbed by the second polarizer while all the converted intensity is rotated by the MP. We have realized such a micro-optical polarizer (MP) with an array of birefringent microlenses and a patterned twisted nematic (TN) cell as a polarization rotator.

3.3 Simulations

We studied a system with an array of cylindrical microlenses of $150\,\mu m$ width and about $25\,\mu m$ height. All the elements constituting the MP are illustrated in Fig. 3.3. The incident natural light reached the microlenses array from the left and due to the index matching between the ordinary refractive index (n_o) and the refractive index n of the matrix material, only one component of the polarization is focused on the twisted nematic cell. The focal length of the microlens for the focalized component is given by

$$f = \frac{ROC}{n_e - n}, \tag{3.1}$$

where ROC is the radius of curvature of the microlens, n_e the extraordinary index of the birefringent material and n the index of refraction of the matrix

material. The TN cell has striped electrodes, visible as black zone in Fig. 3.3.

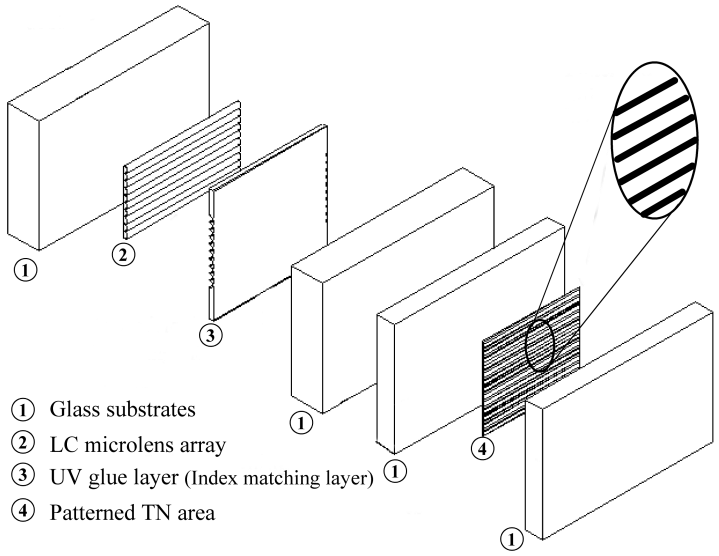

Figure 3.3: Illustration of the complete device. All the elements are represented with their effective thickness. The whole system is less than 2 mm thick.

If the TN cell is switched, these zones will become homeotropic (meaning that the orientation of the molecules will be set normal to the substrate) and the cell forms a grating of twisted and non-twisted areas. Light passing through switched areas is only slightly affected and in the ideal case no change of the state of polarization will be observed. The non-switched areas rotate the polarization by 90°. Simulations have been performed with commercial optical ray tracing software (Trace Pro Expert) that allows simulating polarization optics including crystal optics. One problem for the simulation is the twisted nematic cell. In the present case with restricted angular range, we have chosen a very simple model. The polarization rotation behavior of the TN cell was simulated by a half wave plate positioned at 45° with respect to the orientation of the cylindrical microlens array. The corresponding Mueller matrix has been used instead of more complex, but more accurate methods, such those ones described in [35] which take ray splitting and local interferences phenomenon into account. Let us calculate the efficiency for our model system. In the ideal case all the light of the polarization component that is focused is left unchanged. The other polarization component traverses the system parallel and is rotated, except for the areas, where the TN cell is switched. In the switched zones the polarization is not changed and will remain in the undesired state. The amount of this loss L_1 is given by the ratio of the portion of light that is not rotated and the total incident light i.e. by the ratio of the area of the switchable zones and the total area. It follows for a cylindrical lens grating with a given pitch of Λ_{Lenses} and a

width of the commuted area of W_{TN} to

$$L_1 = \frac{1}{2} \cdot \frac{W_{TN}}{\Lambda_{Lenses}} \,. \tag{3.2}$$

The factor $\frac{1}{2}$ appears in the calculation because only one polarization component shows that type of loss. Taking a pitch of $\Lambda_{Lenses} = 150\,\mu m$ and a width of the commuted area of $W_{TN} = 20\,\mu m$ this leads to the following rate $L_1 = 6.5\,\%$. To this loss we also have to add the part of the light passing through the space between two lenses W_{Gap} and not being affected by the system

$$L_2 = \frac{1}{2} \cdot \frac{W_{Gap}}{\Lambda_{Lenses}} \,. \tag{3.3}$$

For manufacturing reasons this space W_{Gap} is fixed to $5\,\mu m$ leading to a loss of $L_2 = 1.6\,\%$ for cylindrical lenses. So the maximum theoretical polarization efficiency P_e without Fresnel reflection losses is given by

$$P_e = 1 - (L_1 + L_2)\,, \tag{3.4}$$

which gives $P_e = 91.9\,\%$. These different losses and the parameters involved in the calculations are shown in details in Fig. 3.4.

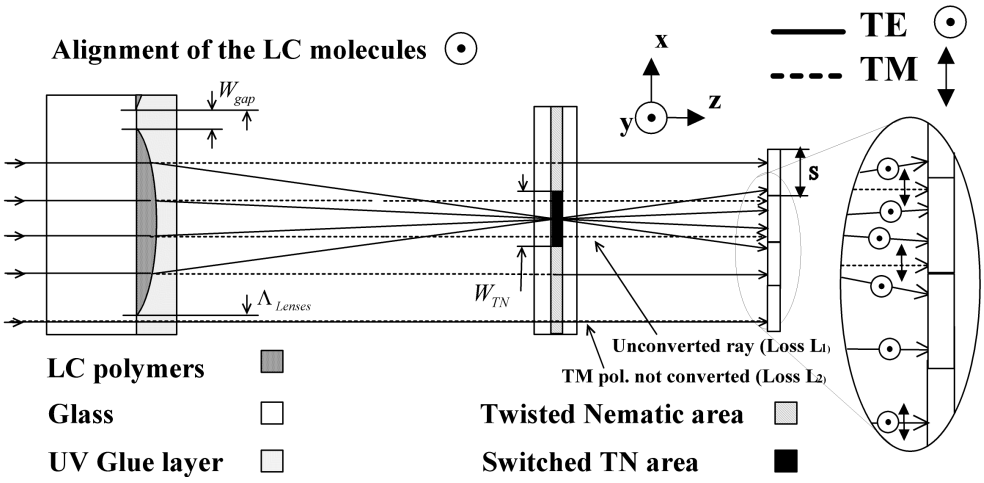

Figure 3.4: Illustration of the different losses present in the system and ray tracing interpretation of the polarization state at the output of the micro-optical polarizer. S corresponds to the sampling area (collecting the rays) retained in the calculation of the polarization state and the intensity distribution.

Another limitation of the system is its high angular sensitivity, since one component of the polarization must be precisely focalized on the switchable TN area. Figure 3.5 illustrates the case of perfectly collimated incoming light striking the device with normal incidence.

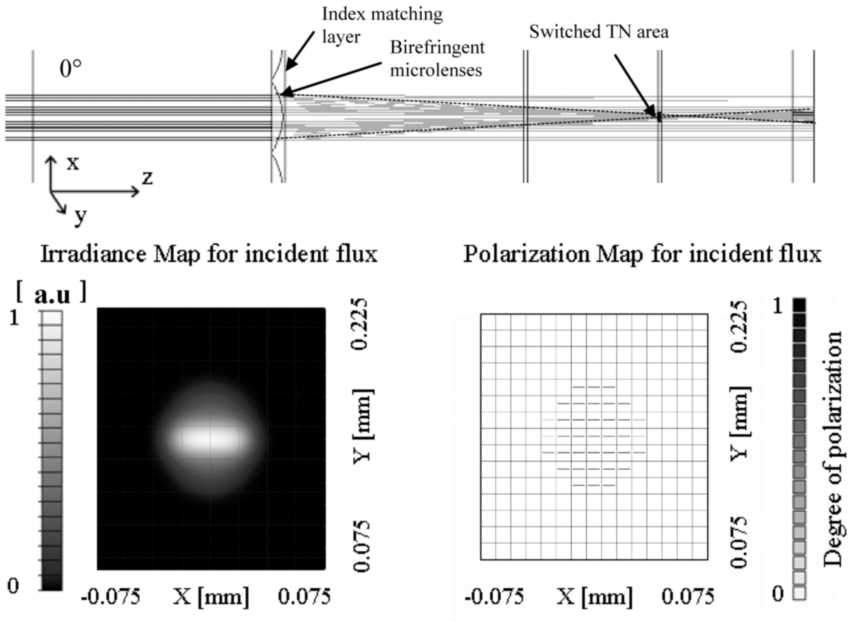

Figure 3.5: Resulting intensity distribution and polarization state for perfectly collimated light at normal incidence. The linear polarization state of the beam is almost homogenous, but the degree of polarization drop down in its center because of the presence of unconverted rays as explained in Fig. 3.4.

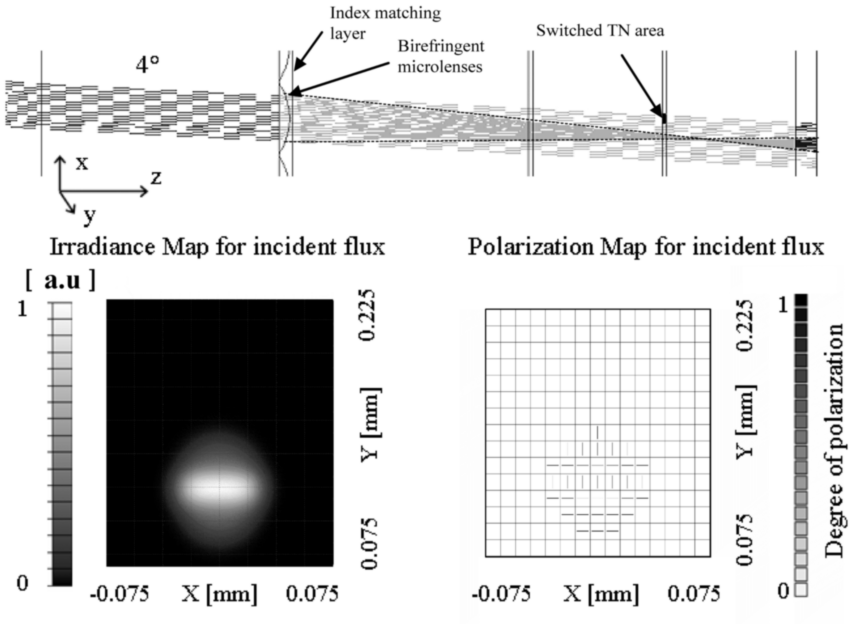

Figure 3.6: Resulting intensity distribution and polarization state for perfectly collimated light at 4˚ of incidence. The focalized polarization does no more pass through the switched area of the TN cell. The polarization map shows the resulting inhomogeneous polarization distribution.

The bottom left picture shows the resulting intensity distribution. The

white area of higher intensity inside the beam spot is due to the focus of one polarization component and shows the new spatial distribution of the output light. In Fig. 3.6, the incoming light is slightly deviated and strikes the microlens

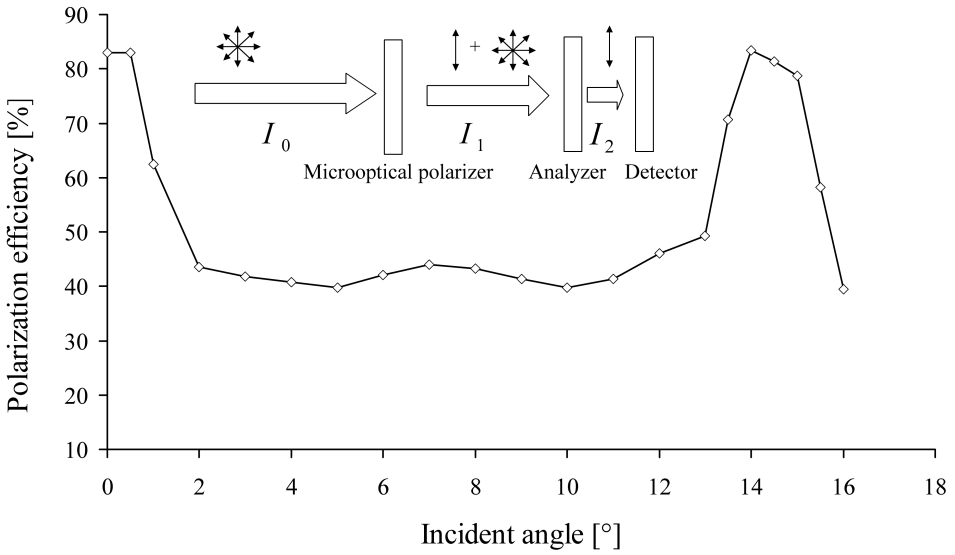

Figure 3.7: Simulated polarization efficiency P_e as a function of the angle of incidence of collimated input light for a system with microlens diameter $Ø = 145\,\mu m$, pitch $= 150\,\mu m$, $h_{lens} = 25\,\mu m$ and a width of the commuted TN area of $20\,\mu m$. P_e is defined as the ratio of the output intensity I_2 and input intensity I_0.

at an angle of 4°, the focused polarization misses the switched area of the TN cell, the polarization state is no more improved as shown in the bottom right picture. The use of cylindrical microlenses can eliminate this dependency in one axis but the problem remains in the other direction. Taking an additional polarizer at the output, the transmission is a measure of the polarization efficiency P_e of the micro-optical polarizer. The simulated transmission as a function of the angle of incidence is shown in Fig. 3.7. After few degrees of inclination the focal points of the focused polarization components do not hit the switched areas of the TN cell anymore and the efficiency drops down and rises again when neighbored switchable areas are found at about 15°. The polarization efficiency drops even below 50% since one polarization does not reach anymore the switched areas and the other component continues to pass through them.

3.4 Experimental results

As described earlier, the presented micro-optical polarizer is composed of two liquid crystal cells. One cell contains the birefringent microlenses between two

glass plates and immersed in index matching fluid. The other is a twisted nematic cell with structured electrodes. The birefringent microlens array is made by a replication process with a silicon stamp, printing the structures into a liquid crystal polymer (LCP) which is afterwards polymerized. The parallel alignment of the LCP in the nematic phase is obtained by boundary conditions imposed by rubbed polyimide coating on one side and nanostructures relief (fabricated by laser beam interference [36, 37]) of the silicon stamp on the other side. After annealing and polymerization of the LC with ultraviolet light (UV) the stamp is removed and a thin layer of index matching UV glue is deposed over the array. The cell is completed by another glass plate and an additional UV curing step to polymerize the UV glue. A very robust temperature insensitive birefringent microlens array is formed. Finally, a TN cell with structured grating electrodes is glued on the lens array respecting the narrow alignment tolerances of aligning the microlens array to the switchable grating structures. To realize the birefringent microlenses, conventional cylindrical microlenses of $150\,\mu m$ pitch spaced by $5\,\mu m$ were used. They were fabricated in photoresist using the reflow technique described in the introduction. By means of laser beam interference a grating of 400 nm pitch with 80 nm depth is recorded on the microlenses with an additional step of lithography. This master is used for stamp fabrication in PDMS silicone material. The liquid crystal polymers are heated to 100° C to evaporate the remaining solvent and avoid bubbles formation during fabrication steps. One drop of LCP is put on a glass plate with a rubbed polyimide layer and the stamp is applied directly over it. After 15 min on the hot plate, a pressure of 1 bar is applied on the stamp. The system is hold at 80° C in an oven for at least 1 hour to align the LCP molecules. As LCP, RM 257 from MERCK with a birefringence of about $\Delta n = 0.14$ (n_o= 1.54; n_e= 1.68) was used.

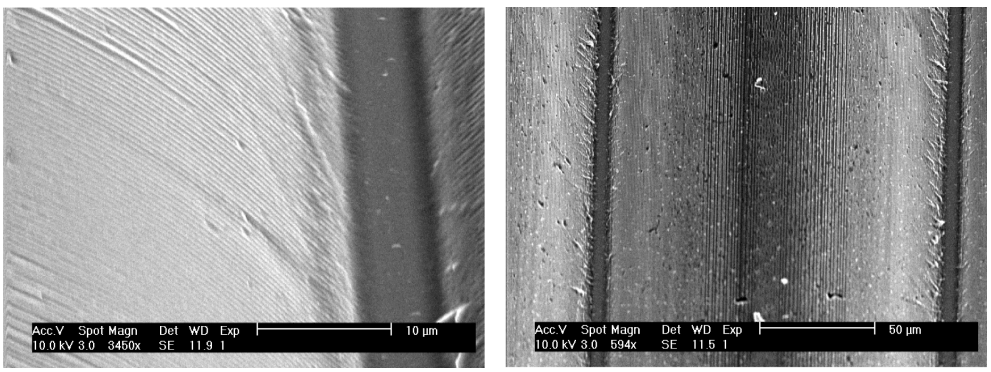

Figure 3.8: SEM Pictures of free standing birefringent microlenses, detail of the alignment grating parallel and orthogonal. (Scales, $10\,\mu m$ *and* $60\,\mu m$*)*

The polymerization of the LCP is done under UV exposure for 9 minutes in a standard UV curing chamber (Intensity of $2\frac{mW}{cm^2}$ in the wavelength range

between 350 to 400 nm). Fig. 3.8 shows two types of free standing birefringent microlenses in LCP. The grating written on the stamp used to mold the microlenses in the LCP is clearly visible. In Fig. 3.9 we can see, the different elements constituting the micro-optical polarizer, firstly the birefringent microlenses, the focal line at the position of the TN cell and the output light. The pictures have been taken at different positions (1,2,3) in the complete system. Figure 3.10 shows the device in the three possible states. Firstly the device is

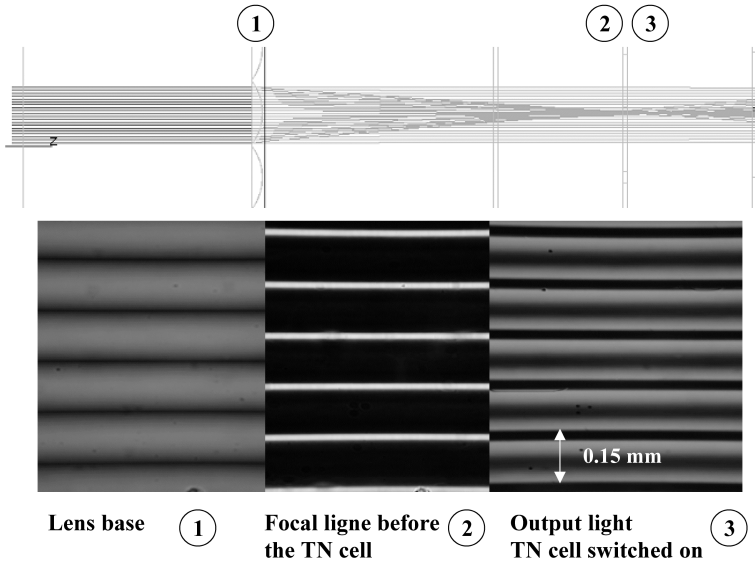

Figure 3.9: Pictures of the realized prototype taken at different distances inside the system showing the microlenses, the focal line and the output light.

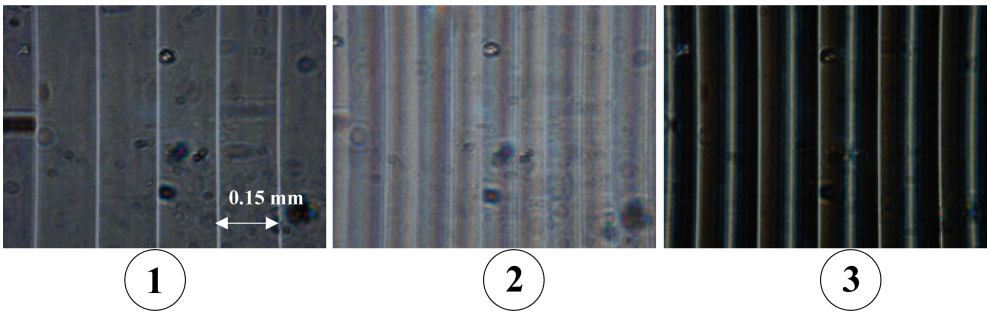

Figure 3.10: Pictures of the realized device in the three possible states under unpolarized collimated white light. Picture (1) the electrodes are switched off, picture (2) switched on, picture (3) black position and TN electrodes switched on.

under collimated but unpolarized illumination. Picture (1) corresponds to the initial state where no voltage is applied on the TN electrodes. This features the basic condition where no change occurs in the illumination except on its spatial distribution. The second image (2) illustrates the device in bright position, i.

e. the optical axis of the analyzer stands parallel to the optical axis of the MP and the TN cell is commuted. The light is completely focused on the switched areas of the TN cell and passed without any change of polarization. A general increasing of the brightness of the picture taken under identical conditions shows the performance of the device. In black position (3), i. e. the optical axis of the analyzer is perpendicular to the optical axis of the device, several stripes appear because of the better contrast as well as a general decreasing of the brightness of the picture. These broader white stripes are the result of disclination lines at the border of the switched zones in the TN cell and because the wrong polarization component passes there without being rotated. The thinner lines correspond to the space between lenses. To measure the performance of the device, the output intensity for a combination of the micro-optical polarizer and a conventional sheet polarizer was measured under natural light using a microscope. To ensure a good collimation of the input light diaphragms have

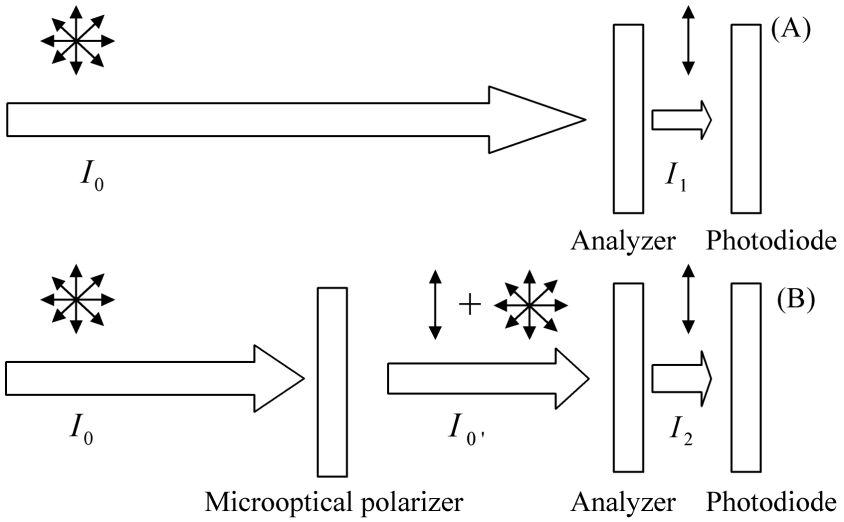

Figure 3.11: Illustration of the configuration used in the measurements of the polarization efficiency P_e of the micro-optical polarizer MP. In the first part of the measure, the intensity I_1 is detected without the MP but through a conventional dichroic polarizer (A), In the second part the MP is placed in front of the analyzer and the intensity I_2 is detected (B). The intensity directly at the output of the MP $I_{0'}$ is not measured because of its not well defined polarization state.

been used. To allow comparisons with the simulated polarization efficiency P_e, we assume 50% efficiency ($P_e = 0.5$) for the analyzer, representing the case of a perfect dichroic polarizer as simulated in the previous section

$$P_{e_{measured}} = \frac{I_2 - I_1}{2 \cdot I_1} + 0.5. \tag{3.5}$$

I_2 corresponds to the intensity measured with the micro-optical polarizer and I_1 without MP as described in Fig 3.11. Results are shown in Fig. 3.12 for angles of incidence in a range between 0° and 18°. The displacement of the second

Figure 3.12: Measured and simulated polarization efficiency as a function of the angle of incidence for a system with microlens diameter $\emptyset = 145\,\mu m$*, pitch* $= 150\,\mu m$*, hlens* $= 25\,\mu m$ *and a width of the commuted TN area* W_{TN} *of* $20\,\mu m$*.*

peak of the efficiency measurements may come from a bad position of the glued TN cell which is thicker than the focal length of the microlenses. At normal incidence, the presence of the device before the analyzer leads to a measured transmission increased by 34 %. The general smoothing of the curve probably comes from the fact that no diffractive effects have been taken into account in simulations. In real measurements the width of the focal point is enlarged by diffraction of the input white light and by the divergence of the source.

3.5 Un-collimated sources

As mentioned in the upper paragraph the realized system is well suited for highly collimated sources and not appropriate for diverging light sources. Nevertheless by adapting some design parameters it is possible to strongly increase the efficiency for that type of illumination. All the sources are assumed to have constant radiance over an angular range between $\pm\,\alpha_{max}$ defined through their F-Number given for any lens by

$$F\# = \frac{f}{2r} \approx \frac{1}{2NA}, \tag{3.6}$$

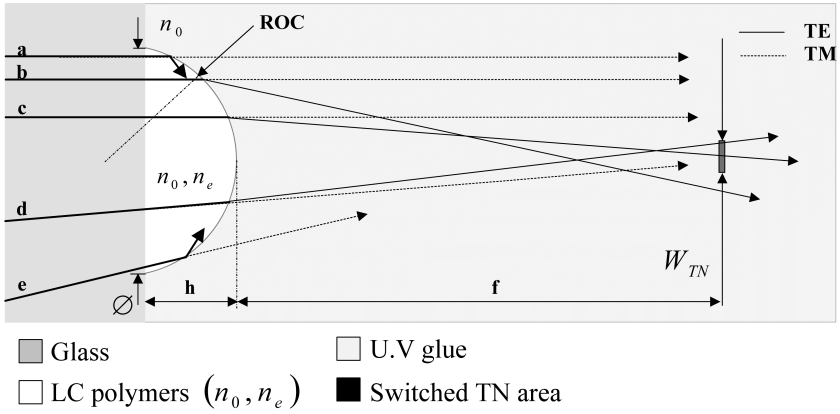

Figure 3.13: Schematic illustration of the design optimization; (a) Total internal reflection (TIR); (b) Spherical aberration, the focused polarization reaches no more the TN area; (c) Focused ray; (d) Off axis ray still focused; (e) TIR of an off axis ray. ROC and W_{TN} are parameters to optimize. Fresnel reflections are not illustrated.

with f as the focal length, r the radius of the lens aperture. The numerical aperture NA is defined by the half angle α_{max} with

$$\alpha_{max} = \arctan\left(\frac{1}{2F\#}\right) . \tag{3.7}$$

As seen in Fig. 3.13, two parameters can be optimized, firstly the focal length of the microlenses through their ROC and secondly the width of the TN cell. The position of the TN cell is fixed to the focus of the microlenses. Taking into account all the different Fresnel losses occurring at the lens interface for off axis rays in a 3D geometry of the system, the calculated transmission is then plotted as function of the F-number of the light source for simulations of microlenses with different radius of curvature (ROC) (see Fig. 3.14) and for different width of the commuted areas in the TN cell (see Fig. 3.15). The main parameter to adjust, in purpose of avoiding losses when rays strike the device with a certain angle, is the focal length. This is checked in simulations by reducing the ROC in Fig. 3.14. It has to be noticed that the position of the TN cell is fixed to the corresponding focal length of the microlenses. Nevertheless a limit is found when aberrations and total internal reflections appear in the microlenses, the highest efficiency is achieved with ROC = 0.091 mm. For large F-Number sources, the width of the commuted areas of the TN cell can be enlarged to ensure a better efficiency of the system, as shown in Fig. 3.15 because the focusing ability of the microlenses is strongly reduced by the angular dispersion at the entrance of the system. In other words, this means that for collimated rays the efficiency will drop down following

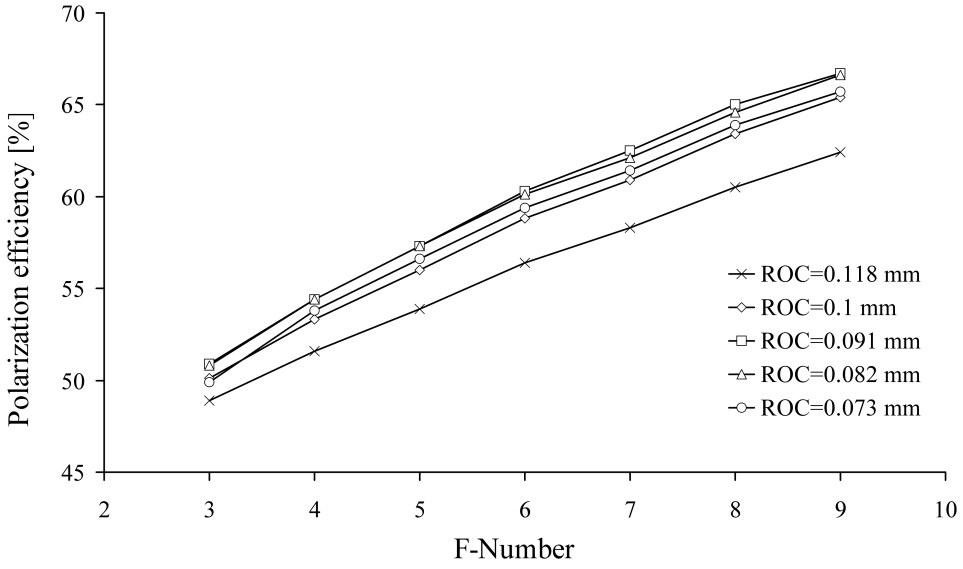

Figure 3.14: Simulated polarization efficiency for sources with different F-numbers and various ROC of the microlenses. The microlens array period is $\Lambda_{Lenses} = 150\,\mu m$*, the gap of* $W_{gap} = 5\,\mu m$ *and the TN switched area* $W_{TN\,Cell} = 20\,\mu m$*.*

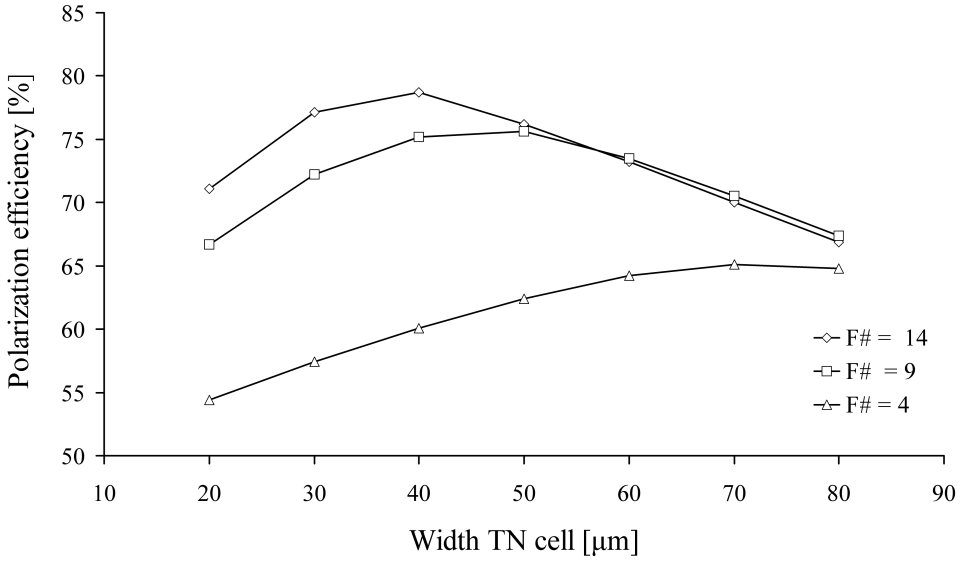

Figure 3.15: Simulated efficiency for three sources with different F-numbers in function of the width of the commuted zones in the TN cell. The ROC of microlenses is 0.09 mm, the microlens period $\Lambda_{Lenses} = 150\,\mu m$ *and the gap* $W_{gap} = 5\,\mu m$*.*

Eq. 3.2, but will increase for off axis rays. As an example an increasing of 10% of the overall efficiency is simulated for by changing the TN width from $20\,\mu m$ to $70\,\mu m$ for a source with a F-Number, F# = 4 (diverging angle α_{max}

defined by Eq. 3.7, $\alpha_{max} = 7.1$) as seen in Fig. 3.15. Appling this considerations it is possible to maximize the system by adjusting the two parameters (W_{th}, ROC) for each specific source.

3.6 Head to head configuration

A strong improvement in the design of the present device can be obtained by adding a second birefringent microlens array with an orthogonal orientation of the optical axis. Based on the identical principle described in the previous paragraph, the second array of microlenses focuses the second polarization component in the plan of the TN cell. This new concept is illustrated in detail in

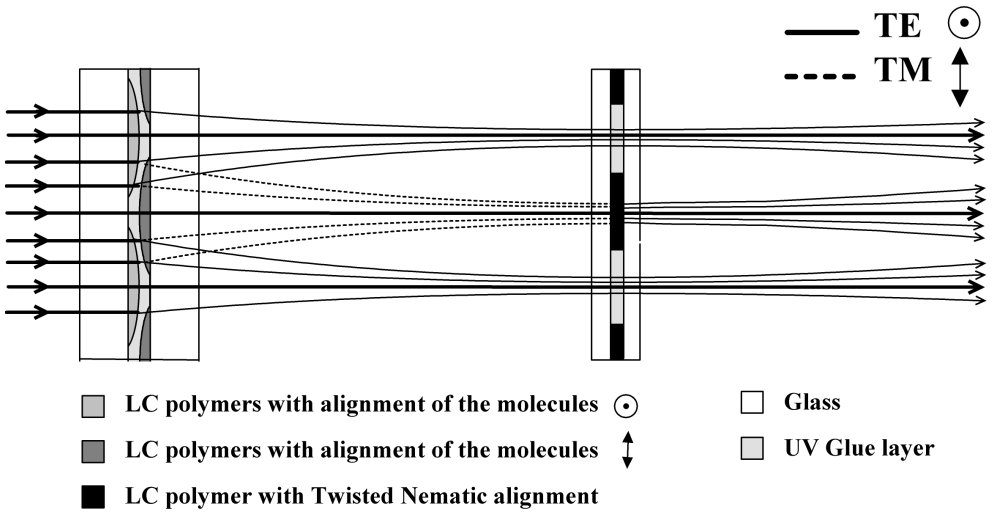

Figure 3.16: Illustration of the Head to Head configuration. The optical axis of the two birefringent microlens arrays are set orthogonal. Both polarizations are focalized. A complete separation of each polarization is performed, with a direct possibility of increasing the width of the TN areas to half the pitch of the microlens arrays.

Fig. 3.16 . In this case, the maximum theoretical polarization efficiency P_e is defined simply by the ratio of the amount of non focused light and focused light, i.e. by two times the half ratio of the gap between microlenses W_{gap} over the microlens array period Λ_{Lenses} :

$$P_e = 1 - \frac{W_{gap}}{\Lambda_{Lenses}}. \tag{3.8}$$

Equation 3.8 leads to an efficiency $P_e = 96.7\%$ for a period $\Lambda_{Lenses} = 150\,\mu m$ and a gap of $W_{gap} = 5\,\mu m$. A complete separation of both polarization components is then achieved.

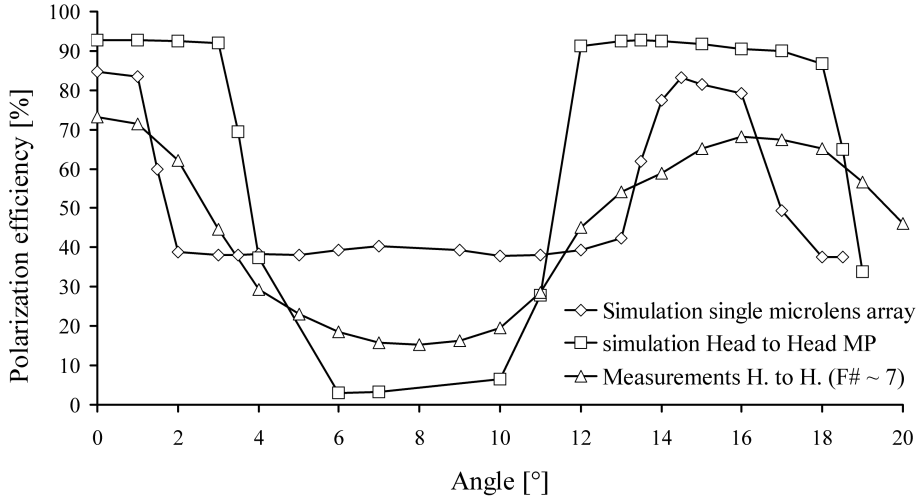

Figure 3.17: Simulated and measured polarization efficiency versus the angle of incidence of collimated light for one microlens array and Head to Head configurations systems with microlens diameter $\emptyset = 145\,\mu m$*, pitch* $= 150\,\mu m$*, hlens* $= 25\,\mu m$ *and a width of the commuted TN area of* $20\,\mu m$*.*

The main implication is a possible widening of the TN commuted area to half the pitch of the microlens array without adding losses to the first polarization component. A lower angular sensitive micro-optical polarizer is then realized. The same consideration described previously on the optimization of the ROC applies. Using the soft embossing technique discussed previously for the fabrication of the birefringent microlens arrays, an unswitchable pattern TN cell in LC polymers with half the pitch of the microlens array has been realized. The height of the cell is $10\,\mu m$. The measured polarization efficiency of the device has been performed under white light illumination using diaphragms (F# $\sim$7) and the mercury lamp of the microscope as an unpolarized light source. The results are shown in Fig. 3.17. The general smoothing of the measured curves may similarly be explained by the diffraction of the white light and by the divergence of the source which widespread the focus point. In Fig. 3.18 the effect of the two birefringent microlens arrays is shown through three pictures. On the right the analyzer is positioned parallel to the microlens array and only one focalized polarization is visible. In the center picture the analyzer is rotated by 90° and the second focalized polarization is now visible. In the last picture the analyzer is removed and both focalized polarizations are visible. Using standard linear photodiode, an average gain of 45% ($P_e = 72,5\%$) on the transmitted intensity has been measured with a contrast defined as the ratio between maximum transmitted intensity and minimum transmitted intensity through the device and the polarizer of reference

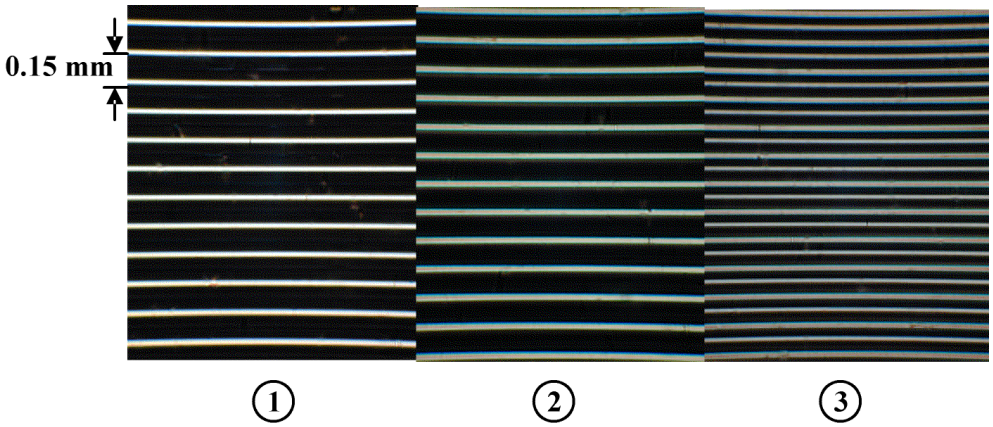

Figure 3.18: Pictures of focalization of one polarization component (1), of the orthogonal component (2) and both (3).

$$c = \frac{I_{max}}{I_{min}} \tag{3.9}$$

of 3.64. For these measurements a prototype has been realized working on a

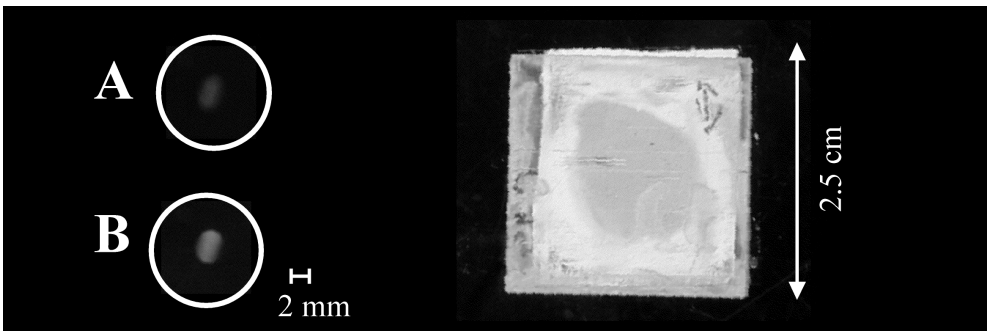

Figure 3.19: Pictures of head to head device illuminated with collimated white light seen through orthogonal polarizer (A) and parallel polarizer (B)and superimposed picture of the whole cell seen between crossed polarizers.

large area of several millimeters and allowing macroscopic view of its efficiency. By restricting the angular distribution of the source using two diaphragms of 2 mm separated by a distance of 130 mm (F# ∼33) pictures of the device have been taken with parallel and orthogonal orientation of the analyzer to see the realized contrast. These two pictures are shown on the right hand side of Fig. 3.19 while on the left hand side a picture of the whole device between crossed polarizer can be seen. The case of intensity transmission with only the polarizer of reference is not pertinent since the light distribution at the output of the device is no more collimated. Note that the beam can be collimated by addition of another lens array with half the pitch of the first arrays. Losses due to the degree of coherence of the source (interferences, diffraction) are not discussed in this paper.

3.7 Conclusion

It has been demonstrated that polarizing micro-optical elements allow creating new non-conventional optical elements. Integrated in systems, special functions like a micro-optical polarizer can be realized. The specific interest lays in the possibility to produce devices with wafer technology. We realized a prototype with miniaturized optical components that is only 2 mm thick. The gain in the polarization efficiency is over 45% for collimated white light. Strong improvements could be realized using AR coating on both sides, by increasing the homogeneity of the alignment of the Liquid crystal molecules and by increasing the TN cell height [27]. Aspheric microlenses could be used to increase the acceptance angle. Moreover a third microlens array could be added to the head to head configuration to improve the collimation of the light at the output of the system.

Chapter 4

Moiré magnifier

4.1 Introduction

This chapter concerns an interesting visual application of microlens arrays. Using a repetitive pattern of a scale down image and a microlens array, a magnification of this image can be displayed. The magnification and the orientation of the image can be chosen by simply rotate the microlens array. This property allows interesting design application in thin and flat devices. To ensure a strong integration of the overall system, we focus our analyze to high resolution moiré magnifiers using microlens arrays having heights of only few tens of microns and diameters between $150 - 360\,\mu m$. From the equations developed in [38] we give a method to design moiré magnifiers and explore their image quality through fabricated samples.

4.2 Moiré phenomenon

The moiré phenomenon is a well known phenomenon which occurs when repetitive structures are superposed or viewed against each other. It consists of a new pattern of alternating dark and bright areas which is clearly observed at the superposition, although it does not appear in any of the original structures [39]. This effect is mainly used in metrology since it allows weak deformations to be easily detected [40, 41].

4.3 Moiré magnifier

The principle of a moiré magnifier is to use a first object made up by the periodic two-dimensional repetition of a certain image and its interaction with a matrix of microlenses of slightly different period. The figure created at the time of

the superposition of the two elements is a magnified image of the repetitive structure visualized through the microlenses.

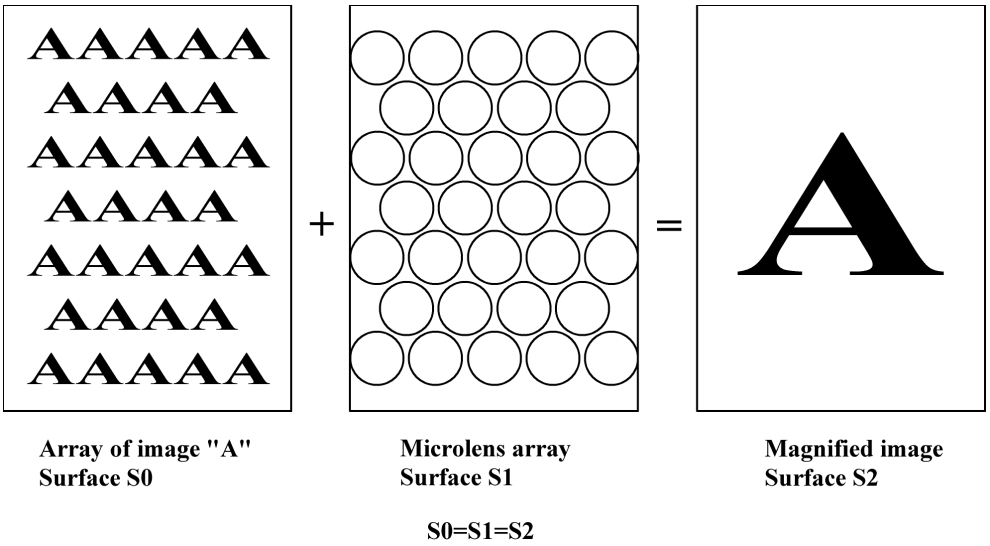

Figure 4.1: Illustration of the different elements constituting the moiré magnifier. On the left the object array, in the middle the microlens array and on the right the magnified image obtained when superposing both elements.

Figure 4.1 shows the different elements constituting the moiré magnifier and the resulting magnified image. Each lens carries out a magnified image of a different part (white area) of the object as seen in Fig. 4.2. When the sampling of the different parts of the pattern is adapted, all the images formed by the matrix of microlenses combine themselves in a contiguous way to form the complete image of the magnified pattern. Since an image formation occurs, two distinguished cases are possible depending on the position of the object compared to the focal length of the microlenses. A virtual magnified image appears when the object position S_o is lower than the focal length f of the microlens i.e. $S_o < f$ and a real but inverted image appears for $S_o > f$. The different elements required for a moiré magnifier are illustrated in Fig. 4.1. The moiré magnifier effect imposes dimensions in the same order for the array and the magnified image. In the idea of displaying a magnified image of the object, no advantage is then obtained since the pattern could directly be written on the surface at disposition. Nevertheless a moiré magnifier is an innovative way to magnify and demagnify a fixed image with an overall thickness of the resulting device of only few millimeters. Only a simple rotation of the microlens array over the repeated pattern is required (see section 4.5.2) [38]. This allows interesting visual applications in thin and flat systems. Others interesting applications are found in security systems for official documents [42]. The high quality resolution required for the repeated pattern do not allow being easily copied and different

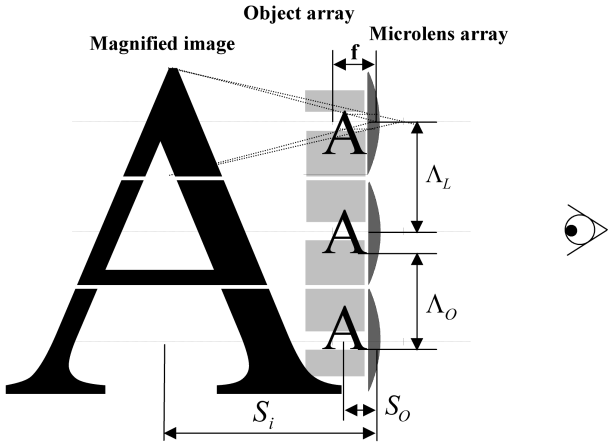

Figure 4.2: Geometrical construction of the moiré magnifier effect. Each magnified part of the object "A" (white areas) combine themselves in a contiguous way to form the complete magnified image. The object "A" is sketched out of plan for understanding purpose. It should be parallel to the plan of the microlens array. f is the focal length, Λ_L is the pitch of the microlens array, Λ_O the pitch of the object array and $S_o$the object position. The illustrated case corresponds to the case of a virtual image where $S_o < f$.

encoding of the information could be realized. A well known application of moiré magnifier concern a peculiar case known as Gabor superlens which uses two arrays of microlenses instead of one repetitive image and one microlens array. This system has been well studied in [43] and applications are commonly found in photocopier and facsimile machines [44].

4.4 Design considerations

The moiré magnification effect appears for elements with close pitches [38]. The pitch of the object array can be assimilated as a first approximation to the pitch of the microlens array. Then to avoid crosstalk between objects, the maximum surface available to write the initial image corresponds to the lens aperture, which defines the unit cell of the pattern. As an example a common microlens array with a diameter of microlenses of $\emptyset_L$ imposes the image to be scale down to the dimension $d = \emptyset_L$ resulting in a high quality printing (24000 dpi). The next important parameter is the wished size of the magnified image D. Both dimensions d and D are connected through the pitches of their arrays by the magnification factor m [38]

$$m = \frac{D}{d} = \frac{\Lambda_L}{\triangle\Lambda}, \tag{4.1}$$

where Λ_L is the pitch of the microlens array, Λ_O the pitch of the object array. In the case where several images are encoded in the same array (for instance the letters "A" and "B" in Fig. 4.3), Eq. 4.1 is rewritten in the form

$$m = \frac{\Lambda_L}{\Lambda_L - N \cdot \Lambda_o}, \tag{4.2}$$

where $N = n + 1$ and n equals to the number of added images. The pitch of the object array is always defined by the periodic distance between two images independently of their type. On other words, it represents cases of object arrays with pitches divided by N or a number of objects per pitch equal to N. In the present case the object size fills up the lens diameter, i. e. n=0, and N=1. All the different geometrical parameters are shown in Fig. 4.3. A scaling factor F

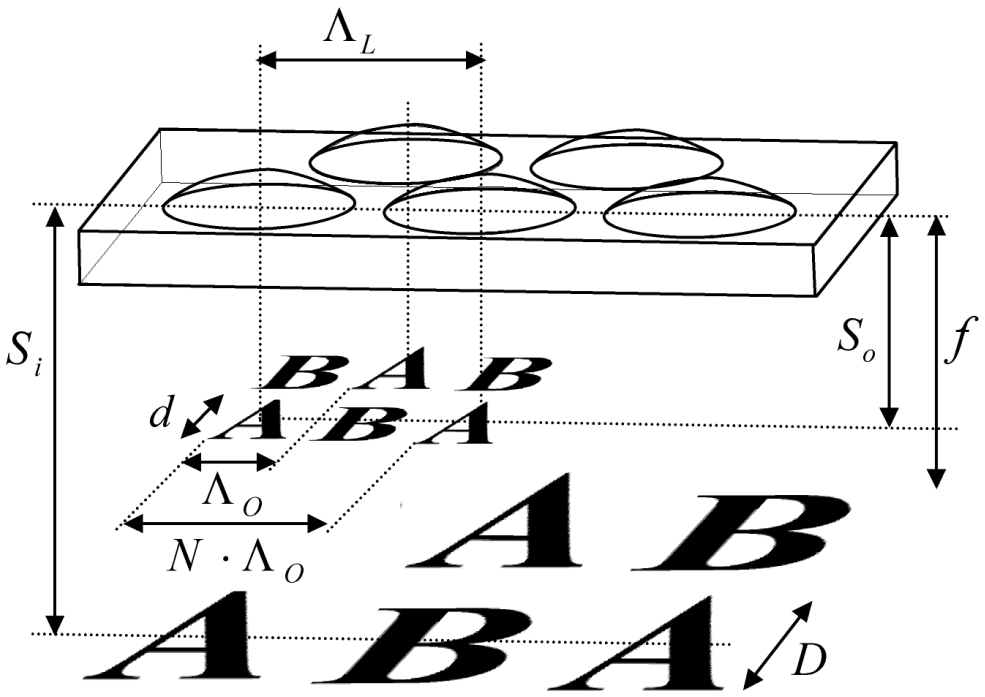

Figure 4.3: Schematic view of the moiré design parameters. f corresponds the focal length of the microlenses, Λ_L to the pitch of the microlens array, Λ_O to the pitch of the object array and S_o to the object position. D corresponds to the size of the magnified image while d is the size of the repeated object.

between Λ_L and Λ_O is defined by

$$F = \frac{\Lambda_O}{\Lambda_L}, \tag{4.3}$$

which becomes with Eq. 4.1

$$F = \frac{m-1}{m} \cdot \frac{1}{N} \,. \tag{4.4}$$

For the microlens array defined above and for a final size D = 2 cm, we get from Eq. 4.1, m = 137.9 and from Eq. 4.4, F = 0.9927. With conventional design mask software (Expert), arrays of the image with a pitch scaled down by F are realized.

4.5 Image quality

4.5.1 Image formation

A main concern is the image quality. As mentioned previously in the design consideration the pitch of the microlens array is taken to be higher than the pitch of the object array which is scaled down by F. This choice can be explain by the wish of the best image quality. Each microlens forms a local magnified image of the object. If the pitch of the microlens array is smaller than the pitch of the object array, we get an inverted magnified image as seen in Fig. 4.4 . The reason

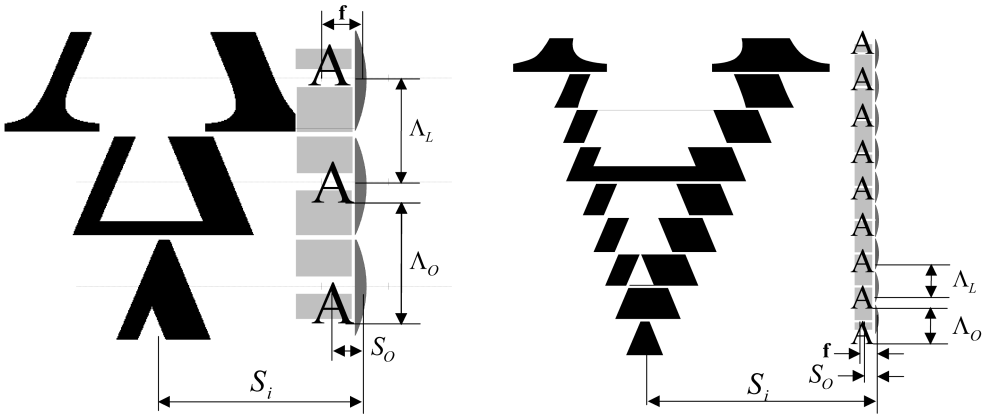

Figure 4.4: Schematic view of the image formation for the case of pitch of the microlens Λ_L smaller than the pitch of the object array Λ_O. This drawback is strongly reduced when the number of microlenses participating to the image formation increases as seen on the right part of the figure. The illustrated case corresponds to a virtual magnified image where $S_o < f$.

is that the different partial images are aligned in the wrong order. If only a few lenses contribute to the imaging, then the quality of the generated image is bad (Fig.4.4 left). If many lenses contribute, the general quality improves (Fig.4.4 right). In the case of an imaging system, the magnification m is determined by the object distance S_o and the focal length f (Newton's equations):

$$m = -\frac{f}{S_O - f}\,. \tag{4.5}$$

An error on m would lead to a new position of the object S_o, f being fixed by the microlens array. This consideration on the image quality of the moiré magnifier is shown in Fig. 4.5 A good contrast is obtained if the difference to

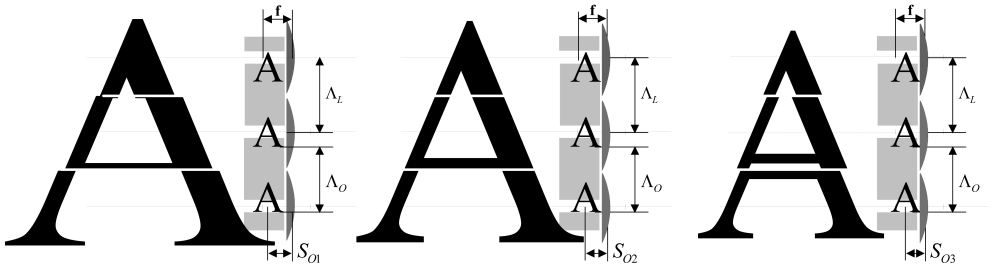

Figure 4.5: Schematic view of the image formation. On the left the case of a too large optical magnification where the local magnified images do not superpose them in a correct way, in the middle the case of a perfect image formation where the distance S_{o2} is adapted to the factor of magnification m and the last case showing a too small optical magnification. Practically the system was limited by its depth of focus, but this consideration could be important for microlenses having low numerical aperture.

the initial object position S_o does not exceed the depth of focus δz of lenses evaluated using the standard Rayleigh criterion:

$$\delta z = \frac{\lambda}{NA^2}, \tag{4.6}$$

where λ is the wavelength of the illumination and NA the numerical aperture of the microlens given by

$$NA \approx \frac{r}{f}\,. \tag{4.7}$$

For a wavelength λ fixed to 500 nm and r to 72.5 μm we obtain for a microlens array replicated in UV glue NOA 65 with refractive index of n=1.52 a focal length $f = 222\ \mu m$. The numerical aperture stands from Eq. 4.7 to NA=0.31 and the depth of focus (Eq. 4.6) $\delta z = 5.5 \mu m$.

Because of the choice of microlenses, i.e. lenses of small diameter, for high magnification, a large number of microlenses participates to the magnified image. Then the imaging properties of the system can be approximated to images of magnified points as seen in Fig. 4.6 . From diffraction theory the minimum

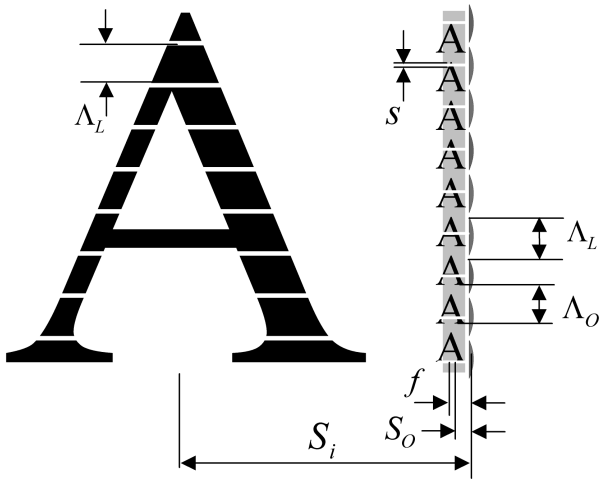

Figure 4.6: Schematic view of the image formation for the case of a very high magnification m, where the pitch of the microlens Λ_L very close to the pitch of the object array Λ_O. The sampling s of the object corresponds to the portion of the object which has to be magnified by the microlens to complete the moiré image formation. If the sampling s is smaller than the resolving power of the microlens no more details are added to the resulting magnified image and the system can be considered as a point imager.

distance between two points being solved by a lens is given by

$$\emptyset_{AD} \approx 1.22 \cdot \frac{\lambda}{NA} \,. \tag{4.8}$$

Taking the same parameters as before we find $\emptyset_{AD} = 2\,\mu m$. The sampling s corresponding to the part of the object which has to be magnified by a single lens and is given by

$$s = \Lambda_L - (\Lambda_L \cdot F) = \frac{\Lambda_L}{m} \,. \tag{4.9}$$

For the system under consideration (m = 137.9) we find a sampling $s = 1.08\,\mu m$. This value is inferior than the resolving power of the microlens. In that case, a high magnification is achieved but no more information is added to the magnified image (since m = 75 in our example). It also means that the formed image at each microlens is an Airy function of diameter: $m \cdot \emptyset_{AD}$. This interpretation explains the strong magnification that can be achieved with only low alterations in the quality of the magnified image because each microlenses does no more carry out spectral information but only local intensity (image of black or white parts). Moreover, the higher the magnification, the larger is the number of microlenses participating to the magnified image. Therefore, the local defects are contained on small zones compare to the whole magnified image.

A typical defect is about the precision of the pitch of the two arrays. From Eq. 4.1 one sees that a weak variation of the relative step of one of the arrays leads to a different magnification m. By writing the derivative of Eq. 4.4 one finds,

$$\frac{\delta F}{\delta m} = \frac{1}{m^2} \cdot \frac{1}{N} \,. \tag{4.10}$$

Taking the local difference and N=1, we get

$$\Delta m = m^2 \cdot \Delta F \,. \tag{4.11}$$

Considering that only neglectible changes on the image dimensions occur, the variations on the final dimensions of the magnified image become,

$$\Delta D = \Delta m \cdot d \,. \tag{4.12}$$

It follows from Eqs. 4.11 and 4.12 that a higher magnification factor m yields to a higher sensitivity of the ratio F between both pitches. Taking our last example and choosing a local error of $\triangle F = \pm 0.001$ we find $\triangle m = \pm 19$. This drives to $\triangle D = \pm 2.757$ mm, which corresponds to 13,7 % of the final size D. This effect has to be taken into consideration when designing a system to ensure the right magnification in presence of variations on positions and sizes that occur during the fabrication of the different elements. It is also an important result when using microlens arrays made by soft embossing techniques where variation of pitches are often present due to local variations on the hardness of the mold or in the applied pressure. This error on the factor of magnification m also leads to a new distance between the lenses and the object as discussed before. It forms at the place where the pitch is deformed, a local blurring effect. Because the magnified image results from magnification of local parts of the different local images, an overall averaging of all contributions is made. It explains why the system easily supports local defects that can occur during the printing of the object array. With pictures of realized samples, the discussed key points on the image quality can be evaluated. It has to be noticed that only cases of virtual images allowing a high magnification have been tested. Focusing is then not easy to achieve with a camera because the erect image is located behind the microlens array. Firstly the increase of the sensitivity of local pitch deformations are illustrated through the three pictures in Fig. 4.7 showing two magnification factors for microlenses replicated in UV glue and accurate reference sample in quartz. The quality of the printing of the array is also a way to increase the general quality of the magnified image.

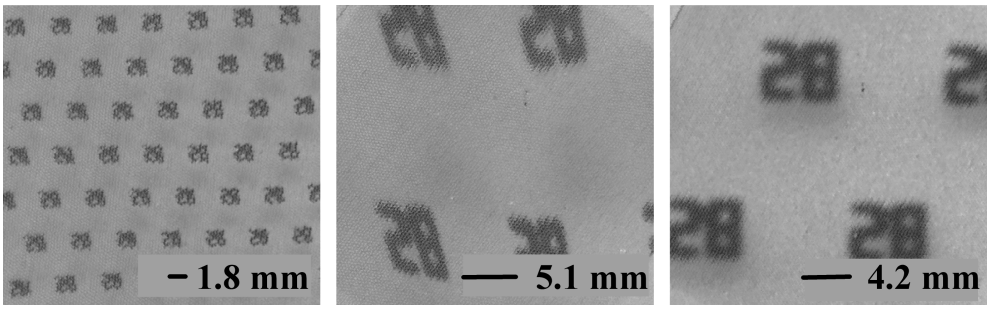

Figure 4.7: Pictures of local deformation of the pitch on the microlens array for two magnifications $m \approx 21$ (left) and $m \approx 60$ (middle). The strength of the deformations on the visual effect depends on the magnification factor m. The right picture has been taken with the master of the microlens array where no deformations are present $m \approx 46$

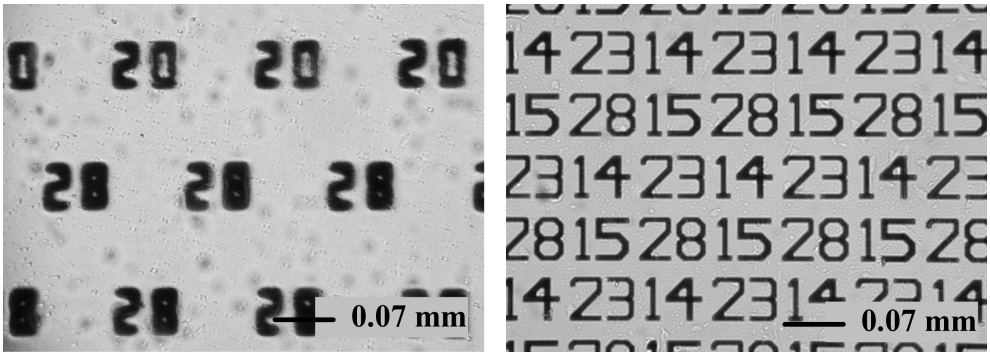

Figure 4.8: Pictures taken with a microscope of high resolution printing on plastic sheet on the left and patterned chromium on glass (photolithography mask) on the right. Several local defects are visible on the high resolution printing on plastic. Nevertheless by averaging of the different contributions of the microlenses high magnification with high image quality can be achieved as seen in Fig. 4.10.

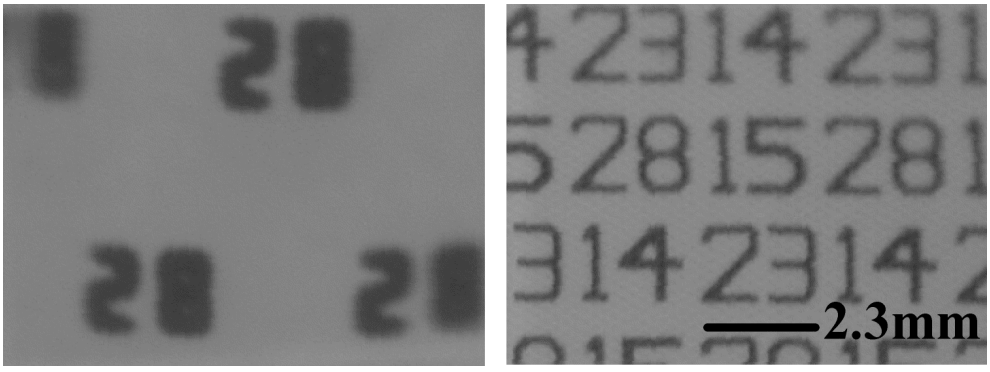

Figure 4.9: High resolution moiré magnifier, the left picture shows results for high resolution printing on plastic and at right a chromium pattern on glass ($m \approx 35$). The pitch of the microlens array is $\Lambda_L = 250\,\mu m$ and the ROC = 0.315 mm.

This is illustrated in Fig. 4.8 with two pictures of printed numbers 28 on a plastic sheet and a high resolution patterned chromium on glass. The results using this two objects are seen in Fig. 4.9. The case of a high magnification over the resolution limit of the microlens is shown in Fig. 4.10

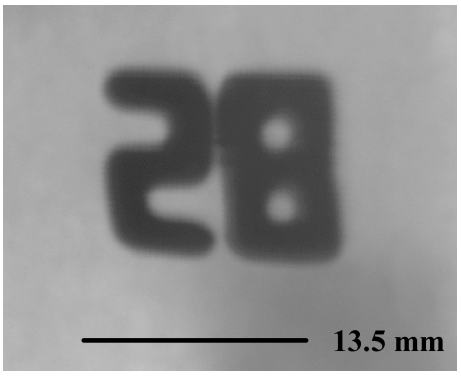

Figure 4.10: Picture of a highly magnified image $m \approx 95$ *from high resolution printing on plastic. The width of the number in the object array is* $106\,\mu m$*. Except a slight distortion visible on the bottom left part of the number, the picture shows that high image quality can be achieved even for high magnification.*

4.5.2 Parallax and orientation

The system also shows a strong parallax [45] leading to a stereoscopic vision which is sometimes disturbing when the object and the microlens arrays are not parallel. This 3D impression cannot be transmitted in pictures of realized systems. This impression can be decreased by employing microlenses with high numerical aperture or by reducing the factor of magnification. From Fig. 4.11 we can define the difference of the position seen by the two eyes looking at the same microlens

$$d_4 = 2 \cdot f \cdot \sin\left(\arctan\left(\frac{e}{h}\right)\right), \tag{4.13}$$

where e corresponds to the half distance between the eyes and set to 4 cm. The parameter h is the distance between the observer and the plan of the microlens array and set to 25 cm. Then for a displacement x of the observer looking at the same microlens a scan over the distance d_3 occurs. Again from Fig. 4.11 we obtain the following formula:

$$d_3 = f \cdot \left[\sin\left(\frac{e+x}{h}\right) - \sin\left(\arctan\left(\frac{e}{h}\right)\right)\right]. \tag{4.14}$$

Using values defined above for the e and h parameters and values determined previously in our example, we found for a displacement x = 4 cm, $d_3 = 0.067$mm.

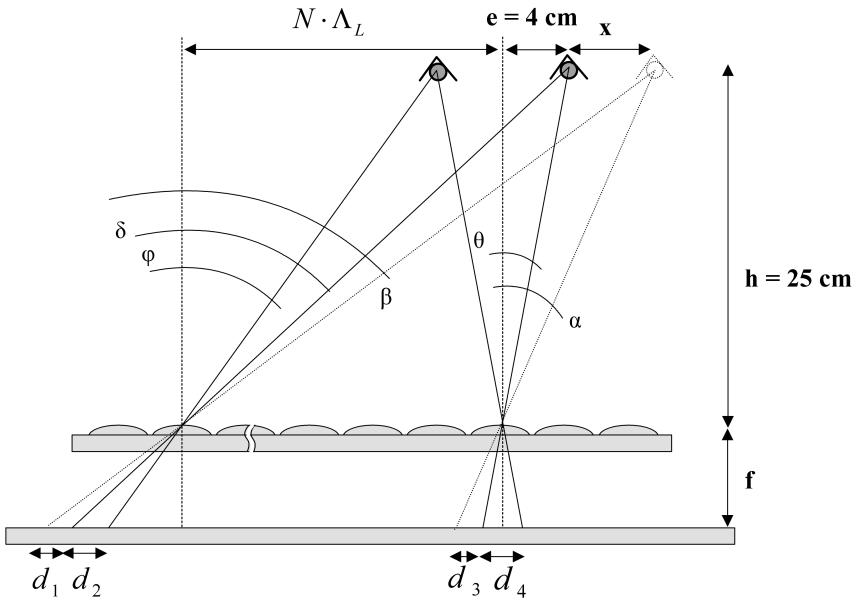

Figure 4.11: Interpretation of the parallax effect which occurs for microlenses with small numerical apertures. The distance e corresponds to half the distance between the eyes of an observer and is set to 4 cm. The observing distance h is set to 25 cm. The distances d_1 and d_4 correspond respectively to the parallax of the system and d_2 and d_3 to the scanning that occurs for a move over a distance x of the observer at two different locations on the microlens array.

This corresponds almost to the radius of the microlens. This explains the need to write the whole object and not only the sampled part s shown previously in Fig. 4.6 behind each microlens to avoid losses in the field of view when moving the head or the sample. This could be reduce by using microlenses with higher numerical apertures as mentioned previously, but harder to realized with the same optical quality (see introduction). Then encoding of several local images could be performed as well as a magnification of the objects which could contain more details but which should again be restricted to the scanned surface defined by the desired field of view.

This parallax leads to another disturbing behavior of the image which appears to travel in the same direction than the movement of the observer when microlens array and array of objects are parallel. This is no more the case for a rotation of the microlens array. The explanation is found by seeing Fig. 4.12 and especially the left part of the figure where a horizontal displacement of the sampling points (small circles) leads to a vertical displacement in the sampling of the object because of their local rotation. The same explanation is valid for stereoscopic vision, because the two images seen by the eyes are no the ones

that should be seen to obtain a real 3D impression. By the fact that the displacement on the array of objects when moving the head does not depend on the magnification factor m, Eq. 4.14, the speed ratio of this movement for two magnified images m_1 and m_2 with a same microlens array can be expressed as the ratio of their magnification factors $\frac{v_1}{v_2} = \frac{m_1}{m_2}$.

The moiré magnifier is an interesting way to magnify and demagnify a fixed image simply by rotating one array to the other. This does not only drive to a magnification demagnification of the object but also to a rotation of the image. To simplify and follow the explanations above for high magnification moiré, the system can be seen as a sampling device. When rotating the microlens array with an angle θ with respect to the object array, the sampled points move to different locations (small circles on Fig. 4.12) on the object array. The new configuration can be interpreted as a new moiré configuration with pitch $\Lambda_O^{'}$ along the axis of the lens array with a local rotation of the objects from the center of each microlens (fixed points present in the real configuration). By geometrical analysis in Fig. 4.13, the local rotation angle of the image φ is given by

$$\varphi = \frac{\pi}{2} - \theta - \arctan(\beta), \tag{4.15}$$

with the angle β given by

$$\arctan(\beta) = \frac{\Lambda_L \cdot \cos(\theta) - \Lambda_O}{\Lambda_L \cdot \sin(\theta)} \tag{4.16}$$

and the magnification factor m by

$$m = \frac{1}{1 - \left(\frac{\Lambda_L - d}{\Lambda_L}\right)}, \tag{4.17}$$

with the distance d,

$$d = \sqrt{(\Lambda_L \cdot \sin(\theta))^2 + (\Lambda_L \cdot \cos(\theta) - \Lambda_O)^2}. \tag{4.18}$$

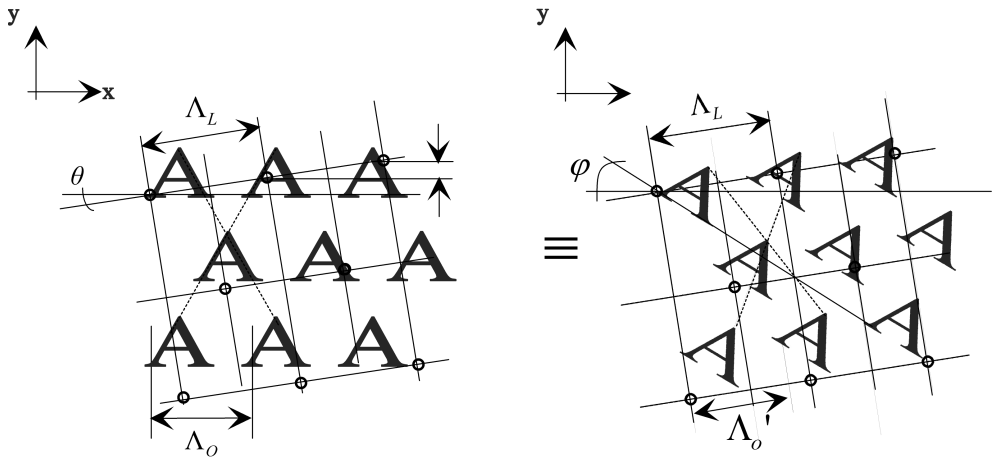

Figure 4.12: Interpretation of the local rotation of the magnified images that occurs during a rotation of one of the components. The system is reduced to a sampling system where the small circles correspond to the area of the object imaged by each microlens. The new configuration (after rotation of the microlens array (left)) can be interpreted as a new moiré configuration (right) with a pitch Λ_O' along the axis of the lens array with a local rotation of the objects from the center of each microlens. The angle θ defines the rotation of the microlens array and the angle φ, the local rotation of the objects.

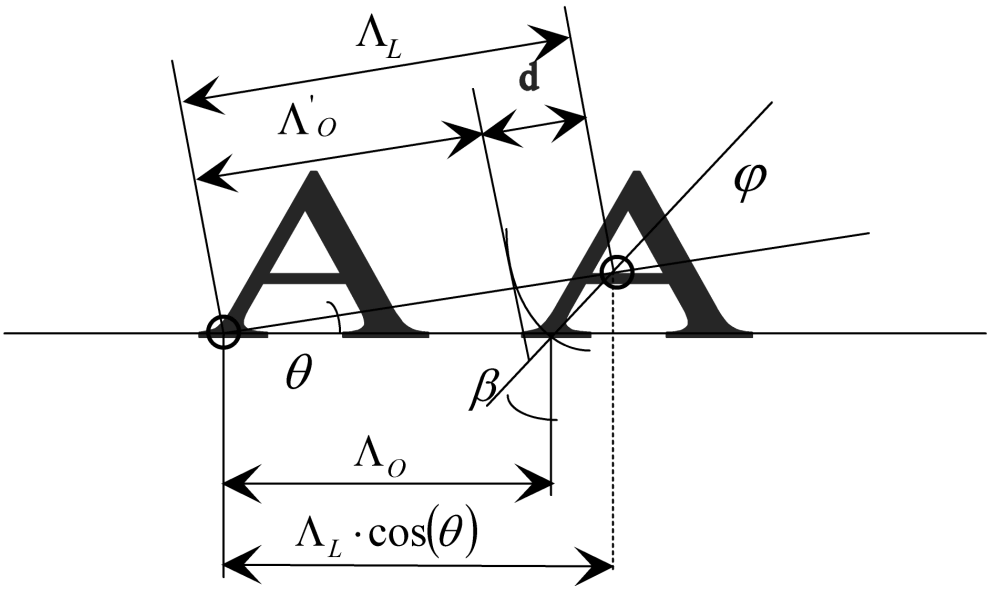

Figure 4.13: Detail of Fig. 4.12 showing the various parameters allowing calculation of the local rotation of the magnified image.

The calculated and measured magnification m and the rotation angle of the image are plotted in Fig. 4.14

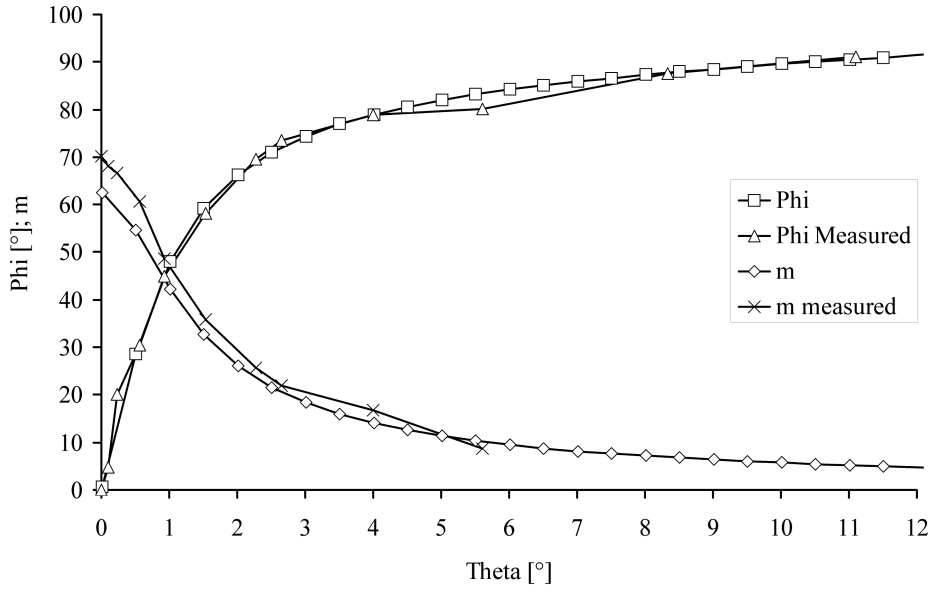

Figure 4.14: Graph of calculated and measured curves for the magnification factor m and the local angle of rotation φ.

. Figure 4.15 shows the pictures of the occurring rotation of the magnified image. A good agreement is found between measurements and calculations. A

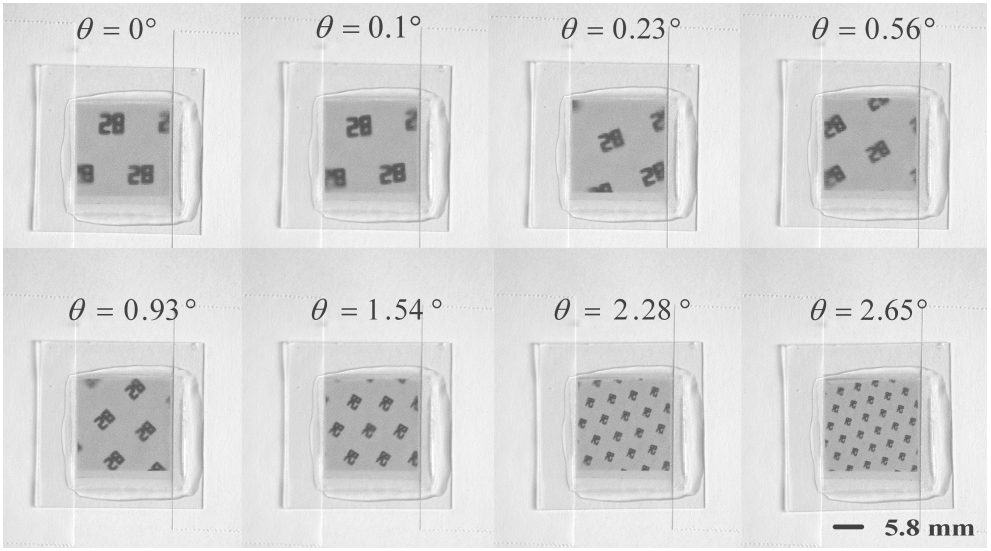

Figure 4.15: Pictures of the rotation of the magnified image (28) that occurs for a rotation angle θ of the microlens array. The pitch of the microlens array Λ_L is 250 μm .

similar interpretation of the image quality described previously in Fig. 4.6 for the case of a pitch of the microlens array smaller than the pitch of the object array can be done because the object array is not rotated in reality and the magnified and rotated image is the reconstruction of local unrotated images.

The last parameter, that must be taken into account are the intrinsic lens aberrations which are mostly responsible for the general contrast of the magnified image.

4.6 Encoding

Since one pattern can be strongly magnified m $>$ 90 as shown previously in Fig. 4.10 with help of good elements several patterns can be encoded on the area at disposal. If the size of the final magnified image takes the whole display a slight move of half the pitch of the object array for an example of 4 encoded images is enough to display another number. This would be the case in Fig. 4.16 if the field of view is restricted to the number 23 for instance. A horizontal move of half the pitch of the object array would display the number 14. Nevertheless this has to be restricted to a microlens array with high numerical aperture to reduce parallax effect and avoid unwished display of the surrounding encoded objects. Since moiré conditions i.e., moiré magnification occurs only for closed pitches (Eq. 4.1), after a rotation of only few degrees the magnification of the image decreases and the image is no more visible (Fig. 4.14 and 4.15). By addition several images can be encoded on the same array. Figure 4.17 illustrates pictures of a realized prototype showing the words "Best of IMT" for rotation of 20°, 40° and 60° of the object array. Because of non imaging but still present sampling of parts of the undesired images by the microlens array, the background seems noisy and reduces the overall contrast of the magnified image.

Figure 4.16: High resolution moiré magnifier of a chromium on glass mask (m ≈ 35*). The pitch of the microlens array is* $\Lambda_L = 250\,\mu m$ *and the ROC = 0.315 mm. If the field of view is restricted to the number 23 (middle), a horizontal move of half the pitch of the object array set to* $\Lambda_O = 247\,\mu m$ *on the left would display the number 14 (left).*

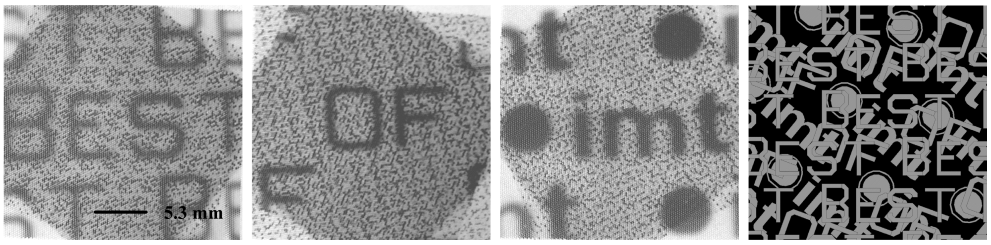

Figure 4.17: Pictures of magnified images of three objects encoded on the same array, $m \approx 55.2$. The pitch of the microlens array is $\Lambda_L = 250\,\mu m$. To display the information, the microlens array is rotated by 20° between each picture. The design of the object array is shown on the right.

4.7 Conclusion

Based on equations developed in [38] a design method for moiré magnifier is given. The different critical parameters on the image quality are discussed in detail and several illustrations of realized samples of highly integrated moiré magnifiers are shown. The encoding of several images is limited because of the parallax which allows the observer to see the images which should be hidden. Nevertheless after a rotation of few degrees, the image is no more visible (due to the decrease of the magnification). This allows encoding of several images. Because of the symmetry present in the 2D periodical arrangement of the lenses several moiré condition are retrieved (every 60° for hexagonal arrays). The angular range is then limited by the symmetry of the array. An idea would be to destroy the symmetry by building a non periodical microlens array with a corresponding scaled down non periodical object array. Taking a reasonable angular range ∼20° to display and remove the image, 18 images could be encoded on a complete rotation of 360°. Contrast problems would still be a problem as seen in Fig. 4.17. This idea could nevertheless be used in security systems where only one position and one dedicated microlens array could be used to read one encoded image.

Chapter 5

Achromatic microlenses

5.1 Introduction

The refractive index of any transparent material is function of the wavelength. Therefore, a lens made in one single material shows different positions of focus at each wavelength. The difference in position of these focal points is known as the longitudinal primary chromatic aberration [46]. To correct this aberration, achromatic lenses are usually manufactured using two lenses of different material having different Abbe numbers combined to form a doublet or even triplet [46]. This method uses the different dispersion curves of the materials to obtain, at two well separated wavelengths, the same focal length with small variations for the other wavelengths in between. By their small dimensions microlenses can have low Fresnel number and then exhibit strong diffractive effects on the position and the shape of their focal point as it has been extensively studied in literature (focal shift [47, 48, 49]). We show here that for such lenses a range for the radius of curvature (ROC) can be found where microlenses show an achromatic behavior. Firstly we focus our study on the position of the peak irradiance (Zp) for different microlenses diameters as function of ROC. The focal length is increased by increasing the ROC. However at a certain value for ROC, the focal length cannot be further increased. The limit is fixed by the position of the peak irradiance of the light diffracted by an aperture equal to the lens diameter. Secondly we study the position of the peak irradiance at different wavelengths. We observe two phenomena influencing Zp. One is the focal shift due to diffraction and the second is the chromatic aberration due to the material dispersion. Because these two phenomena have opposing influence on Zp, a choice for the ROC can be found where Zp is the same at two wavelengths. This property could be used to design achromatic lenses in one single material.

5.2 Basic considerations

The focal length of a plano-convex refractive lens is derived from the radius of curvature ROC and the refractive index n of the lens material .

$$f_E = \frac{ROC}{(n-1)}. \tag{5.1}$$

The refractive index is a function of the wavelength, whereas $n(\lambda_2) < n(\lambda_1)$ for $\lambda_2 > \lambda_1$ .The longitudinal primary chromatic aberration, corresponds to a chromatic shift of the focal length, $f_E(\lambda_2) > f_E(\lambda_1)$ for $\lambda_2 > \lambda_1$, [46]. The Fresnel number FN of a lens with a lens diameter $\emptyset = 2 \cdot \rho$ is defined by

$$FN = \frac{\rho^2}{\lambda f_E}. \tag{5.2}$$

For large Fresnel numbers FN $>>$ 1, geometric optics is well suitable to derive the focal length of a microlens. For low Fresnel numbers, the focal length is shifted towards the lens due to the influence of the diffraction at the lens stop. A Gaussian beam decomposition algorithm [50] is used for the comprehensive analysis of the refractive and diffractive properties of the microlenses.

5.3 Plano-convex refractive microlens

A plane wave with constant intensity profile illuminates a plano-convex refractive microlens as shown in Fig. 5.1. An aperture blocks the light outside the microlens. As an example, a microlens with diameter $\emptyset$=635 μm, ROC = 2.03

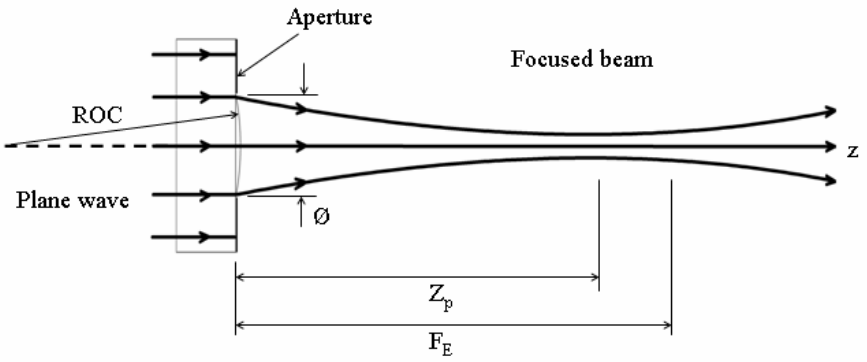

Figure 5.1: Model of a plano-convex microlens illuminated by a plane wave.

mm, made of fused silica with n (633 nm) = 1.456 has been chosen. From paraxial geometric optics, the focal length f is = 4.45 mm. The Fresnel number of the lens is FN = 35.7. As shown in Fig. 5.2, diffraction analysis [50] predicts

a position of the peak irradiance Zp at 4.36 mm. The difference between the position of the peak irradiance Zp derived from diffraction theory and the focal length obtained from geometrical optics is defined as focal shift δ [51]:

$$\delta = Z_P - f_E. \tag{5.3}$$

In the example of a microlens with a Fresnel number FN = 35.7. A focal shift of δ = -0.09 mm, corresponding to 2% mismatch is observed. This shows a good agreement between geometrical optics and diffraction theory for microlenses with large Fresnel numbers. Fig. 5.3 shows the intensity distribution

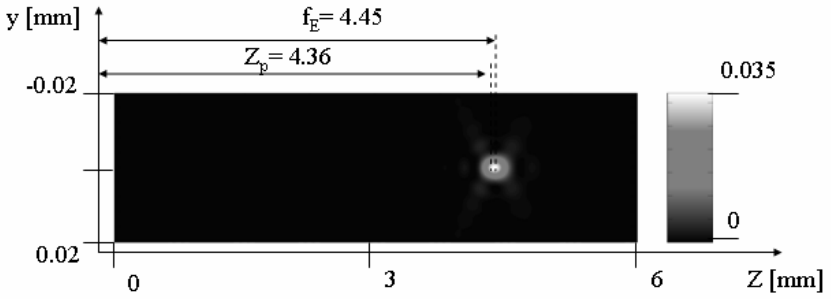

Figure 5.2: Intensity (a.u.) distribution behind a microlens of Ø = 635 μm , ROC = 2.03 mm, illuminated by a plane wave at 633 nm. The lens stands in the x,y plan while z corresponds to the propagating axis.

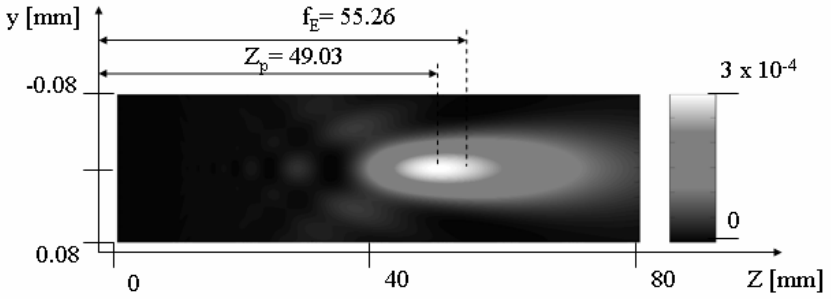

Figure 5.3: Intensity (a.u.) distribution behind a microlens of Ø = 635 μm and ROC = 25.2 mm illuminated by a plane wave at 633 nm. The lens stands in the x,y plan while z corresponds to the propagating axis.

of a microlens with a Fresnel number FN = 6.29. A focal shift of δ= -6.23 mm, corresponding to 11% mismatch is observed. Fig. 5.4 shows the intensity distribution of a microlens with a Fresnel number FN = 0.3. A focal shift of δ = -416.86 mm, corresponding to 75% mismatch is observed. Fig. 5.5 shows

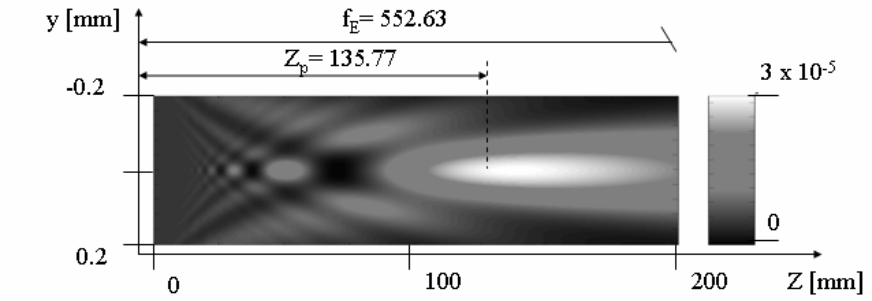

Figure 5.4: Intensity (a.u.) distribution behind a microlens of Ø = 635 μm , ROC = 252 mm, illuminated by a plane wave at 633 nm. The lens stands in the x,y plan while z corresponds to the propagating axis.

the intensity distribution behind a pinhole with same diameter. A pinhole with no refractive power corresponds to a microlens with ROC = ∞. The observed

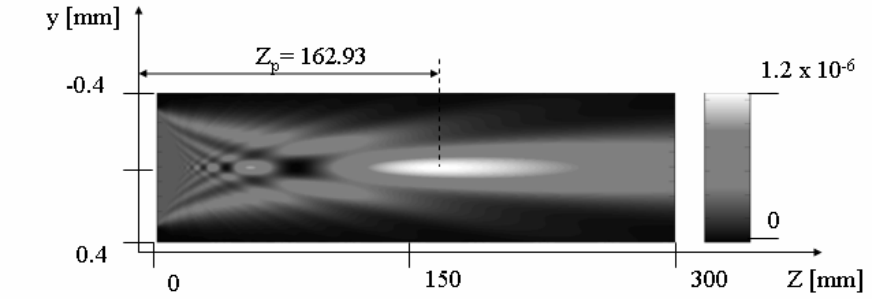

Figure 5.5: Intensity (a.u.) distribution behind an aperture of Ø = 635 μm illuminated by a plane wave at 633 nm. The lens stands in the x,y plan while z corresponds to the propagating axis.

peak irradiance position Zp = 162.93 mm is the maximum obtainable focus spot position for a microlens of Ø=635 μm diameter.

5.4 Refractive and diffractive regime

These phenomena are now analyzed for different microlens diameters illuminated by a plane wave at 633 nm. Fig. 5.6 shows Zp as a function of ROC for different microlens diameters. For low ROC (typically ROC $<$ 1 mm for Ø= 635μm microlens) the peak irradiance corresponds to the focal length obtained by Eq. 5.3. For increasing values of ROC, the peak irradiance converges to a maximum value Zp max illustrated by vertical dash lines in Fig. 5.6. This value corresponds to the peak irradiance position obtained for a pinhole with no optical power, i.e. ROC =∞. To check the validity of the present approach,

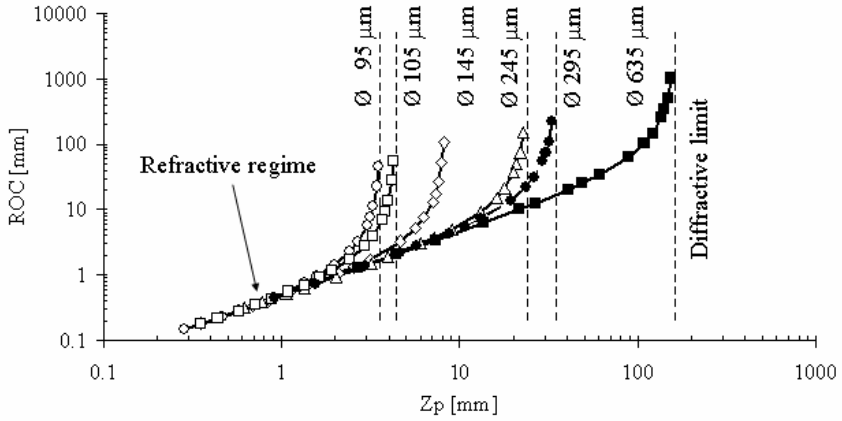

Figure 5.6: ROC [mm] versus position of peak irradiance for six diameters of microlenses illuminated by a plane wave at 633nm.

the values of Zp max obtained by the Gaussian beam decomposition algorithm are now compared to the values derived from the Rayleigh-Sommerfeld integral. The scalar field U(r,z) at the point P is given by [52],

$$U(\mathbf{r}, z) = \frac{1}{\lambda i} \int_{\Sigma} A_0(\mathbf{r}_0) \frac{\exp(ikR)}{R} \cos(\theta)\, dS, \tag{5.4}$$

(4) where Σ is the surface limited by the aperture in $z_0 = 0$. For a plane wave diffracted at the circular aperture and propagating along the optical axis we have $A_0(\mathbf{r}_0) = A_0$and $R = \sqrt{z^2 + \mathbf{r}_0^2}$ with $r_0 = |\mathbf{r}_0|$. Furthermore, for paraxial approximation we assume that $\cos(\theta) \approx 1$. Substituting these relations into Eq. 5.4 and introducing polar co-ordinates yields to

$$U(\mathbf{r} = 0, z) = \frac{A_0}{i\lambda} \int_{\varphi=0}^{2\pi} \int_{r_0=0}^{\rho_0} \frac{\exp\left(ik\sqrt{z^2 + r_0^2}\right)}{\sqrt{z^2 + r_0^2}} r_0 dr_0 d\varphi, \tag{5.5}$$

where ρ_0 is the radius of the limiting aperture at $z_0 = 0$. Integrating Eq. 5.5 and approximating the square root in the phase by the first two terms of the Taylor series yields to

$$I(\mathbf{r} = 0, z) = \left(2A_0 \sin\left(\frac{k\rho_0^2}{4z}\right)\right)^2, \tag{5.6}$$

describing the intensity distribution along the optical axis. The maximum intensity is found by setting the derivative of Eq. 5.6 equal to zero,

$$\frac{dI(\mathbf{r} = 0, z)}{dz} = -A_0\rho_0^2 \sin\left(\frac{k\rho_0^2}{2z}\right) \frac{1}{z^2} = 0, \tag{5.7}$$

which implies that $\frac{k\rho_0^2}{2z} = \pi$. The position of peak irradiance of an aperture obtained by the Rayleigh-Sommerfeld integral is

$$Z_p = \frac{\rho_0^2}{\lambda}. \tag{5.8}$$

The peak irradiance positions Zp of pinholes with diameters obtained from Rayleigh-Sommerfeld, are shown as dashed lines in Fig. 5.6. The Gaussian beam decomposition algorithm corresponds well to the Rayleigh-Sommerfeld approach.

5.5 Achromaticity

As described in the previous section microlenses exhibit a refractive regime following the linear law predicted by classical optics and a diffractive regime where the peak irradiance converges to a maximum value. As shown in Fig. 5.7, both effects are related to the wavelength . In the diffractive regime, the peak irradiance Zp is strongly dominated by the focal shift introduced by diffraction at the aperture and converges to a maximum value proportional to the inverse of the wavelength, see Eq. 5.8. In the refractive domain, the peak irradiance

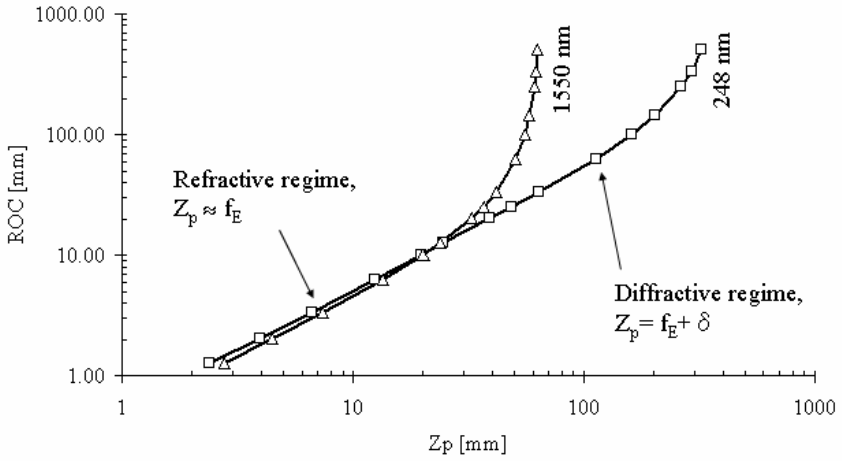

Figure 5.7: ROC versus position of peak irradiance Zp for microlenses of Ø = 635 µm illuminated by a plane wave at two different wavelengths.

Zp respectively the focal length is inversely proportional to the refractive index $n(\lambda)$. The dispersion curve of a material approximated by the Cauchy Formula [46],

$$n = C_0 + \frac{C_1}{\lambda^2} + \frac{C_2}{\lambda^4}, \tag{5.9}$$

leads to a decreasing refractive index for increasing wavelengths. In the refractive regime, the position of the peak irradiance (Zp) is equal to the focal length given by Eq. 5.1. Fig. 5.7 shows the peak irradiance position function of ROC at different wavelengths . The longitudinal primary chromatic aberration is the difference of the peak irradiance positions for different wavelengths, expressed along the optical axis [46]. In classical optics, an achromatic lens is designed to have the same focal length for two well-separated wavelengths, i.e. $\delta_\lambda = 0$. In

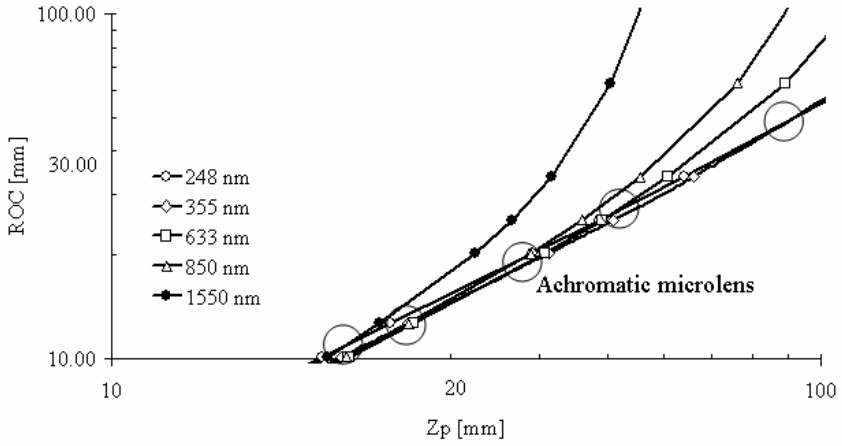

Figure 5.8: ROC versus position of peak irradiance Zp for a microlens of $\emptyset = 635\,\mu m$ *, illuminated by a plane wave at five different wavelengths. The crossings between two curves corresponding to achromatic microlenses are shown with circles.*

Fig. 5.8, we observe that for each pair of wavelengths the different graphs are crossing in one point. From the UV to the IR a value for ROC is found where the longitudinal chromatic aberrations are zero for two different wavelengths. For our example of a microlens with diameter , the peak radiance at 248 nm and 1550 nm are equal Zp(248 nm) = Zp(1550 nm) = 21.7mm for ROC = 10.8 mm, Fig. 5.7. Similar to classical achromats an achromatic microlens does not show an achromatic behavior over the full wavelength range in-between λ_1 and λ_2. The variation of achromats inside the range between these two design wavelengths is usually called secondary color aberration [46]. In classical optics the design of achromatic lenses can be made for any desired Zp. In the present case, chromatic aberrations are directly related to the diameter and the ROC as these are the only free parameters. For a fixed diameter of microlenses, the appearance of diffraction effect, used for chromatic aberration corrections, depends on the ROC as seen in Fig. 5.6. This implies for each design one position of the peak irradiance. To investigate an achromatic design for a microlens we fix a diameter. Then to allow comparisons a wavelength of reference fixing Zp is required. It is now possible to plot the relative variations of this Zp against the

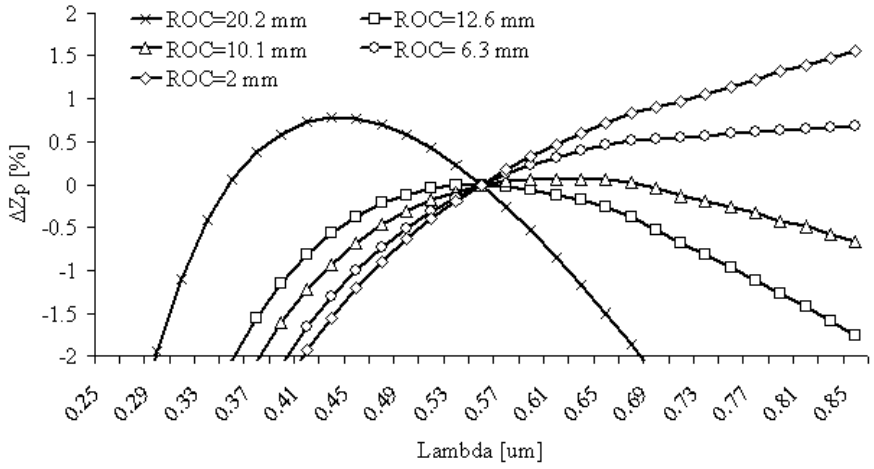

Figure 5.9: Relative variations on Zp calibrated at 550 nm for five microlenses of $\emptyset = 635\,\mu m$ for five ROC, illuminated by a plane wave at different wavelengths.

wavelength of a defined spectrum. For example, Fig. 5.9 shows the variations as function of the wavelength of Zp expressed in percent of the Zp calibrated at 550 nm. This is done for different ROC while for each lens Zp at 550 nm is taken to normalize. The effect of diffraction appears when ROC increases. Correction of chromatic aberrations is possible for curve shapes that show a maximum in the desired wavelengths region. It would seem that small curvature (large radius of curvature) of the plot at the maximum would lead to small chromatic aberration in Fig. 5.9. Curves for ROC = 20.2 mm (FN = 4), 12.6 mm (FN = 6) and 10.1 mm (FN = 8) in Fig. 5.9 show a maximum. Note, that the FN are calculated at 550 nm. The maximum shifts to shorter wavelengths for increasing ROC. The microlens with a ROC fixed to 10.1 mm shows less than 1 $^{0}/_{00}$ variation on Zp from 530 nm to 690 nm. For comparison the microlens with ROC=2 mm is not influenced by diffraction effects and shows more than 8 $^{0}/_{00}$ variations on Zp inside the same range. For this wavelengths range we see from Fig. 5.9 that the lens with ROC=10.1 mm represents an optimum design for a lens of diameter. The position of the peak irradiance is 21.5 mm.

5.6 Conclusion

It is well known from geometric optics that increasing the focal length of any lens leads to increase its ROC. This is the case for lenses having large values of FN $>>1$. By comparison, microlenses by their small diameters impose small value for ROC and then short focal length. When designing a microlens with large ROC, diffraction at the lens aperture may severely dominate the optical

properties of the microlens and limit the range of the effective focal length. The upper limit of the focal length is determined by the diffraction pattern of a pinhole with equal diameter. Moreover refraction and diffraction have opposing influence on the position of the peak irradiance when changing the wavelength of illumination. Diffraction at the lens stop can be used to correct chromatic aberration introduced from the dispersion of the lens material. For microlenses with low Fresnel numbers (FN$<$10), achromatic designs can be realized in one single material.

Chapter 6

Diffusers for optimized illuminations

6.1 Introduction

Profiles of laser beam are not homogeneous (i.e. uniform intensity distribution). As commonly described in literature they result of the combination of one or several transversal modes such as the superposition of Hermite-Gaussian types intensity distribution [53]. Nowadays micromachining manufacture requires highly homogenous beam profiles. Microlenses can successfully be ap-

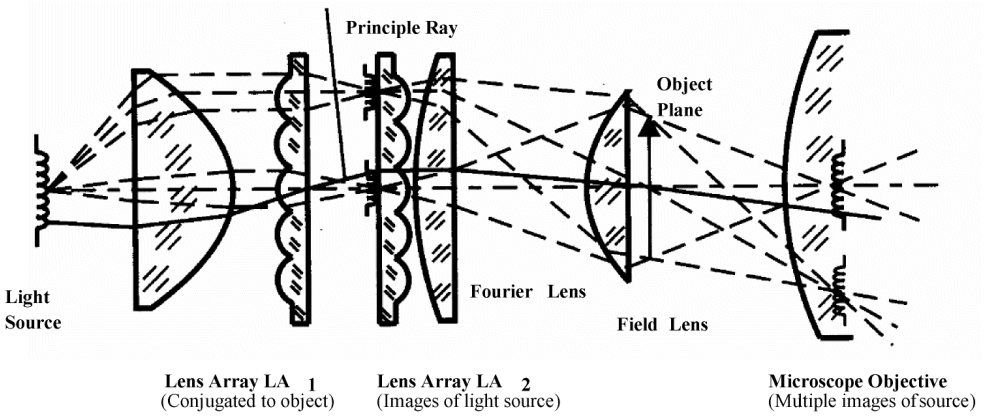

Figure 6.1: Typical homogenized microscope illumination described in the beginning of the 21^{th} century. The picture shows two microlens arrays LA_1 and LA_2 and a Fourier lens nowadays found in Fly's eye condenser for laser beam homogenizing. The object is placed in the homogenized plane of illumination and an additional field lens redirect the intensity to the microscope objective and the observer.

plied to homogenize light sources. Especially in the case of incoherent light

sources such as LEDs where arrays of microlenses can offer a space invariant solution with various aperture shapes. Nevertheless in the case of highly coherent sources they produce very contrasted diffraction pattern. One solution consist to modify spatially and temporally (at the time scale of the application) this coherence by introducing a rotating diffuser inside the optical path. To ensure a high energy throughput these diffusers should have a very narrow angular dispersion. In this chapter we present such micro-optical diffusers that have been developed to fulfill this condition.

The use of microlenses to homogenize light sources is not new. Since more than 100 years Fly's Eye Condensers are used to homogenize light emitting from a light bulb in order to efficiently illuminate extended object fields in the object plane of the microscope. This is shown in Fig. 6.1 by a drawing of a typical homogenized microscope illumination where two microlens arrays and a Fourier lens are found [54]. Similar homogenizers with microlens arrays are used today for homogenizing of a wide variety of modern light emitters from line-narrowed Excimer Lasers, laser diodes to high power LEDs. It is hence important to study their characteristics with coherent illumination.

6.2 Microlens beam homogenizers

Two main types of microlens Beam Homogenizers have to be distinguished: the Non-Imaging illustrated in Fig. 6.2 and the Imaging microlens Homogenizer illustrated in Fig. 6.3. Both types use either cross cylindrical or square microlens arrays to divide the incident beam into beamlets. These beamlets are then passed through a lens FL to be overlapped at the homogenization plane FP located in the back focal plane of the lens FL. The lens FL causes parallel bundles of rays to converge in the homogenization plane FP and is therefore called a Fourier lens. It carries out a two-dimensional Fourier transformation. The intensity pattern in the homogenization plane is related to the spatial frequency spectra generated by the microlens array(s) entering the Fourier lens. The decision whether to use a Non-Imaging or Imaging Homogenizer depends very much on the light source and the desired application. Following Dickey's [55] suggestion the Fresnel number FN should be used as a general guideline. The Fresnel number FN of a microlens beam homogenizer is defined as

$$FN \approx \frac{P_{LA} \cdot D_{FT}}{4 \cdot \lambda \cdot f_{FL}}, \tag{6.1}$$

whereas P_{LA} is the pitch of the microlens array, D_{FT} is the dimension of the flat-top intensity profile in the homogenization plane FP, f_{FL} is the focal length of the Fourier lens FL and λ is the wavelength.

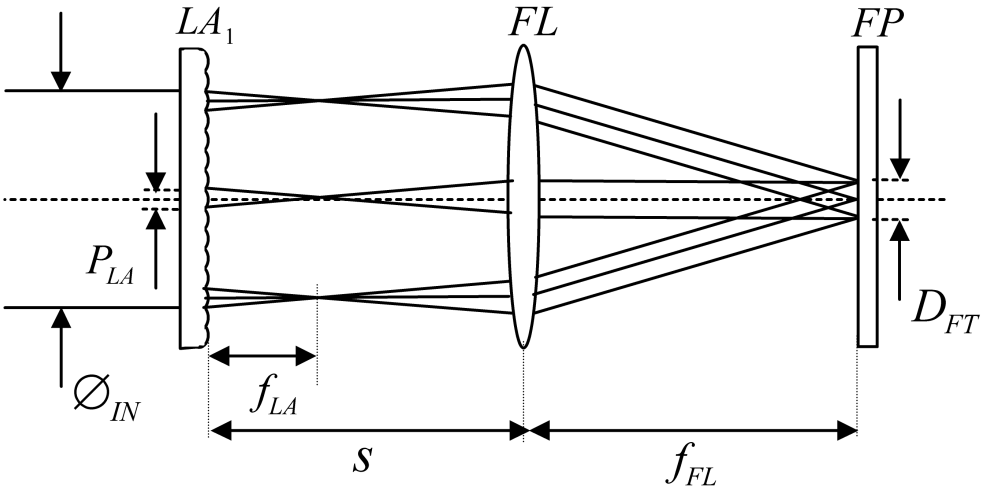

Figure 6.2: Illustration of the non-imaging beam homogenizer. In this configuration a single microlens array LA_1 divides the input beam of diameter $\varnothing_{IN}$ into several beamlets recombined in the homogenization plane FP by a lens FL. The width D_{FT} of the flat top profile intensity will depend on the pitch of the microlens array P_{LA}, the focal length of the microlenses f_{LA} and the focal length of the lens FL f_{FL}. The distance s is a free parameter.

Non-imaging homogenizers often show dominant diffraction effects due to Fresnel diffraction at the microlens array. The Fresnel diffraction is related to the Fresnel number FN. Higher Fresnel numbers give sharper edges and smaller variations of the flat-top profile. In practice, non-imaging homogenizers should have Fresnel numbers FN > 10, better FN > 100, to obtain a good uniformity. Non-imaging homogenizers are well suited for large area illumination, as the flat-top dimension D_{FT} is proportional to the Fresnel number FN. For small Fresnel numbers FN < 10 or high uniformity flat-top requirements, the Imaging Homogenizer is the preferred solution.

6.3 Design considerations

The size of the obtained flat top obtained with a non-imaging beam homogenizer is given by [55]

$$D_{FT_{NI}} = \frac{P_{LA} \cdot f_{FL}}{f_{LA}}, \tag{6.2}$$

proportional to the pitch P_{LA} of the microlens array and the focal length of the Fourier lens f_{FL} , but inversely proportional to the focal length of the microlens array f_{LA}. The imaging homogenizer uses the first microlens array LA_1 to divide the incident beam into multiple beamlets. The second microlens

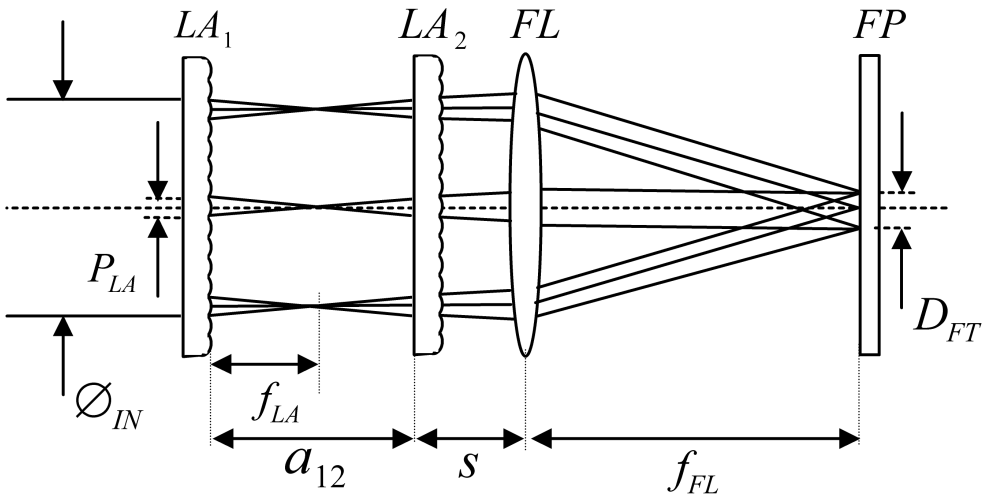

Figure 6.3: Illustration of the imaging beam homogenizer. In this configuration a second microlens array is added to the non-imaging configuration (Fig. 6.2) and creates with the help of the lens FL an array of objectives that superimposes images of the beamlets in the first array LA_1 onto the homogenization plane FP. The size of the flat top can be adjusted by modifying the distance between the two arrays a_{12}. The distance s is a free parameter.

array LA_2, in combination with the lens FL, acts as an array of objective lenses that superimposes the images of each of the beamlets in the first array onto the homogenization plane FP. The size of the flat-top now depends on the separation a_{12} of the two microlens arrays where $f_{LA1} < a_{12} < f_{LA1} + f_{LA2}$

$$D_{FT_I} = P_{LA1} \frac{f_{FL}}{f_{LA1} \cdot f_{LA2}} \left[(f_{LA1} + f_{LA2}) - a_{12} \right]. \tag{6.3}$$

This allows variations of the flat-top dimensions by shifting the position of the second microlens array. However, care must be taken not to damage the second microlens array by focusing high-power laser beams into the lens material or to generate crosstalk by overfilling the lens apertures of the second microlens array. The divergence (half angle) after the homogenized plane is given by

$$tan\,(\theta) < \frac{1}{2} \frac{(\varnothing_{IN} + D_{FT_I} - 2P_{LA})}{f_{FL}}, \tag{6.4}$$

if $D_{FT_I} > P_{LA}$ and by the approximation

$$tan\,(\theta) \approx \frac{1}{2} \frac{(\varnothing_{IN} + D_{FT_I})}{f_{FL}}, \tag{6.5}$$

when $D_{FT_I} < P_{LA}$. Usually, imaging homogenizers consist of two similar microlens arrays with identical lens pitches.

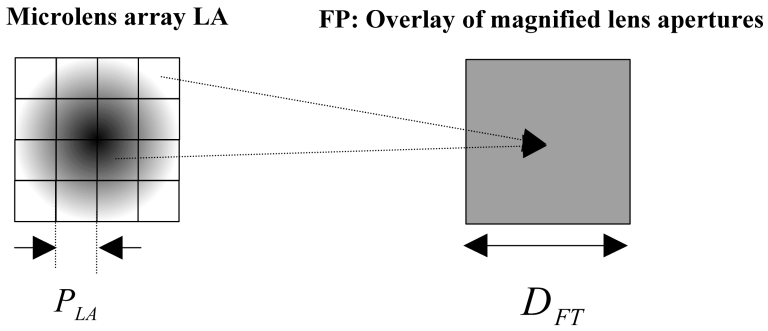

Figure 6.4: Superimposition of magnified images of channels apertures. The shape of the output intensity in FP corresponds to the shape of the microlens apertures. The width D_{FT} of the flat top profile intensity will depend on the pitch of the microlens array P_{LA}.

Square-type lens apertures generate a square flat top or top hat intensity distribution in the Fourier plane. Circular or hexagonal microlenses will generate a circular respectively hexagonal flat-top Fig. 6.4.

6.4 Beam requirements

For standard laser beams, the overlay of some 3 by 3 microlenses is usually sufficient to achieve a good flat top uniformity. Consequently, the beam diameter $_{IN}$ constrains the maximum microlens pitch $P_{LA_1} \leq \frac{IN}{3}$. Typical homogenizers use 5 x 5 to 7 x 7 microlenses. For space invariant features a larger number of microlenses is required. For imaging homogenizers the diameter of the individual beamlets at the second microlens array LA_2 must be smaller than the lens pitch to avoid an overfilling of the lens aperture and the loss of light. For a collimated laser beam, the separation of the two microlens arrays is given by $f_{LA1} < a_{12} < f_{LA1} + f_{LA2}$. For laser beams with a significant beam divergence the diameter of the beamlets at the second microlens array scales with the beam divergence. The maximum allowed beam divergence for a given microlens homogenizer is

$$tan\,(\theta) \leq P_{LA}/\,(2 \cdot f_{LA1})\,, \tag{6.6}$$

for $a = f_{LA1}$. For high-power laser beams, a focusing into the material of the second microlens array or the spherical lens must be avoided. As it will be discussed later on, an additional diffuser might be used to properly fill the aperture of the second microlens array.

6.5 Diffraction effects

For small microlens apertures with a long focal length, i.e. for microlens beam homogenizers with a Fresnel Number FN < 10, the flat top profile might be distorted by diffraction at the lens apertures. This effect is shown in Fig. 6.5 where two simulations of the intensity distribution in FP for one illuminated microlens channel having different Fresnel numbers. Thus for small laser beams a beam expander is usually the better solution than using microlens arrays with a very small lens pitch. Microlens arrays are periodic structures, where the pitch

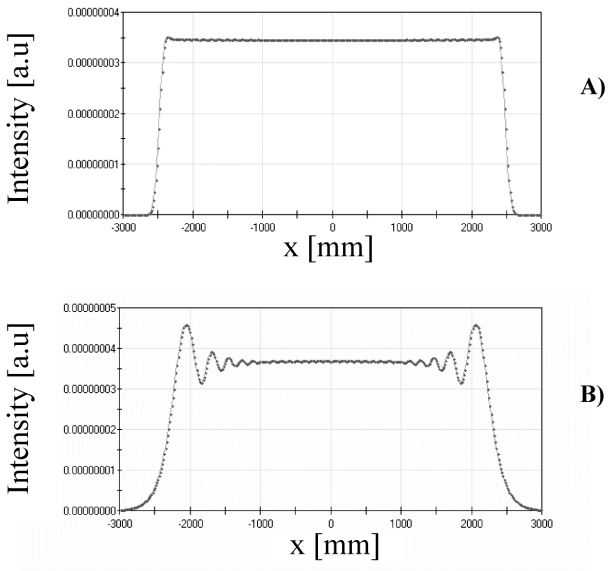

Figure 6.5: Simulations of one microlens channel intensity distribution in the Fourier Plan for two beam homogenizers with microlenses of different Fresnel Numbers: A) P_{LA}= 1 mm, FN = 272; B) P_{LA}= 0.3 mm, FN = 37 (FL = 80 mm). In the bottom simulation, the diffraction effect is enhanced and a modulation of the flat top intensity appears.

P_{LA} corresponds to a grating period. Each microlens array will behave like a diffraction grating and will generate diffraction orders with a period Λ_{FP}

$$\Lambda_{FP} = \frac{f_{FL} \cdot \lambda}{P_{LA}}, \tag{6.7}$$

in the homogenization plane FP. f_{FL} corresponds to the focal length of the Fourier lens and λ to the wavelength. This becomes a real drawback for coherent illumination. This behavior is illustrated in Fig. 6.6 for a beam homogenizer used with coherent light. The flat top intensity pattern is distorted by an array of spots with a minimum diameter δx_{min} given by diffraction at the Fourier lens:

$$\delta x_{min} = 1.22 \cdot \frac{2 \cdot f_{FL} \cdot \lambda}{\varnothing_{Beam}}, \tag{6.8}$$

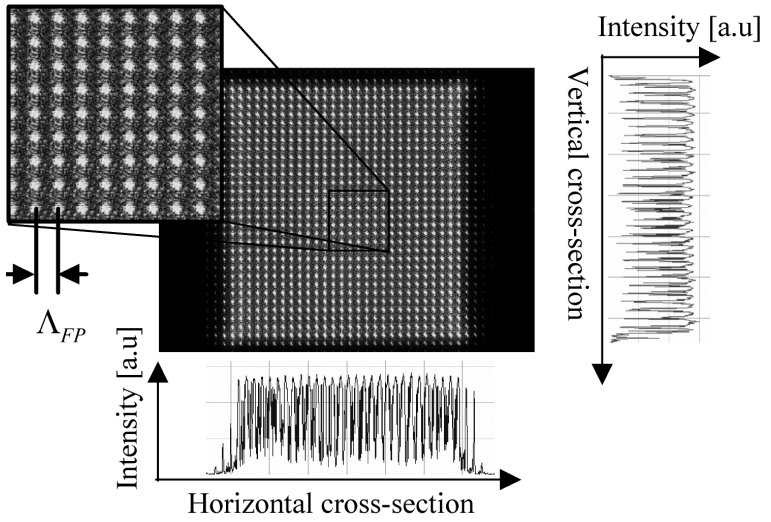

Figure 6.6: Typical diffraction pattern observed in FP for coherent light source (Laser diode Linos DS 670). The homogenization is clearly destroyed by an array of local intensity spots.

whereas $\emptyset_{Beam}$ is the diameter of beam.

6.6 Coherent illumination

To fully understand diffractive and interference effects happening in microlens beam homogenizers for coherent illumination, it is convenient to analyze the system using Fourier optics theory. It follows that the intensity pattern of the homogenized beam by a non-imaging beam homogenizer is modulated by the superposition of two effects [56]. First, the beam is modulated by diffraction at the microlenses edges. Second, an amplitude modulation appears due to interference caused by the overlapping of beams from individual microlenses. The complex 1D transmittance function of the lens array is given by the following expression [57]

$$T_{LA} = \left[\left(\left(e^{-j\frac{k\left(y'^2\right)}{2 \cdot f_{LA}}} \right) \cdot rect\left(\frac{y'}{P_{LA}/2} \right) \right) \otimes comb\left(\frac{y'}{P_{LA}} \right) \right] \cdot circ\left(\frac{y'}{N_0 P_{LA}/2} \right), \tag{6.9}$$

with p_{LA} is the pitch of the microlens array, f_{LA} the focal length of the microlenses, N_0 the number of microlenses and the wavenumber $k = \frac{2 \cdot \pi}{\lambda}$ defined at the wavelength λ. The first term corresponds to the phase factor introduced by the microlens, the second to the square lens aperture and the comb function to a train of Dirac functions spaced by P_{LA} representing the array. The last

circ function to the finite circular aperture of the input beam limiting . The output field in the target plane is given by the Fourier transform performed by the Fourier lens of the input field U_{IN} transmitted through the microlens array of transmittance T_{LA}

$$U_{FP} = FT_{FL}\left\{U_{IN} \cdot T_{LA}\right\}, \tag{6.10}$$

which can be developed in the form

$$U_{FP} \propto \left(\hat{U}_{IN} \otimes \hat{T}_{LA}\right), \tag{6.11}$$

where $\hat{U}_{IN}$ and $\hat{T}_{LA}$ represent the Fourier transform by the Fourier lens FT_{FL} of the input field and the microlens array complex transmittance. From Eq. 6.10, $\hat{T}_{LA}$ takes the form

$$\hat{T}_{LA} = \left[\left(FT_{FL}\left(e^{-j\frac{k\left(y'^2\right)}{2 \cdot f_{LA}}}\right) \otimes sinc\left(\frac{P_{LA}}{2}\frac{1}{\lambda \cdot f_{FL}} \cdot y\right)\right) \cdot comb\left(\frac{P_{LA}}{\lambda \cdot f_{FL}} \cdot y\right)\right] \tag{6.12}$$

$$\otimes Airy\left(\frac{N_0 P_{LA}}{2}\frac{1}{\lambda \cdot f_{FL}} \cdot y\right).$$

If we look in detail Eq. 6.12, the two first terms correspond to the Fresnel diffraction from the microlenses and the third term to interferences. The forth term correspond to diffraction effects from the beam size. Neglecting the field size we see from Eq. 6.11 that the field is the result of the convolution between the angular spectrum of the input field and a modulated comb function $\left(\hat{T}_{LA}\right)$ with period $\lambda \cdot f_{FL}/P_{LA}$. The shape of each intensity spot is a function of the angular spectrum of the input field. So when modifying the plane wave spectrum of the source with a diffuser, modifications on the intensity in the Fourier plan FP will occur.

In the case of the imaging system with two microlens arrays, we follow the ideas given in [58] and used the propagation of the plane wave spectrum of the input field. The method is well suited because it allows a complete separation of the effects of the array and of single microlens channels. To fully understand this approach it is convenient to start again with the case of the non-imaging beam homogenizer with a single microlens array. Firstly using an monochromatic input field of the form

$$U_{in} = a\left(\alpha\right) \cdot \exp\left(iky' \sin\left(\alpha\right) + \phi\left(\alpha\right)\right), \tag{6.13}$$

where α is the angle of propagation of the plane wave and the amplitude $a(\alpha) = 1$ and $\phi(\alpha) = 0$ is the phase shift. The resulting field in the focal plane of the Fourier lens FP for a non imaging beam homogenizer can be expressed, neglecting the finite aperture of the Fourier lens FL, by

$$U_{FP}(\alpha) = FT_{FL}\left\{|U_{in}(\alpha)| \cdot \exp(iky' \sin(\alpha)) \cdot \sum_{l=-N_0}^{N_0} \delta(y' - lP_{LA}) \cdot U_{Lens}(y')\right\}, \tag{6.14}$$

where $\sum_{l=-N_0}^{N_0} \delta(y' - lP_{LA}) \cdot U_{Lens}(y')$ represents the transmission function of the microlens array with $U_{Lens} = e^{\frac{ik}{2f_l}y'^2} \cdot rect\left(\frac{y'}{P_{LA}}\right)$. This expression can be developed using linearity and shifting properties of Fourier analysis in the form

$$U_{FP}(\alpha; y) = \left[\delta(y - f_{FL} \cdot sin(\alpha)) \otimes FT_{FL}\left\{\sum_{l=-N_0}^{N_0} \delta(y' - lP_{LA})\right\}\right] \tag{6.15}$$

$$\cdot \left[\delta(y - f_{FL} \cdot sin(\alpha)) \otimes FT_{FL}\{|U_{in}(\alpha)| \cdot U_{Lens}(y')\}\right].$$

It can be rewritten into the simplified form

$$U_{FP}(\alpha; y) = S_{N_0}(\alpha; y) \cdot U_{FP_{Chanel}}, \tag{6.16}$$

where

$$S_{N_0}(\alpha; y) = \left|\frac{\sin(N_0 \pi P_{LA}(y - f_{FL}\sin(\alpha))/\lambda f_{FL})}{\sin(\pi P_{LA}(y - f_{FL}\sin(\alpha))/\lambda f_{FL})}\right|,$$

corresponds to the analytical expression of the Fourier transform of the array transmittance $U_{array} = comb\left(\frac{1}{P_{LA}}\right) \cdot rect\left(\frac{1}{N_0 P_{LA}}\right)$ shifted by $f_{FL}\sin(\alpha)$ giving the diffraction effects of the array containing N_0 microlenses with peaks separated by Λ_{FP} given by Eq.6.7 and position depending on the plane wave angle α as illustrated schematically in Fig. 6.7.

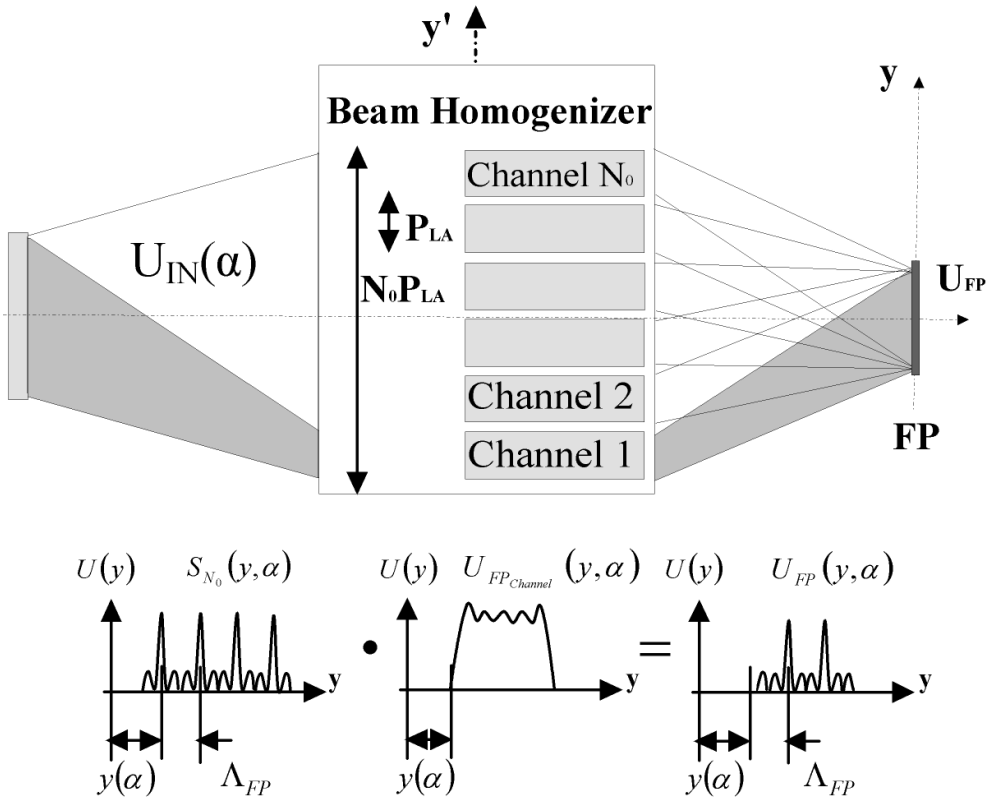

Figure 6.7: Schematic illustration of the interpretation of the plane wave spectrum applied to beam homogenizer. The beam homogenizer can be seen independently of the type (imaging or non-imaging) as an array of transmission channels. The intensity distribution will be a function of the array transmission function S_{N_0} responsible of the peaks intensity multiplied by the transmission function of a channel $U_{FP_{channel}}$.

The second term $U_{FP_{Chanel}}$corresponds to the propagation onto FP of the input wave through one microlens channel. A general broadening of the flat top can't be avoid because of the position which depend on α for both functions S_{N_0} and $U_{FP_{Chanel}}$. The overall expression of the transmitted field through an imaging beam homogenizer with two microlens arrays can be similarly described by the propagation of the input wave in one channel onto FP multiplied by the array function S_{N_0}. The channel can be considered with one or two microlenses as illustrated in Fig. 6.8. By applying the approximation to the distance between the arrays $a_{12} = f_{LA}$ and propagating the field from LA_1 to LA_2 using the Fresnel approximation of the Fresnel-Kirchhoff diffraction Integral [58] one gets

$$U_{FP}(\alpha; y) \propto S_{N_0}(\alpha; y) \cdot [sinc\left(\frac{P_{LA}}{\lambda \cdot f_{FL}}\right) \otimes \tag{6.17}$$

$$\left(|U_{IN}(\alpha)| \exp\left(ikf_L/f_{FL} y \sin(\alpha)\right) rect\left(\left(\frac{f_L}{f_{FL}}\right)\left(\frac{y}{P_{LA}}\right)\right)\right)],$$

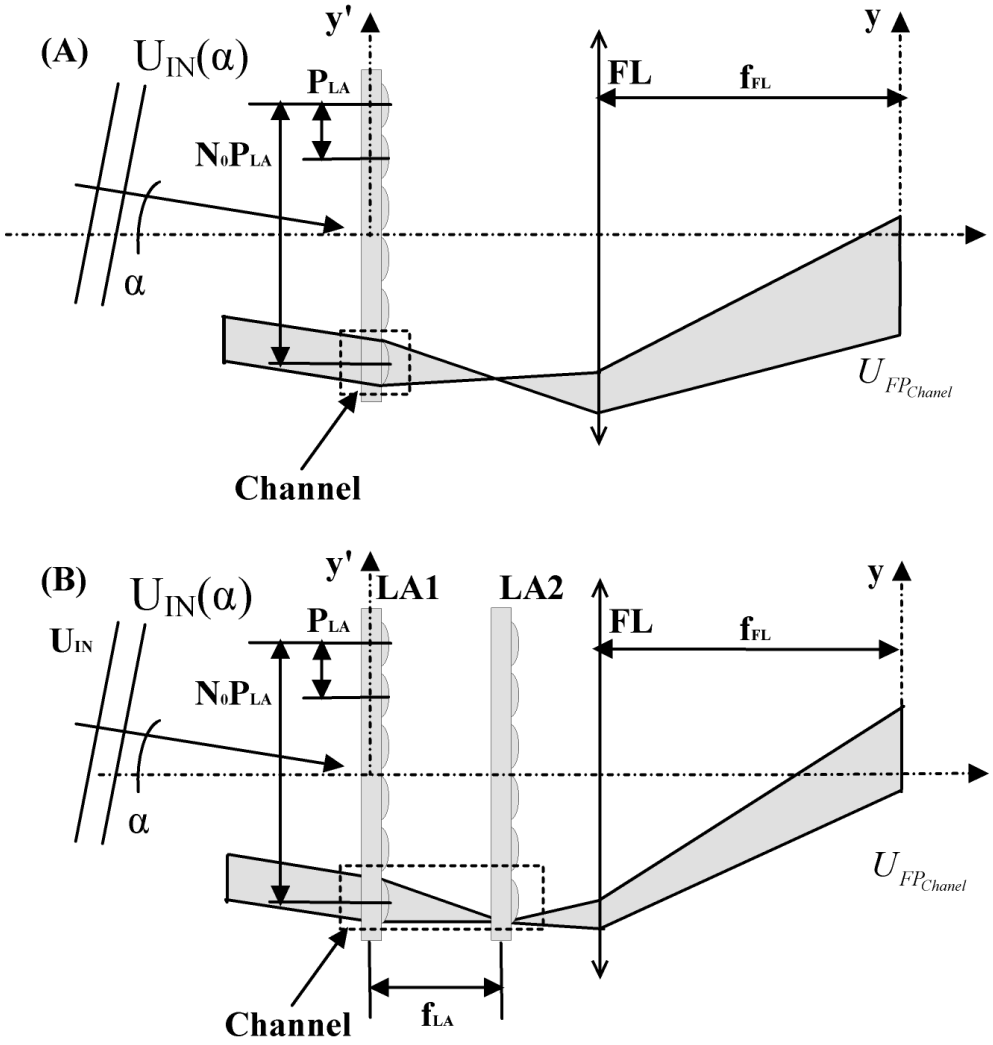

Figure 6.8: Schematic illustration of the different parameters involved in the plane wave spectrum approach of the Non-Imaging (A) and Imaging (B) beam homogenizer. $U_{IN}(\alpha)$corresponds to one plane wave component of the input field. LA_1 and LA_2 are microlens arrays. FL is the Fourier lens with a focal length f_{FL}. P_{LA} is the pitch of the microlens array and N_0 is the number of retained microlenses. To evaluate the transmission of a channel in the case of the imaging beam homogenizer, the field at the entrance of one microlens is propagated over the focal length of the microlenses f_{LA}.

where the term in the brackets after the array function S_{N_0} corresponds to the channel transmission function $U_{FP_{Chanel}}$ of the imaging configuration. The resulting intensity for a monochromatic source λ is the modulus of the coherent sum of the different plane waves contributions

$$I_{FP} \propto \left| \int_{\alpha_{min}}^{\alpha_{max}} U_{FP}(\alpha)\, d\alpha \right|^2 . \tag{6.18}$$

Because of the term S_{N_0} present in both cases of non-imaging and imaging beam

homogenizers and depending on α, the modification of the angular spectrum of the source is a way to reduce the localization of theses spots and smooth the general diffraction pattern. The imaging configuration is also less sensitive to broadening effects of the flat top profile since its $U_{FP_{Chanel}}$ is not linked to α. For coherent cw-lasers, the spatial modulation of the observed pattern can locally reach more than 100%. A rotating diffuser plate is the appropriated mean to homogenize the intensity of the flat top profile. Placing the diffuser at the focus of the beam, e.g., by using a beam expander in front of the homogenizer, changes the plane wave spectrum of the illumination by creating a new extended light source, whereas the size of the source is equal to the spot diameter on the rotating diffuser. Unfortunately rotating diffusers do not work for pulsed lasers like Nd:YAG with picosecond laser pulses. Different measures, such as stair case beam splitters [59] are applied or chirped microlens arrays [60].

6.7 Diffusers

Conventionally diffusers are obtained by mechanical methods, such as sand-blasting, which increase statistically the surface roughness of a glass plate.

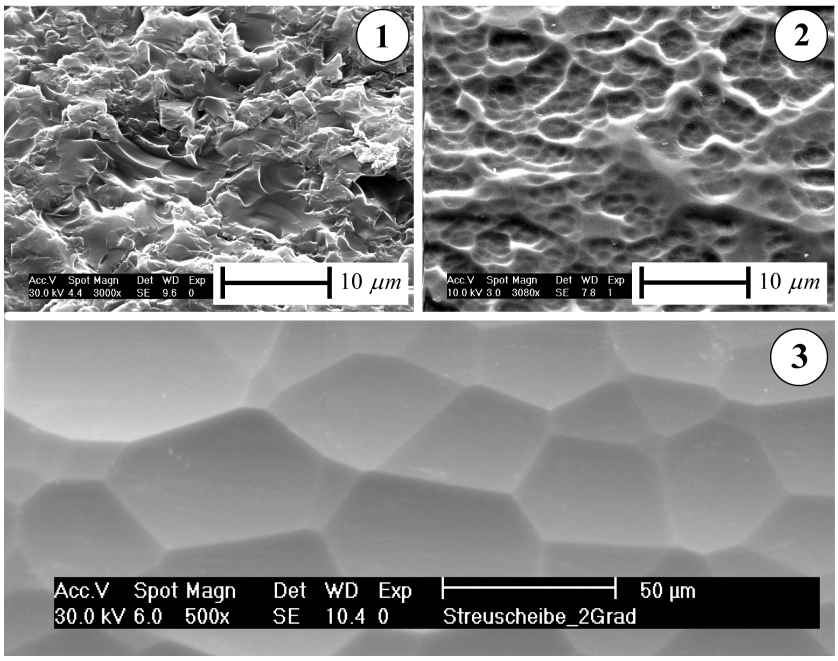

Figure 6.9: SEM pictures of a ground glass diffuser (1), E diffuser (2), HT diffuser (3).

These cheap diffusers have the main drawback of diffusing light in a very broad angular spectrum because of their sharp and fine details producing local diffraction of the input light. This behavior implies often losses of light when

employed in an optical setup. To fight this drawback we have developed two other types of diffusers, respectively called SMO E and SMO HT followed by the value of their diverging angle (e.g. SMO E 1.3°). SMO stands for Süss micro-optics. For confidential reasons no details about their fabrication are mentionned. Both diffusers obtained have smoother diffusing surfaces as shown in Fig. 6.9. The HT type diffuser is composed of several coincident concave

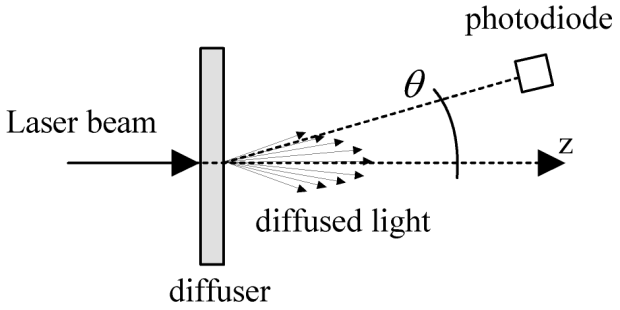

Figure 6.10: Scheme of the goniometer setup used to measure the radiation properties of the diffusers. The diffuser is static and illuminated by a HeNe laser and the light is collected by the scan of a photodiode over the angle θ.

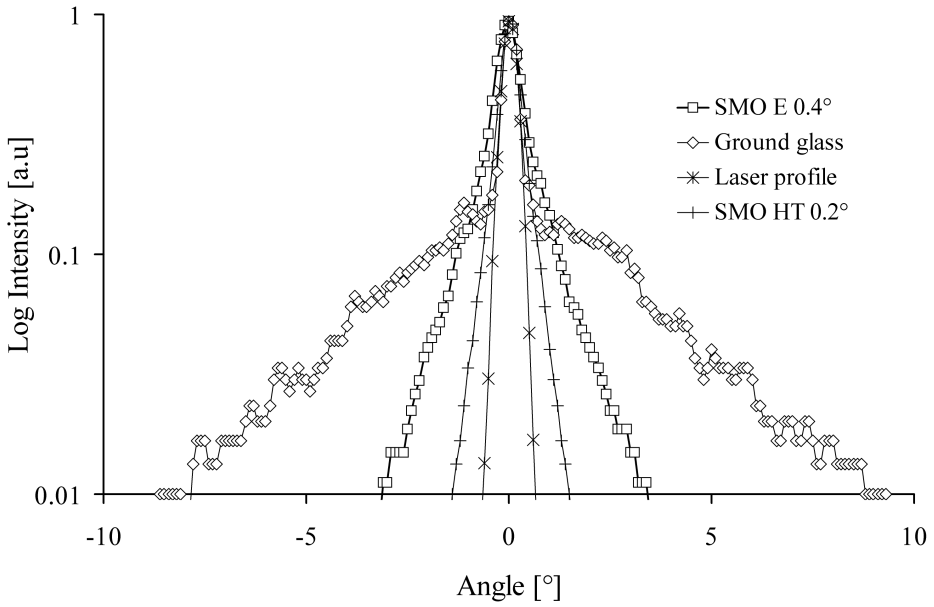

Figure 6.11: Measured angular distribution curves for several diffuser type showing the different cut-off angles and the strong zero order transmission of the ground glass diffuser.

areas reducing substantially the thin and sharp edges present in the first profile. Consequently the Full Width at Half Maximum (FWHM) angular dispersion of these diffusers is reduced. The diffusing properties are analyzed using a

conventional goniometer setup as shown in Fig. 6.10. The diffuser is lightened with a HeNe laser and the output is collected by mean of a photodiode. Results on the angular distribution are shown in Fig. 6.11.

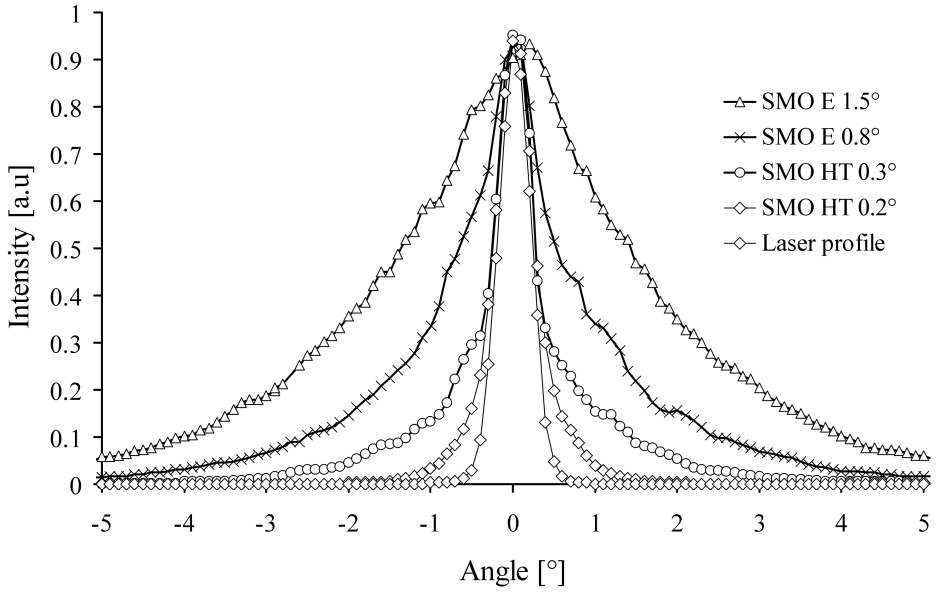

Figure 6.12: Measured angular distribution curves for diffusers E and HT with different depths of microstructures.

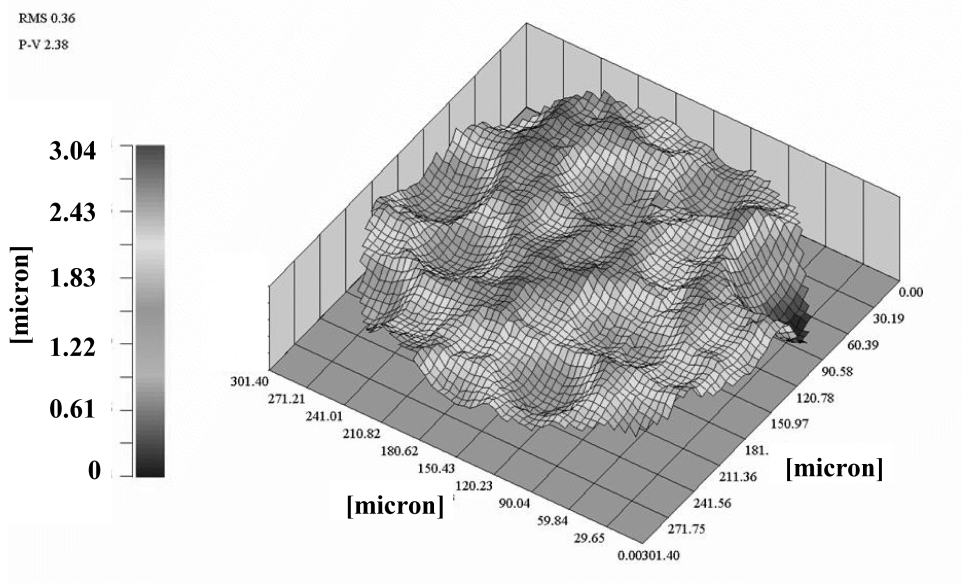

Figure 6.13: Surface profile of SMO HT 0.2° diffuser performed with a Mach Zehnder interferometer. The average depth of the microstructures lies around $1.5\,\mu m$ *and the width is about* $60\,\mu m$.

An averaging of the diffuser properties is performed because of the large illuminated area $\varnothing_{beam} \sim 2mm$ compared to the size of the microstructures

having usually several microns. All the curves have been normalized. Starting with one surface profile, diffusers with various angular dispersion properties have been realized by adjusting the depth of microstructures from few hundred nanometers to several microns. Measurements of such diffusers with various microstructure depths are shown in Fig. 6.12. The typical surface of a SMO HT 0.2° diffuser is shown in detail in Fig. 6.13 where the 3D profile is analyzed using a Mach Zehnder interferometer. It exhibits typical microstructures with concave shapes. For example the microstructures selected in Fig. 6.13 have diameters of about $\varnothing = 60\,\mu m$ with depths of $1.5\,\mu m$ corresponding to a focal length $f_l \sim -600\,\mu m$. The possibility to modify the depth of the microstructures allows fabrication of adapted diffusers to a specific design of a beam homogenizer.

6.8 Beam Homogenizer with diffuser

To ensure flexibility the diffuser is placed between the two lenses of the beam expander as shown in Fig. 6.14. This allows a tuning of the homogeneity by changing the position e of the diffuser. The illuminated area of the diffuser will then vary with its position, while the average size of the microstructures remains the same.

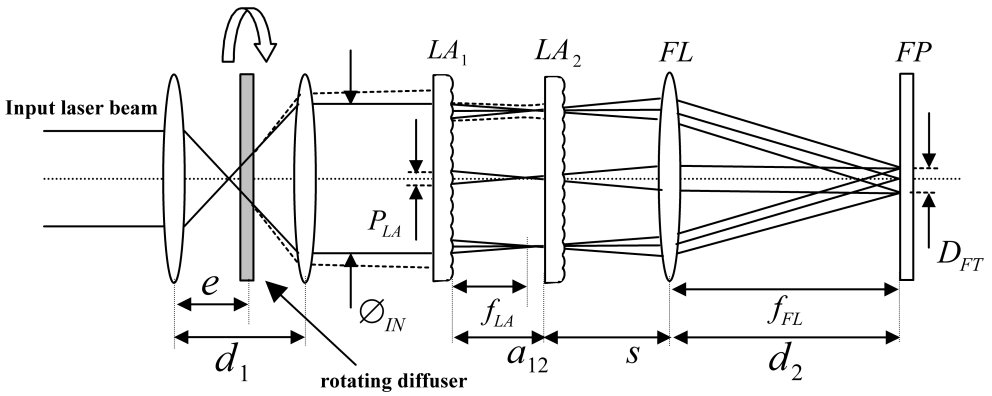

Figure 6.14: Scheme of beam homogenizer with telescope and diffuser. The diffuser is placed between the two lenses of the telescope spaced by d_1. By changing the position e of the diffuser modifications on the spatial intensity distribution in FP can be achieved. The position and the angular distribution of the diffuser have to be adapted to avoid crosstalks between microlenses on the second array LA_2 (dashed lines).

It implies that when looking at the system over a certain period of time, for instance the integration time of the CCD camera used to record the flat top intensity, the diffuser can be seen as a new incoherent source of diameter $\varnothing_{SD}$

$$\varnothing_{SD} = (e - d_1) \cdot \tan(\arcsin(NA)). \tag{6.19}$$

The distance e corresponds to space left between the two lenses of the telescope and d_1 to the position of the diffuser. NA is the numerical aperture of the telescope lenses. The radiance of the source will be modified by the diffusing properties of the diffuser as illustrated in Fig. 6.15. This interpretation has been confirmed in experiments when placing the diffuser directly at the focal point of the telescope and by displacing it closer to the last lens. One sees in Fig. 6.16 the increasing diameter of the spot of the diffraction pattern for two positions of the diffuser. It is easy to understand that the overall homogeneity that can be obtained by this way cannot be perfect since the square arrangement of the microlenses exclude a complete filling of the flat top area with a circular wide spreading of the local spots (due to the rotation of the diffuser). The variations of homogeneity H was calculated as the root mean square (RMS) value of the spatial intensity deviation from the mean intensity on the flat top area using

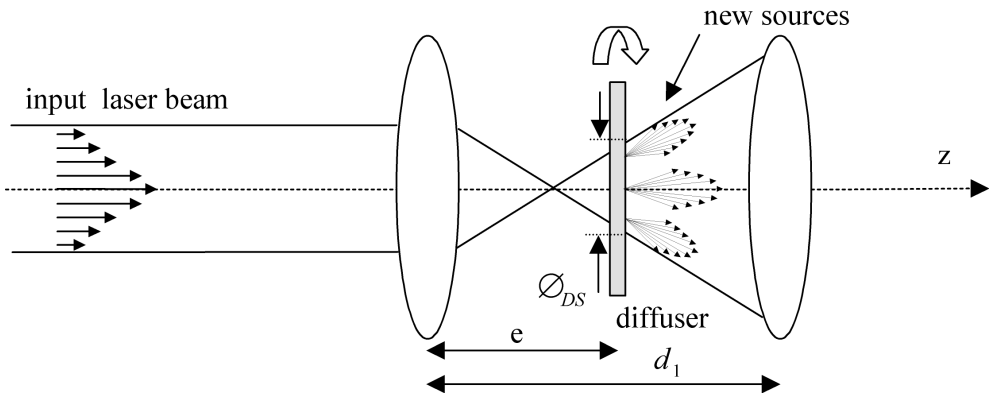

Figure 6.15: Interpretation of the influence of the diffuser as a "new source" of diameter $\varnothing_{DS}$. The diameter and the radiance of the "new source" is spatially modified by changing the position e of the diffuser inside the telescope.

$$H\ [\%] = \frac{\sigma}{\langle I(x,y)\rangle}, \tag{6.20}$$

where $\langle I(x,y)\rangle$is the spatial average value on the whole flat top area and σ is the RMS value of the intensity variation on the same surface and is defined by

$$\sigma = \sqrt{\left\langle I(x,y)^2 - \langle I(x,y)\rangle^2 \right\rangle}. \tag{6.21}$$

Commercial definition of the homogeneity follows ISO 13654 norm. While a spatial variation of homogeneity H of more than 100 % is observed for the raw intensity pattern in Fig. 6.17, the same value drops down to H=16 % using

a SMO HT 0.2° (HWHM) diffuser. Compared to a conventional ground glass diffuser the variation of homogeneity H is more than two times inferior for a collected power that is 2.8 times superior.

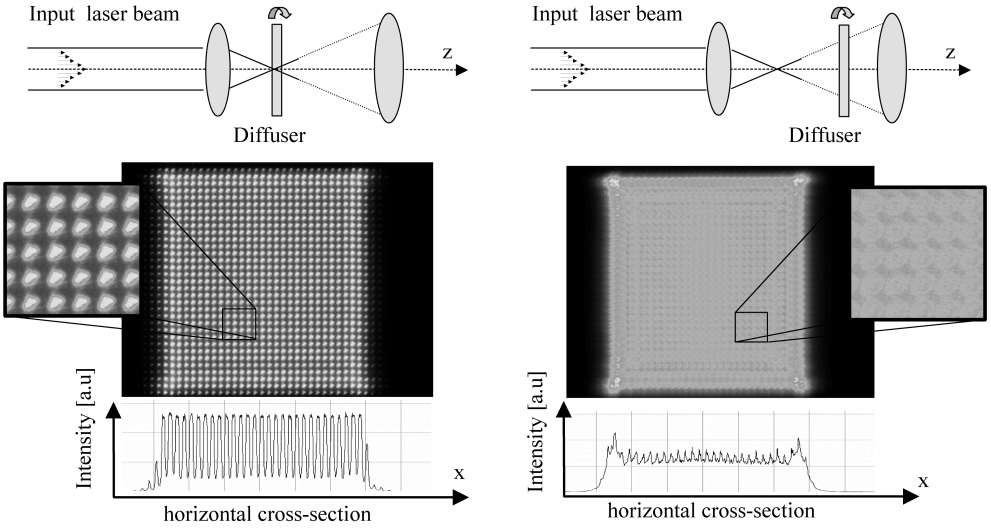

Figure 6.16: Experimental observation of the spatial intensity distribution in FP for two different positions of the rotating diffuser. A circular enlargement of the spots intensity is observed and a better homogeneity is achieved.

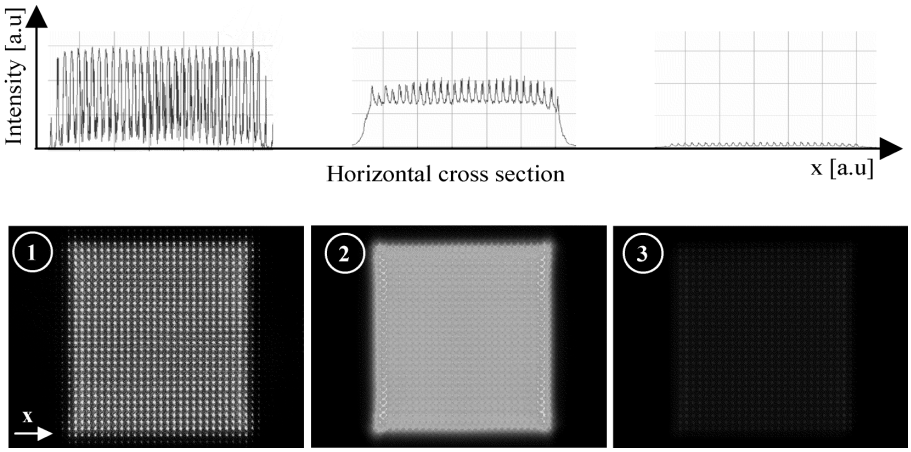

Figure 6.17: Intensity measurements in FP for a beam homogenizer with microlens arrays of 300 microns pitch and FN=37 at 670 nm. (1) Output intensity without diffuser. The spatial variation of the homogeneity H reaches more than 100%. (2) The addition of a rotating HT 0,2° diffuser reduced this variation H to 16 %, (3) The same experiment with a rotating ground glass diffuser (commercial product). The value H is around 33 % for 2.8 less collected power.

6.9 Advanced considerations on homogeneity

Placing a rotating diffuser in the telescope is not the only technique to increase the homogeneity. The defocus of the telescope is also another way to improve the homogeneity by changing the divergence of the light source. Defocus of the target plan compared to the Fourier lens is also a third possibility as we can see Fig. 6.18. It has to be noticed that microlens arrays are periodical elements and when illuminated with coherent fields they produce periodic patterns in the far field.

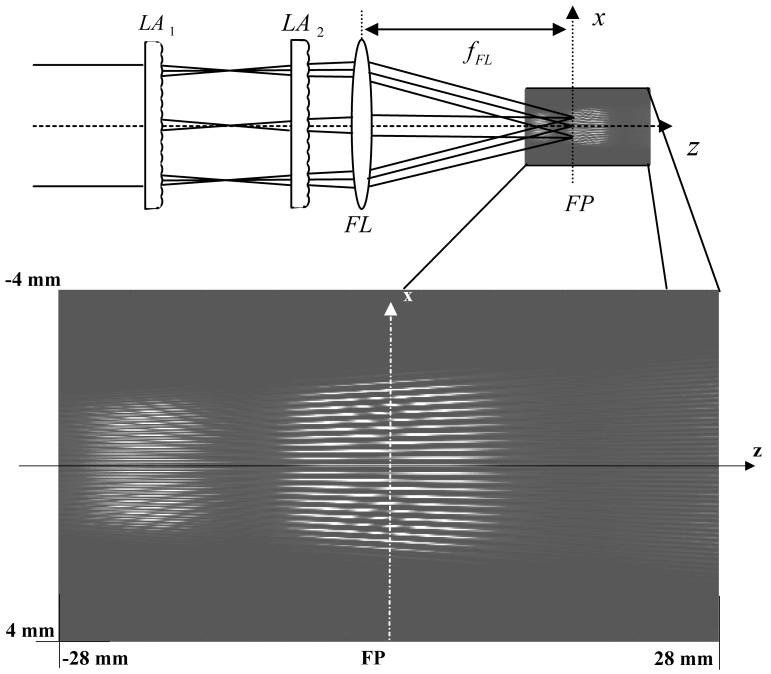

Figure 6.18: Simulation of the intensity distribution around FP for a beam homogenizer with microlens arrays of 300 microns pitch and FN=37 illuminated by a plane wave with Gaussian intensity distribution at 670 nm. The presence of spots are spatially localized. A defocus of the homogenization plan FP can help to increase the homogeneity.

This is definitely true for planes at defined distances known as Talbot planes [61, 62]. This Talbot planes are easily seen in Fig. 6.18. If the target plan is out of focus for example from the Fourier lens, the system is no more focused on a plan of periodical pattern and the overall homogeneity is increased. By combining the different ways of increasing the homogeneity, significant results have be recorded. As an example 5 % of variation of homogeneity H has been obtained with SUSS SMO HT 0.2° as shown in Fig. 6.19 .

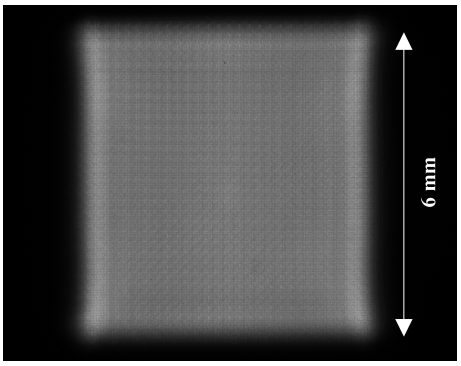

Figure 6.19: Picture of a flat top intensity distribution with only 5 % of variation of homogeneity H. This result has been obtained for a beam homogenizer with microlens arrays of 300 microns pitch and Fresnel Number FN = 37 illuminated at 670 nm through a rotating SMO HT 0.2° diffuser. The focal length of the Fourier lens FL = 80 mm.

6.10 Conclusions

Two types of diffusers dedicated to beam shaping applications with various diffusing properties have been realized and will be commercially available. It has been demonstrated that employed in conventional Fly'eye condenser they allow very high reduction of the overall contrasted pattern of coherent illumination. Using a laser diode at 670 nm and square microlens arrays we reduce the variations of homogeneity by a factor 2 compared to a conventional ground glass diffuser. Only 5 % of variations on the homogeneity has been measured. Moreover this type of diffusers with narrow angular dispersion allows high energy throughput. The measured collected power was almost 3 times superior compared to a conventional ground glass diffuser. The possibility to adapt the depth of the microstructures (i.e. their diffusing properties) ensure a high flexibility for various beam shaping applications.

Chapter 7

Concave microlenses

7.1 Introduction

In this chapter we described a new method allowing the creation of concave microlens arrays. While most of the fabrication methods to generate concave microlenses in photoresist are based on control of the exposure threshold or distribution [63, 64], we developed a two step photolithography process. We were able to fabricate concave microlens arrays with lens diameters between 30 to 230 μm and diffraction limited properties. For the development of the fabrication process, the simplicity of the method was a key point to respect. We tried to avoid additional etching or lift off steps.

Based on this fabrication principle, we fabricated diffusers by generating patterns of random locations and sizes of concave resist structures.

7.2 Basic principle

The fabrication principle consists in a two step process shown in Fig. 7.1. A photolithography step is done on a photoresist (PR) layer to create cylindrical holes. A melting step is performed on the obtained structures to harden them and allow continuous edge shapes formation. The melted structures are next filled by a second spinning step of resist. After a bake to remove the solvents, concave shapes are generated. Because of the complex geometry of the melted holes, several trials where performed to find the appropriated spin speeds and resist concentrations. We found that because of the non planar surface present during the second spinning step, the spin speed has to be slowed down to allow homogenous deposition of the PR. The spin speed is then no longer linked to the final thickness of the PR layer but rather to the quantity of PR filling the holes.

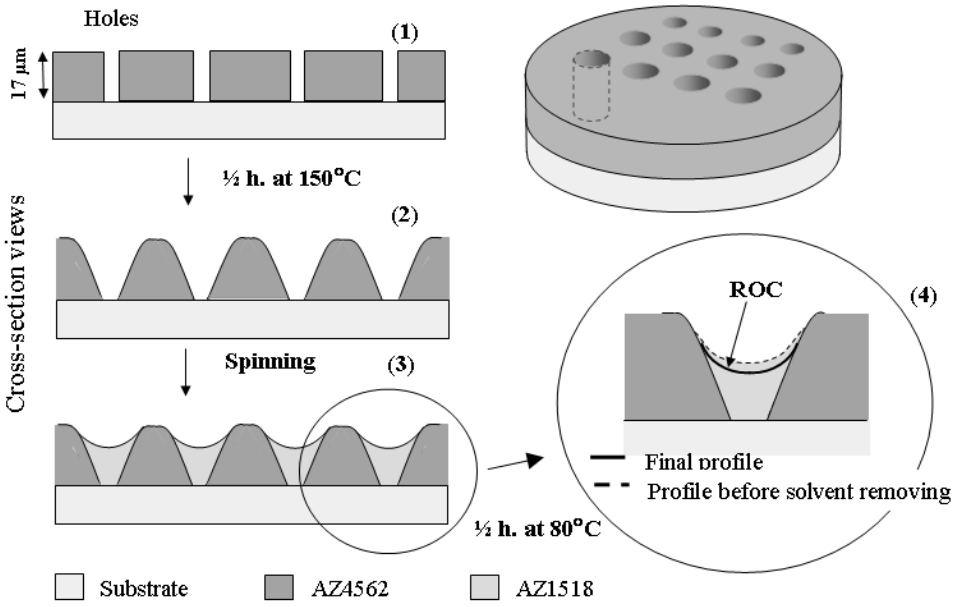

Figure 7.1: Process flow. The first step shows a crossed section view of cylindrical holes resulting from a conventional photolithography process (spinning of photoresist AZ4562, UV exposure through a mask with holes and development). During the second step the holes are melted at 150˚C for half an hour. In the third step the holes are filled with AZ1518 PR during a second spinning step. To finish the PR is dried in an oven at 80˚C for 30 minutes. The concave profile obtained by the surface tension is then modified by the solvent removed in the final cure.

7.3 Methodology

A mask containing hole arrays of various diameters has been designed. Hexagonal and square packed holes with diameters in a range between 30 to 240 μm spaced by 10 μm were designed. Three additional zones were filled with randomly generated pattern of various hole diameters in the purpose of testing the idea of concave microlens diffusers. The goal is to fill these holes, once transferred by photolithography, in a PR layer. As a starting point the thickness of this first layer on the glass wafers was fixed to 17 microns. To allow spinning of a second layer of PR it is necessary to melt the first layer of PR to make it less sensitive to the solvent dilution. This is performed half an hour in an oven at 150°C. The melting of the first layer is illustrated in Fig. 7.2 with two pictures of unmelted and melted holes. During melting some reflow of the PR from the thin regions between holes to wider zones occurs [65]. The main consequence is a lower wall ((A) in Fig. 7.2) between two holes meaning a lower depth of the melted holes . To avoid this drawback a less reflow sensitive PR (AZ4562) has

been used instead of the conventional thick PR AZ9260. Moreover to reduce this melting drawback, some empty spaces ((B) on Fig. 7.2) were added to the design of the mask to obtain the same width of the walls everywhere in the PR.

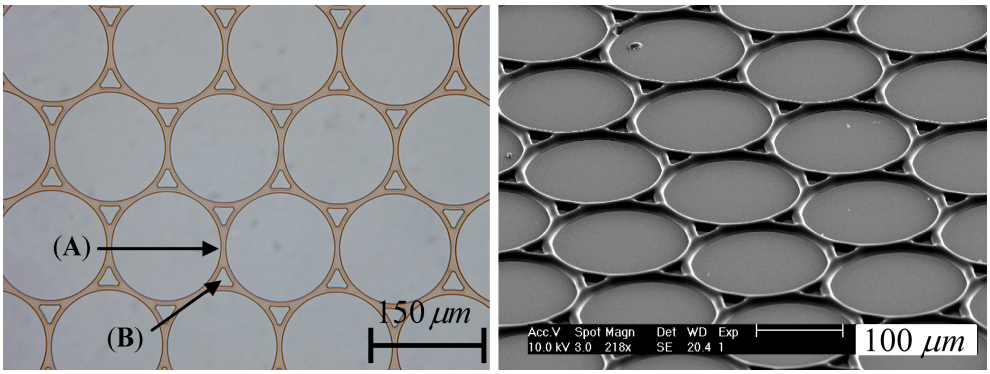

Figure 7.2: Microscope picture of unmelted (left) and SEM picture of melted (right) hexagonal packed cylindrical holes of diameter $\emptyset = 150\,\mu m$. The height of the walls (A) between holes depends on the reflow process. Empty spaces (B) have been added to the design to reduce the reflow and the local photoresist peak formation during the melting step.

This effect is shown in detail in Fig. 7.3 with two interference measurements showing the phase differences on the holes edges. Because of the too steep slopes of the walls no fringes were resolved.

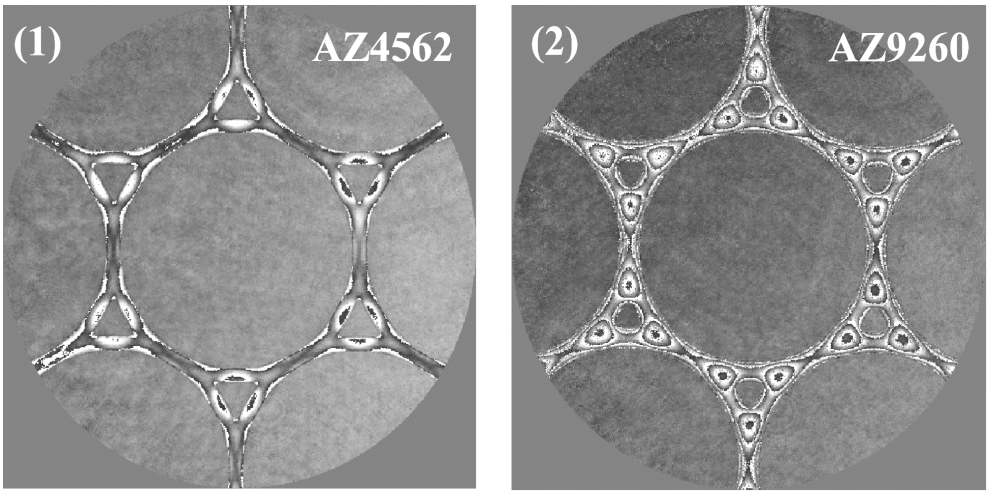

Figure 7.3: Illustration of the reflow occurring during the melting step of the first PR layer. Using a Mach-Zehnder interferometer two measurements (1) and (2) have been taken. They show interference fringes in the melted walls for two types of PR, AZ4562 and AZ9260. While in the first case only one fringe is seen from the lowest to the highest point on the walls more than 3 fringes are distinguished in the second case meaning deformations around 3 times more important.

Nevertheless variations on the wall profile are clearly distinguished. This effect is clearly minimized when employing AZ4562 PR instead of AZ9260 PR. In the first case only slight deformations of the walls appear visible as dark and light grey modulations. In the second case several black fringes are observable meaning stronger deformations. The amplitudes of these deformations depend on the array geometry. As an example, height differences between the lowest and the highest part of the wall in Fig. 7.3 were $3.8\,\mu m$ in the AZ9260 and 3 times less around $1.3\,\mu m$ for the AZ4562.

The holes are then filled by a second step of spinning. To avoid inhomogeneous deposition of the second layer, some PR is poured on all the wafer before spinning occurs. Because of the presence of structures before spinning, the spin speed is not anymore correlated to the final layer thickness as mentioned in chapter 1. In this case it seems correlated to the amount of PR left in the filled holes. After filling, the wafers are dried in an oven at 80°C for 30 minutes to remove solvents. At this stage concave shapes are obtained depending on the boundary conditions imposed by the melted hole, the surface tension of the chosen PR and the amount of solvent removed during the drying step.

7.4 Quality measurements

To get values on their quality, all the microlenses where measured using a Mach-Zehnder interferometer [66, 67, 68] allowing the calculation of the corresponding Strehl ratio. The Strehl ratio or normalized intensity $i(P)$ is defined as

$$i(P) = \frac{I(P)}{I^*}, \tag{7.1}$$

where $I(P)$ corresponds to the intensity in the point P (focal point) and $I^*$to the intensity which would be obtained without aberrations[69]. The Marechal's criterion applies that Strehl ratio higher than 80 % are considered for diffraction limited microlenses [70]. More in detail, the validity of the approach comes from the fact that, as a first approximation, the half-width of the diffraction Airy pattern introduced by the circular lens aperture in the focal region does not change with the presence of small aberrations. But energy from the central lobe is redistributed in the different side lobes. So the calculation of the ratio between the amount of energy in the central lobe without aberrations and with aberrations becomes a way to get an idea on the quality of the microlens. When the aberrations are sufficiently small, the Strehl ratio is expressed by the following equation:

$$i\left(P\right) \sim 1 - \frac{4 \cdot \pi^2}{\lambda^2} \cdot \left[\frac{\iint \left\{W(x,y)\right\}^2 dxdy}{A} - \left\{ \frac{\iint \left\{W(x,y)\right\} dxdy}{A} \right\}^2 \right], \quad (7.2)$$

where $W(x,y)$ corresponds to the wavefront aberration, A the surface of the exit pupil of the optical system. The term in brackets can be recognized as the variance of $W(x,y)$. So the Strehl tolerance level (0.8) is reached when the variance is $\frac{\lambda}{197}^2$ or when the RMS deformations of the wavefront is about $\frac{\lambda}{14}$. To get an idea on the maximal allowed deformation of the wavefront we consider the case of primary spherical abberation that can be written in polar coordinates (ρ, ϕ), $W\left(\rho,\phi\right) = \alpha_1 \cdot \rho^4$. One finds from Eq.7.1 that the maximum deviation of the wavefront $\alpha_1 = \pm 0.24 \cdot \lambda$. This correspond to the Rayleigh quarter-wavelength rule which says that the optical system is substantially perfect if wavefronts can be included between two concentric spherical surfaces $\frac{\lambda}{4}$ apart. As an example if we take a concave microlens in photoresist with a diameter of $\emptyset$=50 μm with a depth $h = 5.05\,\mu m$ (NA of 0.2). The corresponding optical path length, for a refraction index difference of $\Delta n \sim 0.5$, is equal to 4λ. The maximum acceptable deformation stands to $\frac{0.25 \cdot \lambda}{4 \cdot \lambda} = \frac{1}{16}$. The fabrication error should be less than 6.2 % for this microlens depth. More details on quantification of wavefront aberrations can be found in reference [69].

7.5 Experimental results

The maximum diameters of the diffraction limited concave microlenses that have been realized as a function of the spin speed of the second layer of PR are shown in Fig. 7.4. It is seen that diffraction limited concave microlens arrays could be produced for diameters in a range between 30 to 230 μm. The minimum achievable diameter was arbitrary defined when only one fringe (i.e. depth around 1.2 μm) could be solved or because of inhomogeneity coming from the too important filling of the holes. For diameters over 150 μm the holes are almost filled, resulting in an nearly flat profile. The numerical aperture (NA) is then lower than 0.02. A degree of freedom on the numerical aperture is possible by changing the spin speed and/or the dilution of the PR as seen in Fig. 7.5 and Fig. 7.6. As an example square packed concave microlens arrays of pitch between 70 to 80 μm with a gap of 10 μm having NA from 0.07 to 0.14 have been realized (grey zone in Fig. 7.6). The differences observed in the results presented in Fig. 7.4, Fig. 7.5 and Fig. 7.6 between square and hexagonal packed microlens arrays could come from boundary conditions imposed by the

geometry of the melted holes and from the thin layer of PR deposits at the surface which quickly dries because of the volatile solvents contained inside it.

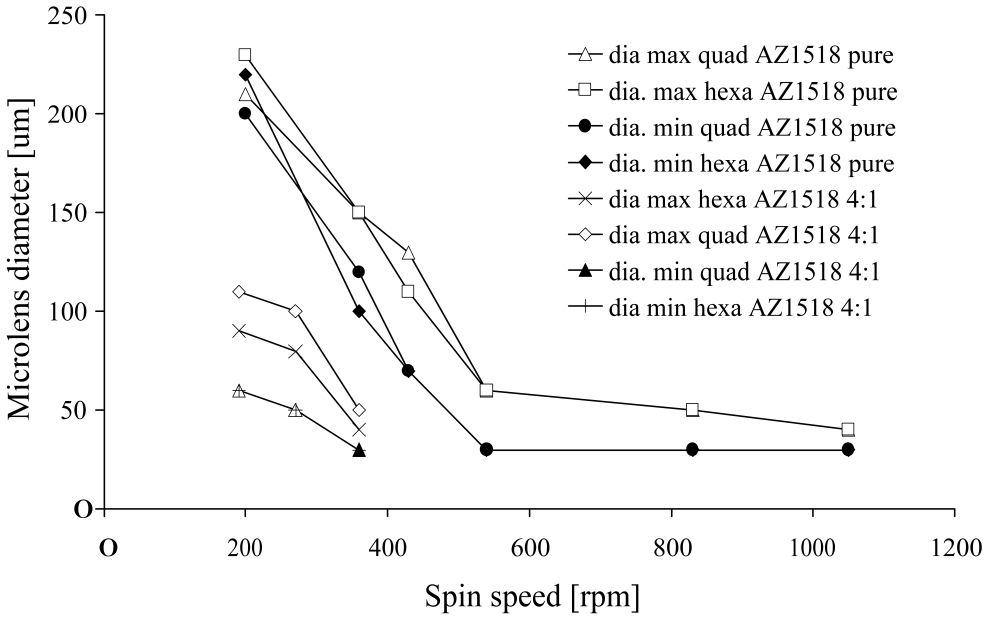

Figure 7.4: Results of the fabrication of concave microlens arrays. The curves show the maximum diameters of diffraction limited microlenses that could be obtained when varying the spin speed of the second layer of AZ1518. Over this limit, the Strehl ratio of the concave microlenses drops down to values lower than 80%. The minimum diameters were arbitrary defined when only one fringe could be solved on the interference measurements or when homogeneity problems happened. Square (quad) and hexagonal (hexa) packed arrays have been considered.

The influence on the resulting meniscus shape of these boundary conditions is shown in Fig. 7.7. The figure shows RMS deformations from a sphere occurring for increasing diameters after deposition of the second layer (AZ1518 4:1 270 rounds per minute (rpm)). For diameters lower than $80\,\mu m$ no significant deformations are visible (Strehl ratio $\sim$96 %). For diameters between $80\,\mu m$ and $100\,\mu m$ deformations are clearly visible as well as their different locations for hexagonal and square packed arrays. In this experiment square packed microlens arrays are less sensitive. For diameters $\varnothing > 100\,\mu m$ the holes are not enough filled and after drying both (square and hexagonal packed) microlenses exhibit similar deformations. Fig. 7.8 shows the profile formation of the concave shape in measurements performed on a constant microlens diameter $\varnothing = 50\,\mu m$ and for different spin speed experiments. Because of the non vertical walls surrounding the meniscus, the radius of curvature (ROC) of the realized microlenses changes depending on the filling rate of the melted holes. An important question is the homogeneity of the obtained results. For spin speeds higher

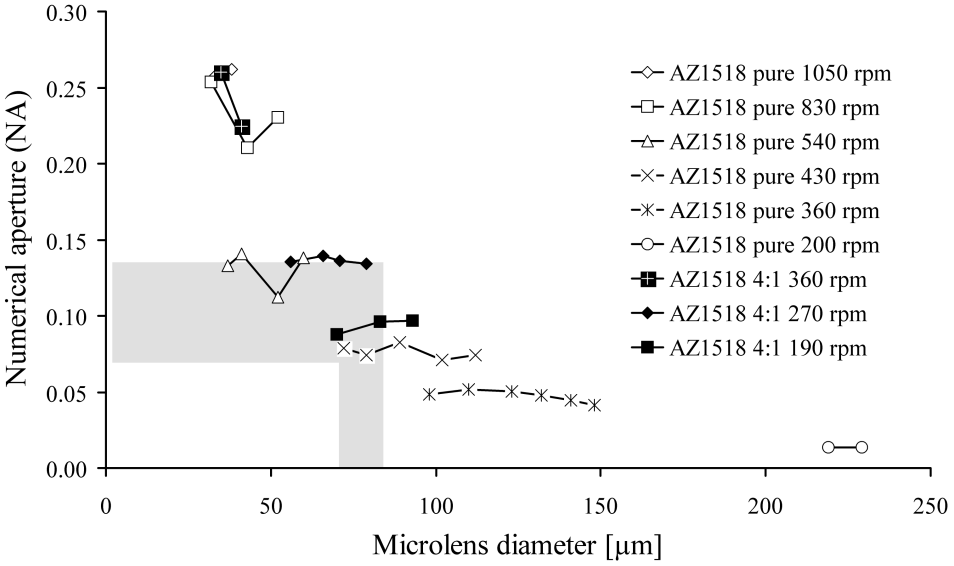

Figure 7.5: Numerical aperture (NA) as function of the microlens diameters (hexagonal packed arrangement) for various spin speed experiments. As an example, in the grey zone corresponding to microlenses with diameters between 70 to 80 microns, NA between 0.07 to 0.14 have been realized by changing the spin speed and/or the dilution of the PR.

than 2000 rpm some shadow effects of the structures, mainly coming from the grid between the microlens arrays, are observable.

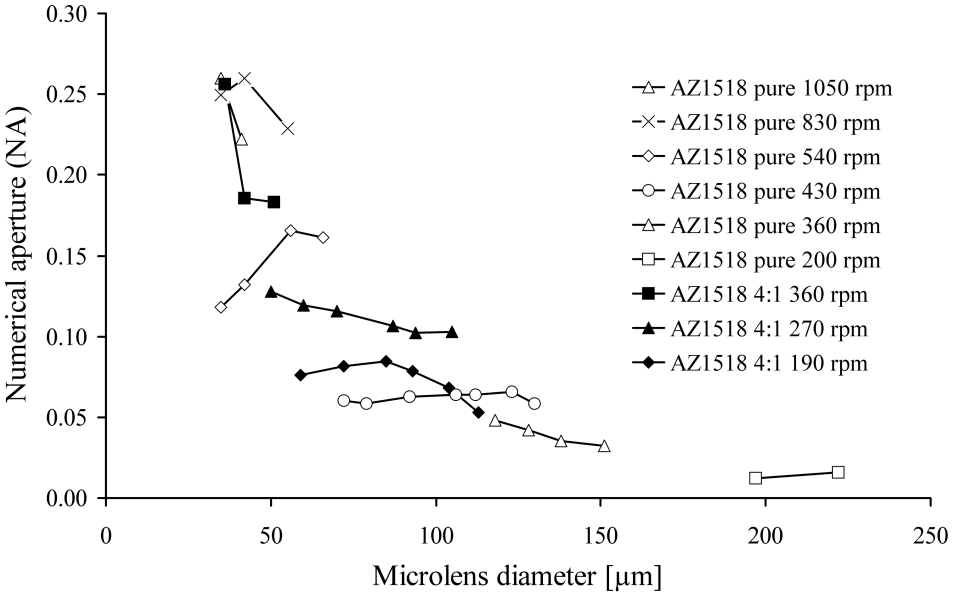

Figure 7.6: Numerical aperture (NA) function of the microlens diameters (square packed arrangement) for various spin speed experiments.

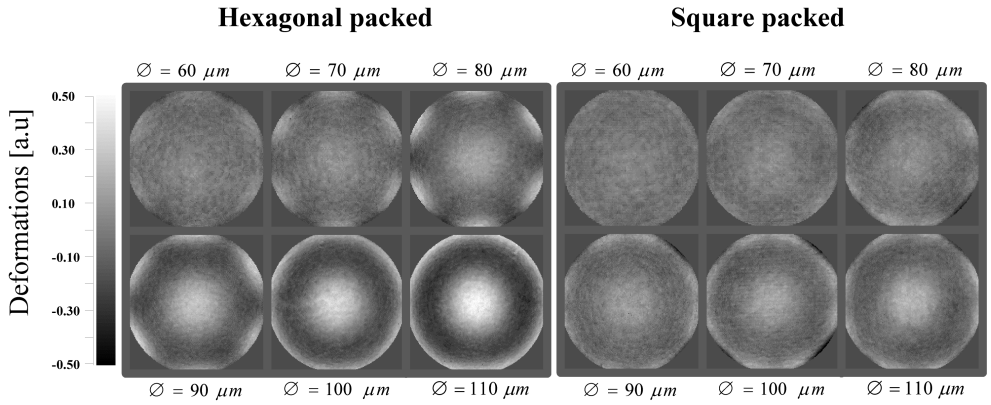

Figure 7.7: 2D profile deformations from a sphere for increasing microlens diameters between 60 to 110 microns. The arrangement of the array is clearly seen in the deformations which occur at the four cardinals points for square packed array and at both sides of the three axis of symmetry for hexagonal packed microlens arrays. The first layer is $17\,\mu m$ *of AZ4562 and the second layer of diluted (4:1) AZ1518 was spincoated at 360 rpm*

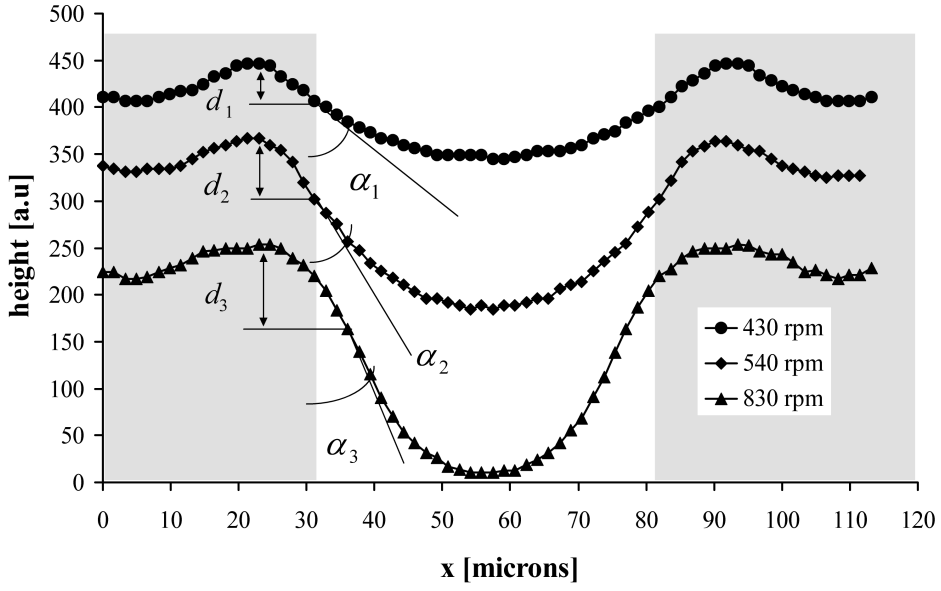

Figure 7.8: Profile measurements of concave microlenses with $\emptyset = 50\,\mu m$ *(white area) obtained at 3 different spin speeds of pure AZ1518. The vertical positions are set arbitrary. The anchoring point (i.e., the inflection point of the profile of the microlens) of the meniscus will depend on the filling of the holes. As it can be seen, the distances* (d_1, d_2 , d_3) *between the top part of the profile and the starting slope (angle* α_1, α_2, α_3) *of the meniscus decrease. At 830 rpm the meniscus starts within the hole and deformations appears on the edges as shown previously in Fig. 7.7.*

For lower spin speeds the results are quite homogenous even if the tested wafers contained various structures in heights and sizes. For this reason no investigations have been done to evaluate all parameters. Nevertheless it is possible, as shown in Fig. 7.9, to realized homogenous arrays of several microlenses. The typical defects encountered during the fabrication process are illustrated in Fig. 7.10.

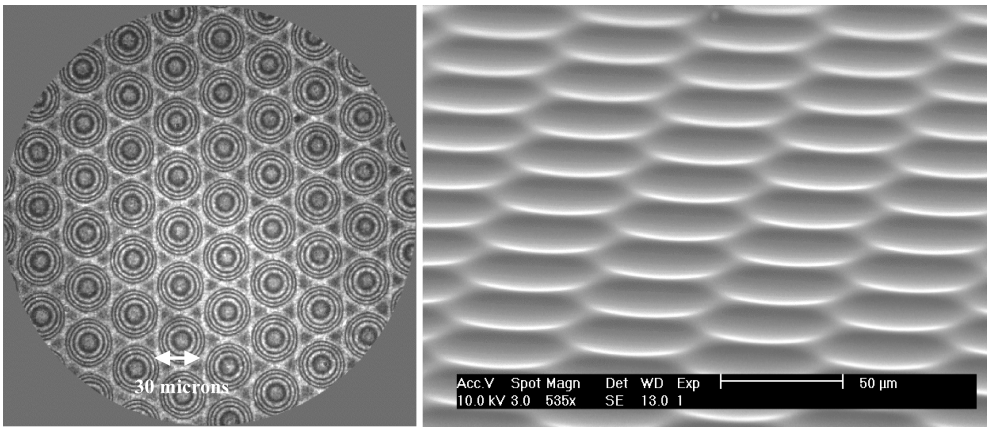

Figure 7.9: Large scale interference picture (left) and SEM picture (right) of respectively 40 µm pitch and 60 µm pitch concave microlens array showing the homogeneity of the realized samples.

It consists in trapped air bubbles, dust particles, cracks in the second layer as well as local adhesion problems of the first layers.

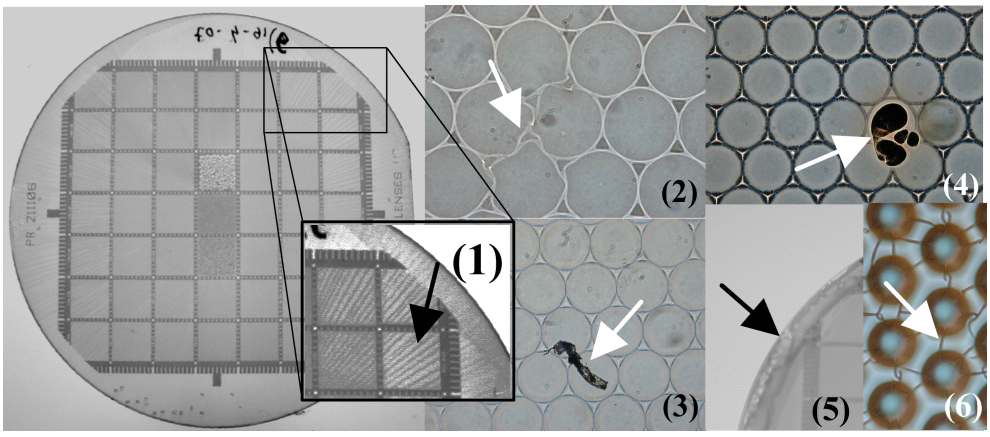

Figure 7.10: Pictures of typical defects encounter during the fabrication process. (1) Shadow effect of the structures during spinning of the second layer of PR for spin speed higher than 2000 rpm.(2) Local deformation due to local weak adhesion of the first layer. (3) Dust particles. (4) Trapped bubbles. (5) Edge beads formation of PR at very low spin speed of the second layer (< 400 rpm).(6) Cracks in the second spun layer.

At very low spin speeds it is necessary to remove the PR at the edge of the wafer during spinning to ensure homogenous distribution of the second layer. The reproducibility of the experiment is closely linked to the quality of the photolithography of the first layer. Once the thickness, the quality of the exposure and the quality of the development of the photoresist is kept constant, variations of less than 10 % were observed on the focal length of the diffraction limited microlenses. The temperature as well as the dilution rate of the photoresist used to fill the holes are also important parameters which have to be well quantified.

7.6 Concave microlens diffusers

Based on experiments with the SMO HT diffusers that are composed of concave structures, three types of design have been developed. They consist in randomly distributed (in positions and sizes) holes over an area of 1 square cm. The

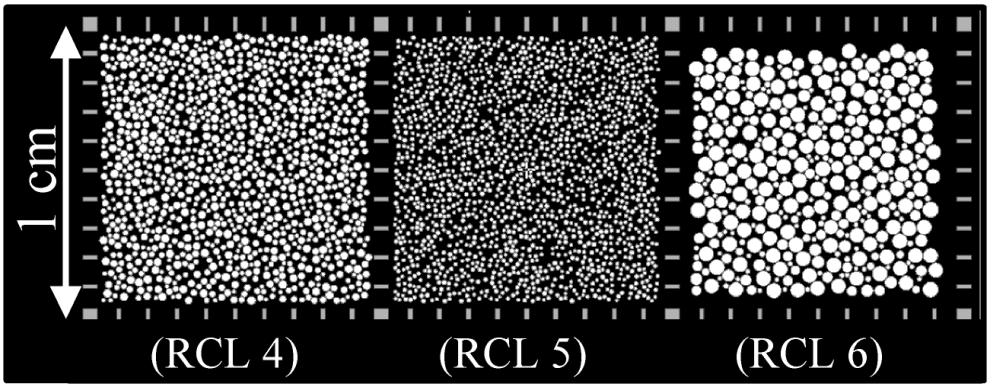

Figure 7.11: Illustration of the three patterns of randomly distributed holes. The diameters of the holes were contained in ranges between 100 to $300\,\mu m$ *(RCL 4), 70 to* $160\,\mu m$ *(RCL 5) and to 160 to* $500\,\mu m$ *(RCL 6) .*

designs are illustrated in Fig. 7.11. On the left part of the figure, the range of diameters was contained between 100 to $300\,\mu m$ (RCL 4) while in the design on the middle, they were restricted to 70 to $160\,\mu m$ (RCL 5) and to 160 to $500\,\mu m$ (RCL 6) in the last pattern. Using a Mach-Zehnder interferometer, the profile of three realized diffusers are shown in Fig. 7.12. The typical depth of the resulting structures lies at 15 microns. To avoid a strong zero order transmission of the diffusers the main part of the holes must be filled and form concave shapes. Because of the large hole diameters (designed to ensure low diffusing angles), only very low spin speed fulfill this condition. For this reason only diffusers from spin speed experiments allowing formation of concave microlenses close to the specific range of hole diameters have been considered.

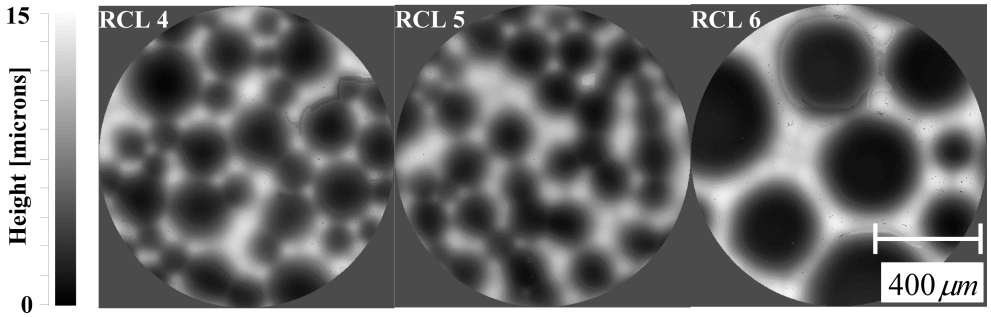

Figure 7.12: 2D profiles of three realized diffusers. Because of the reflow occurring during the melting step of the first layer the zones between concave microlenses are no more flat (white and grey areas) and strongly reduced zero order transmission. The first layer is set to 17 microns and the second layer of pure AZ1518 has been spincoated at 200 rpm.

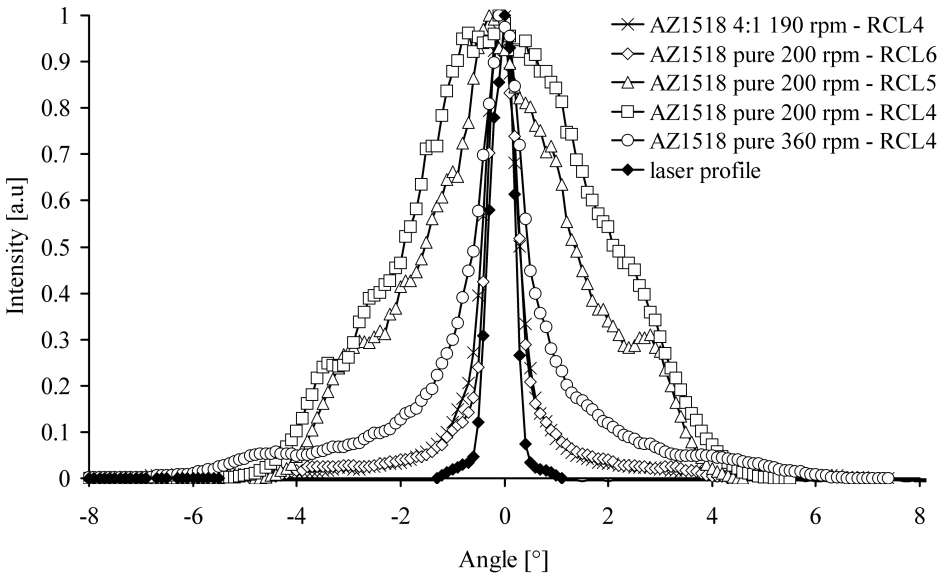

Figure 7.13: Measured angular distribution curves of concave microlens diffusers. AZ1518 pure 200 rpm RCL 4 and RCL5 show very nice smooth dispersion while no zero order transmission is observable.

Their diffusing properties have been analyzed using the goniometric setup illustrated in chapter 6 and shown in Fig. 7.13. While most of the measured diffusers only scatter around 10% of the light intensity with a strong zero order transmission, two diffusers (AZ1518 pure 200 rpm RCL 4 and RCL5) show a smooth distribution of the transmitted light. The large cut-off angle around 4° could be reduced by a dry etching step with adapted selectivity.

7.7 Conclusion

A new method allowing the fabrication of diffraction limited concave microlens arrays has been demonstrated. Moreover by adjusting the processing parameters of the PR a control on the numerical aperture NA is possible. Once fabricated and transferred in a fused silica wafer to ensure flat areas between microlenses, they could be used as a mold for fabrication of high quality convex microlenses. Moreover because of the unexposed second layer of PR, nanostructures could be written at the surface using interference recording.

The fabrication process of concave microlenses has been successfully applied to the realization of diffusers. The idea behind is the increase of the flexibility on the design of fused silica diffusers compare to conventional statistical methods such as sandblasting techniques or wet chemical etching. Using dry etching on fused silica wafers several diffusers with interesting diffusing properties could be realized. Some trials with others PR with different surface tension would be a way to explore the flexibility of this fabrication method. It would probably permit to increase the range of possible NA.

Chapter 8

Conclusion

This thesis illustrates various applications of microlenses. From several birefringent ones built in arrays and combined with an index matching layer a micro-optical polarizer has been realized in chapter 3. Its efficiency has been simulated and measured on fabricated samples. The possibility to shape birefringent materials allows formation of micro-optical elements that can be combined to form systems. This micro-optical polarizer is an example of such systems and the measured efficiency over 72 % gives validity to this approach. Various applications of microlens arrays are possible. For design applications some moiré magnifiers with high image quality have been realized in chapter 4. Because of their small diameters the Fresnel number of the microlenses can easily reach very low values FN$<$10 and diffraction effects begins to be preponderant. A study of their implications on the maximum focal length that can be obtained for microlenses has been done in chapter 5. As well as the possibility to choose a design that allows the same position of the peak irradiance at two different wavelengths. Comparison between results obtained in the FRED optical software and the Rayleigh-Sommerfeld equations has been performed. With the recent opportunity to easily obtain microlens arrays of very high quality, several applications in beam shaping application are found. The typical case of fly'eyes condensers is developed in chapter 6. This microlens beam shapers are well adapted to uncoherent light emitters such as LEDs. But when used with highly coherent sources they produced very contrasted patterns. A solution consists to add a rotating diffuser in the optical path after the light source and before the beam shaper. To ensure a high energy throughput compare to commercial ground glass diffusers, several designs of low angular distribution down to 0.2° (FWHM) diffusers have been realized. Basic rules to use them are given. A deacrese of the spatial variations of the homogeneity down to only 5 % has been measured. Compared to a ground glass diffuser they reduce the inhomogeneity by a factor 2 while they allow a power collection 2.8 times higher. In

chapter 7, a new method to fabricate concave microlens arrays with diffraction limited features is described for diameters between 30 to 230 μm. An application is shown through the realization of diffusers from statistical distribution in size and location of concave shapes. Goniometric measurements show no zero order transmission.

Acknowledgements

I would like to thank in my french English:

Prof. Dr. René Dändliker, who hired me at IMT.

Prof. Dr. Hans-Peter Herzig, my thesis director, for his valuable remarks during the correction of my thesis manuscript.

Dr. Toralf Scharf, my supervisor who allowed me to stay longer than I thought and fully helped me to realize this thesis.

Dr. Reinhard Völkel, who was my expert, gave me so much work to do for yesterday and introduced me to the field of beam shaping and diffusers.

Prof. Dr. Hans Zappe, from the University of Freiburg (D), for accepting to read my thesis and be my expert.

The University of Neuchatel and the "Commission pour la Technologie et l'Innovation" (CTI), for financially supporting my research.

All the industrial partners involved in the different projects and especially the company SUSS MicroOptics.

Dr. Gerben Boer, my ancient high school colleague, who thought of me when he was looking for someone to make Wollaston cells in liquid crystal polymers and introduced me to the world of birefringent micro- optics and spectrometers.

Dr. Olivier Ripoll, with whom I shared my office and who introduced me to diffraction and to (the) incomprehensible philosophical implications of quantum mechanics.

Irène Philipoussis, who did not only share my office but also life difficulties and joys with always in the silent background a strange salsa song from some obscure South American guy. She helped me a lot in the fabrication of concave microlenses.

Dr. Iwan Märki, who helped me to stay fit by joining me at the swimming pool and for the numerous interesting scientific discussions we had on photonic crystals.

Dr. Sylvain Jaquet, who also helped me to stay fit by joining me at the swimming pool and encouraged me to swim the head under water level (not ideal for breathing) and also for the numerous interesting scientific discussions on OLED and Bragg reflectors we had.

Sylvain Herminjard, for his perpetual good mood and his so personal style.

Vincent Paeder, an inhabitant of Le Landeron (thus, a nice guy ;)) who also came swimming, for his interesting explanations about optical theory, methods, validity, matrices, and so on.

Pierre-Yves Baroni, a colleague biker and companion in the clean room who recorded many gratings for me.

Dr. Oliver Scherler, a true biker (all weathers) with delicious coffee in his office.

Dr. Wataru Nakagawa, for his delicious chocolate and his phosphorescent American junk food.

Dr. Piero Tortora, for his sympathetic birthdays with guitar concerts, the soccer matches we played together and for his SNOM introduction.

Dr. Emiliano Descrovi, for our nice talks on polarization distributions and for his dog that sometimes scared me in the hallway late in the evening.

Marcel Groccia and Martial Racine, for the few bike tours I tried to do with them, sweating and praying that they would suffer from their old ages. No way...

Felix Schädelin, for his help in the preparation of the exercises for students.

Dr. Kenneth Weible and Dr. Pascal Pernet, for their valuable advice on making the RIE machine work.

All the SUSS MicroOptics team.

Mary-Claude Gauteaub and Joëlle Banjac, for helping me with parcels.

Sandrine Piffaretti, for helping me with incredibly complicated administrative tasks.

Mme Stocker and Mme De Carvalho, for helping me avoid financial disasters at IMT.

Dr. Christophe Weiteneder, for his introduction to the field of holography.

Dr. Christian Bohley, for his artistic views on the scientific work.

Dr. Carsten Rockstuhl, for helping me using the FMM in Matlab.

Dr. Guido Niederer, for introducing me to the behavior of gratings.

Dr. Martin Salt, who introduced me to the English humor.

Dr. Omar Manzardo, for his precious advice on lifestyle.

Reto Tscharner, for his help with the fire security system and about all things that create vacuum, especially pumps.

Cédric Bucher, for his help with finding Reto.

Dr. Andrea Crottini, Dr. Lorenzo Sirigu, Hicham Farah, Roland Bitterli, Tristan Sfez, Dr. Luciana Vaccaro, Dr. Marcella Giovannini, Jean-Luc Coulot.

Jean Luc Kumin, for teaching me how to repair a motorbike and how it was when you rode a famous Triumph Bonneville.

Patrick Hostettler, for his sympathetic mood and for all the various discussions we had.

All the people from the other groups at IMT, who shared coffee the morning, lunch or some cigarettes that I may have smoked during my time here.

My clos friends, with whom I can share other aspects of my personality and who helped me find a good balance between work and leisure...

My family, my father, my mother and my two brothers, who were and are so important to me.

My wife Perrine for all... and more...

My son Esteban, whose interest in grabbing things and understanding the world surrounding him always captivated me and made me remeber the fundamentals of science...

Bibliography

[1] *Micro-optics Elements, systems and applications*, edited by H.P. Herzig, Taylor and Francis (1997)

[2] T. Stone and N. George, *Hybrid diffractive-refractive lenses and achromats*, Appl. Opt. **27**, 2960- (1988)

[3] P. Ruffieux, T. Scharf, H. P. Herzig, R. Völkel, and K. J. Weible, *On the chromatic aberration of microlenses,* Opt. Express **14**, 4687-4694 (2006)

[4] V.Paeder, T. Scharf, P. Ruffieux, H.P. Herzig, R. Voelkel, K.J. Weible, *Microlenses with amplitude and phase masks*, JEOS, Vol 2, pp. 07005-1-07005-6 (2007)

[5] G. J. Swanson, W. B. Veldkamp, *Diffractive optical elements for use in infrared systems*, Opt. Eng. **28**, 605-608 (1989)

[6] H. P. Herzig, M. T. Gale, H.W. Lehmann, R. Morf, Diffractive components: Computed generated elements. In Ph. Lalanne, P. Chavel (eds) Perspectives for Parallel Interconnects, pp 71-107, Berlin, Springer (1993)

[7] A.M. Donald, A.H. Windle, *Liquid Crystalline Polymers*, Cambridge University press (1992)

[8] G. Boer, P. Ruffieux, T. Scharf, P. Seitz, R. Dändliker, *Compact Liquid-Crystal-Polymer Fourier-Transform Spectrometer,* Appl. Opt. **43**, 2201-2208 (2004)

[9] L. Novotny, B. Hecht, *Principles of Nano-Optics* ,Cambridge Univ. Press, Cambridge, UK *(*2006)

[10] C.Koch, T.J. Rinke, *Lithography, theory and application of photoresists, developers, solvents and etchants*, Ed. Microchemicals (2006)

[11] Z. D. Popovic, R. A. Sprague, G. A. Neville-Connell, *Technique for monolithic fabrication of microlens arrays*, Appl. Opt. **27**, 1281- (1988)

[12] D. Daly, R. F. Stevens, M. C. Hutley, and N. Davies, *The manufacture of microlenses by melting photoresist*, J. Meas. Sci. Technol. **1**, 759-766 (1990).

[13] P.Nussbaum, R. Volkel, H.P. Herzig, M. Eisner, S Haselbeck, *Design, fabrication and testing of microlens arrays for sensors and microsystems*, Pure Appl. Opt. **6**, 617-636 (1997)

[14] Y. Xia,G. M. Whitesides, *Soft lithography*, Annu. Rev. Matter. Sci. **28**, 153-84 (1998)

[15] M. Heckele, W. K. Schomburg, *Review on micro molding of thermoplastic polymers*, J. Micromech. Microeng. **14**, R1-R14 (2004)

[16] S.Y. Chou, P.R. Krauss, P J. Renstrom, *Nanoimprint lithography*, J.Vac. Sci. Technol. B 14 (6), 4129-4133 (1996)

[17] J.P. Rolland, E. C. Hagberg, G M. Denison, K. R. Carter, J. M. De Simone, *High-Resolution Soft lithography: Enabling Materials for Nanotechnologies*, Angew. Chem. Int. Ed. **43**, 5796-5799 (2004)

[18] S. W. Lee, S.S. Lee, *Shrinkage ratio of PDMS and its alignment method for the wafer level process*, Microsyst Technol **14**, 205-208 (2008)

[19] I*nformation about high technology silicone material,* Sylgard 184 datasheet, Dow Corning corporation (1991)

[20] G. S. Oehrlein, J. F. Rembetski, *Plasma-based dry etching techniques in the silicon integrated circuit technology*, IBM J. Res. Develop. Vol 36 No. 2 (1992)

[21] C. Chang, Y. F. Wang, Y. Kanamori, J. J. Shih, Y. Kawai, C. K. Lee, K. C. Wu, M. Esashi, *Etching submicrometer trenches by using the bosch process and its application to the fabrication of antireflection structures*, J. Micromech. Microeng. **15**, 580-585 (2005)

[22] LA Donohue and al., *Developments in Si and SiO2 Etching for MEMS-Based Optical Applications, proceeding of SPIE,* Vol. 5347, pp 44-53 (2003)

[23] F. Gaboriau, G. Cartry, M-C. Peignon, Ch.Cardinaud, *Etching mechanisms of Si and SiO_2in fluorocarbon ICP plasmas: analysis of the plasma by mass spectrometry, Langnuir probe and optical emission spectroscopy*, J. Phys. D:Appl. Phys. **39**, 1830-1845 (2006)

[24] M. Madou, *Fundamentals of microfabrication*, CRC press (1997)

[25] S.A. McAuley, H. Ashraf, L. Atabo, A. Chambers, S. Hall, J. Hopkins, *Silicon micromachining using a high-density plasma source*, J. Phys. D:Appl. Phys. **34,** 2769-2774 (2001)

[26] J.M. Teijido, *Conception and design of illumination light pipes*, Thesis at the university of Neuchatel (2000)

[27] T. Scharf, *Polarized Light in Liquid Crystals and Polymers*, Wiley & Sons, (2006)

[28] S. Huard, *Polarisation de la lumière*, Masson (1994)

[29] C. Gu, P. Yeh, *Optics of Liquid Crystal Displays,* Wiley, New York, (1999)

[30] 4. D.J. Broer, *Reation of Supramolecular thin film architectures with liquid-crystalline networks*, Mol Cryst Liq Cryst **261**, 513-523 (1995)

[31] N. Nieuborg, A. Kirk, B. Morlion, H. Thienpont, I. Veretennicoff, *Polarization-selective diffractive optical elements with an index-matching gap material*, Appl. Optics. **36**, 4681-4685 (1997)

[32] W. C. Yip, H. C. Huang, H. S. Kwok, *Efficient polarization converter for projection displays*, Appl. Optics. **36**, 6453-6457 (1997)

[33] C.W. McLaughlin, *Progress in projection and large-area displays*, Proc. IEEE, Vol: 90, no. 4, (2002).

[34] T. Scharf, *Static birefringent microlenses*, Optics and Lasers in Engineering **43**, 317-327 (2005)

[35] G. Boer, Toralf Scharf, *Polarization Ray Tracing in Twisted Liquid Crystal Systems*, Mol. Cryst Liq.Cryst., Vol. 375, pp. 301-311 (2002)

[36] M. C. Hutley, *Interference (holographic) diffraction gratings*, Jounal of Physics E, Vol 9 (1976)

[37] E. G. Loewen, E. Popov, *Diffraction gratings and applications*, Marcel Dekker Inc, New York (1997)

[38] H. Kamal, R. Völkel, J. Alda, *Properties of moiré magnifiers*, Opt. Eng. **37** (11) 3007-3014 (1998)

[39] I. Amidror, *The Theory of the Moiré Phenomenon,* Kluwer Academic Publishers, Dordrecht (2000)

[40] C. A. Walker, *A historical review of moiré interferometry*, Exp. Mech. **34**, 281-99 (1994)

[41] Y. Yamamoto, Y. Morimoto, M. Fujigaki, *Two-directional phase-shifting moiré interferometry and its application to thermal deformation measurement of an electronic device*, Meas. Sci. Technol. **18**, 561-566 (2007)

[42] I. Amidror, *A new print-based security strategy for the protection of valuable documents and products using moiré intensity profiles*, Proceedings of SPIE Vol. 4677 (2002)

[43] C.Hembd-Sölner, R.F. Stevens, M.C. Hutley, *Imaging properties of the Gabor superlens*, J. Opt. A: Pure Appl. Opt. **1**, 94-102 (1999)

[44] R. H. Anderson, *Close-up imaging of documents and displays with lens arrays,* Appl. Opt. **18**, 477-84 (1979)

[45] M.C. Hutley, R. Hunt, R.F. Stevens, P. Savandert, *The moiré magnifer*, Pure Appl. Opt. **3,** 133-142 (1994)

[46] D. Malacara, Z. Malacara, *Handbook of lens design,* Dekker, New-York, (1994).

[47] Y.Li, E. Wolf, *Focal shifts in diffracted converging spherical waves,* Opt. Commun. **39**, 211 (1981).

[48] Y. Li, H. Platzer, *An experimental investigation of diffraction patterns in low Fresnel-Number focusing systems,* Optica Acta **30**, 1621- (1983).

[49] W. Wang, A.T. Friberg, E. Wolf, *Structure of focused fields in systems with large Fresnel numbers,* J Opt. Soc. Am. A. **12**, 1947- (1995)

[50] Arnaud, J, *Representation of Gaussian beams by complex rays,* Applied Optics **24**, 538- (1985).

[51] Urs Vokinger, René Dändliker, Peter Blattner, Hans Peter Herzig, *Unconventional treatment of focal shift*, Opt. Commun. **157**, 218-224 (1998)

[52] J.W. Goodman, *Introduction to Fourier Optics*, 2nd edn., MacGraw-Hill, New York, Chap. 4, 63-69, (1968)

[53] B.E.A. Saleh, M.C. Teich, *Fundamentals of photonics*, Wiley (1991)

[54] N. Schröder. *Bauelemente der Optik.* Hanser Verlag (1992)

[55] F.M. Dickey, S.C. Hoswade, D.L. Shealy. *Laser Beam Shaping Applications.* Taylor & Francis, ISBN 0-8247-5941 (2000)

[56] C. Kopp, L. Ravel, P. Meyrueis *Efficient beamshaper homogenizer design combining diffractive optical elements microlens array and random phase plate.* J. Opt. A: Opt. **1**, 398-403 (1999)

[57] *Handbook of optical systems: Vol. 2. Physical Image Formation*, Edited by H. Gross, Wiley, Weinheim (2005)

[58] A. Buttner, U. D. Zeitner, *Wave optical analysis of light-emitting diode beam shaping using microlens arrays*, Opt. Eng. **41** (10), 2393-2401 (2002)

[59] L.Erdmann, M. Burkhardt, R.Brunner *Coherence management for microlens laser beam homogenizers.* Proc. SPIE Vol.4775 (2002)

[60] F. Wippermann, Uwe-D. Zeitner, P.Dannberg, A. Bräuer,S. Sinzinger, *Beam homogenizers based on chirped microlens array,* Opt. Express **15**, 6218-6231 (2007)

[61] K. Patorski, *The self-imaging phenomenon and its applications*, Progr. Opt. XXVII, 3108 (1989)

[62] B. Besold, N. Lindlein *Practical limitations of Talbot imaging with microlens arrays.* Pure Appl. Opt. **6**, 691-698 (1997)

[63] Sung-Il Chang and Jun-Bo Yoon, *Shape-controlled, high fill-factor microlens arrays fabricated by 3D diffuser lithography and plastic replication method*, Opt. Express **12**, 6366-6371 (2004)

[64] X. Dong, C. Du, S. Li, C. Wang, Y. Fu, *Control approach for form accuracy of microlenses with continuous relief*, Opt. Express **13**, 1353-1360 (2005)

[65] A. Schilling, R. Merz, CH. Ossmann, H.P. Herzig, *Surface profiles of reflow microlenses under the influence of surface tension and gravity*, Opt. Eng **39**, 2171-2176 (2000)

[66] D.J. Daly, M.C. Hutley, R.F. Stevens, *"Mach-Zehnder interferometer for measuring microlenses"*, Proc. SPIE Vol. 2340, 258-263 (1994)

[67] H.Sickinger, J. Schwinder, B. Manzke, *"Fiber based Mach-Zehnder interferometer for measuring wave aberrations of microlenses"*, Optik **110**, 239-243 (1999)

[68] S. Reichelt, H. Zappe, *"Combined Twyman-Green and Mach-Zender interferometer for microlens testing"*, Appl. Opt. **44**, 5786-5792 (2005)

[69] M. Born and E. Wolf, *Principles of optics*, 7th ed., Cambridge university press (1999)

[70] W. T. Welford, *Aberrations of optical systems*, Adam Hilger Ltd, Bristol and Boston (1986)